Intertidal sand boils within springs

By

Marianna Ramirez Lagunas

Thesis
Submitted to Flinders University
for the degree of

Master by Research
College of Science and Engineering
21 Feb 2024

Table Of Contents

Declaration

I certify that this thesis:

1. Does not incorporate without acknowledgment any material previously submitted for a degree or diploma in any university.

2. The research within will not be submitted for any other future degree or diploma without the permission of Flinders University.

3. To the best of my knowledge and belief, does not contain any material previously published or written by another person except where due reference is made in the text.

Marianna Ramirez Lagunas

Co-author statement

Chapter 3 of this thesis was written and submitted as a journal paper. I, **Marianna Ramirez-Lagunas** am the first author of the publication and was responsible for leading the project and designing the Conceptualization, Methodology, Formal analysis, Investigation, Data Curation, Writing - Original Draft, Visualization, and Project administration.

The co-authors of the publication contributed with the following:

Eddie Banks: Conceptualization, Supervision, Methodology, Review & Editing, Data collection

Ilka Wallis: Conceptualization, Review & Editing

Adrian Werner: Conceptualization, Supervision, Review & Editing

Margaret Shanafield: Conceptualization, Review & Editing, Data collection

Approximate contribution of each author to the publication (Chapter 3):

Ramirez-Lagunas: 80%, Banks: 5%, Werner: 5%, Wallis: 5%, Shanafield: 5%

Acknowledgments

“It is what it is, but it is at once too much and not enough”

-Anonymous

I would like to thank everyone that contributed to this project, especially my Flinders professors, Dr Banks, Dr Werner, Dr Wallis, Dr Shanafield and Dr Jazayeri, for their support and knowledge. Also, my thanks to the HDR team for assisting whenever I needed it.

During this project I lost the two pillars of my life, my mom Rebeca and my grandma Mamisa and I would like to thank them for all the love and support they always gave me. They were the most kind, supportive and amazing people I know. Wherever you are, I am sending all my love to you.

I am grateful for my friends, family and partner who have been with me along this ride and for all their support during some really painful times. My loving pets, Spike, Sansón and Ducky have really left a paw print in my heart and have helped me heal, thanks.

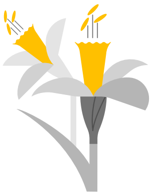

Publications

Ramirez-Lagunas, M., Banks, E.W., Werner, A.D., Wallis, I., Shanafield, M., 2022. Characterisation of intertidal springs in a faulted multi-aquifer setting. J. Hydrol. 128457. https://doi.org/10.1016/j.jhydrol.2022.128457

Appendix 1

Werner, A.D., Jazayeri, A., **Ramirez-Lagunas, M.**, 2020. Sediment mobilisation and release through groundwater discharge to the land surface: Review and theoretical development. Sci. Total Environ. 714, 136757. https://doi.org/10.1016/j.scitotenv.2020.136757

Appendix 2

Summary

This Master by Research thesis presents the results of a study aimed at characterising the hydrogeophysical properties and sediment characteristics of intertidal sand boils within springs at Sellicks Beach, South Australia. The study was conducted to describe the temporal and spatial variability of these sand boils and to gain a better understanding of their role in groundwater flow dynamics.

Chapter 1 introduces the physical processes of coastal groundwater discharge and focused on the characterisation of discrete discharge features that including springs and sand boils.

In Chapter 2, the study area at Sellicks Beach in the southwest of the Willunga Basin is described. This includes a detailed description of sediment transport at a micro-tidal environment with a dissipative beach profile and the impact of waves, tidal currents, and wind.

Chapter 3 details a hydrogeophysical characterisation of intertidal sand boils. The survey methods included thermal infrared imaging, electromagnetic geophysics, and environmental tracers (stable isotopes of water and salinity). The results showed that the sand boils exhibited significant spatial and temporal variability in their hydraulic conductivity and salinity. The thermal infrared imagery survey revealed that sand boils have higher temperatures than the surrounding areas, indicating greater water flow. The electromagnetic survey showed that the sand boils have lower bulk electrical conductivity, and defined the spatial extent of the boils within the intertidal zone. The water sampling showed differences in salinity and stable isotope composition between the sand boils and the surrounding area, indicating differences in water source and flow paths.

Chapter 4 focuses on the sediment characteristics of the sand boils and the surrounding area. The sediment analysis showed that the sand boils contain mainly pebble-sized grains, in contrast to the surrounding area where sediments range from fine to medium sands. This suggests that the sand boils are fed by a different source of sediment, possibly related to the geology of the area.

Overall, the study highlights the importance of intertidal sand boils as part of coastal groundwater discharge processes and the mechanisms that control their spatial extent and temporal dynamics. The results suggest that sand boils have higher hydraulic conductivity and are more permeable than the surrounding sediments, which may impact the distribution and quality of groundwater. The sediment analysis also suggests that the sand boils may have a distinct sediment source, which could be relevant to understanding the hydrogeological context of the area.

In conclusion, this thesis provides valuable insights into the hydrogeophysical and sediment characteristics of intertidal sand boils within beach springs. The findings have implications for understanding the dynamics of groundwater flow in the area, which may be relevant for water management and environmental planning. The study also highlights the importance of considering sediment characteristics in hydrogeological studies, as these can provide valuable information about groundwater flow pathways and sources.

Chapter 1

1.1 Introduction

Groundwater discharge in coastal environments occurs as diffuse seepage or as localised features described commonly as seeps, springs, sand boils and 'wonky holes' (Johannes, 1980; Stieglitz, 2005), and it is found to occur not only through the sea floor, but also within intertidal environments, and to tidal streams and rivers (Moore, 2010). Groundwater discharge through localised features, such as springs and sand boils can have important implications for coastal geomorphology, as it can contribute to the erosion or deposition of sediments in nearshore environments (FitzGerald, 1996; Taboroši et al., 2013)

Springs are discrete discharge features where groundwater flows upward through the subsurface and emerges at the surface (Wilson and Moore, 1998; Stevens and Meretsky, 2008). Springs can be perennial or ephemeral with varying discharge rates (Salama, 1996) and may occur due to abrupt changes in topographic slopes, geological structures and/or due to vertical/lateral changes in the subsurface materials (O'Driscoll et al., 2019). Coastal springs in the intertidal zone are often related to faults and fractures that provide preferential paths for groundwater flow. Along coastlines, faults and fractures are often exposed in the faces of cliffs and outcrops (Taboroši et al., 2013).

Currently, there is limited research on intertidal groundwater springs (Williams, 2016; O'Driscoll et al., 2019). Studies which have investigated coastal springs have focused on groundwater discharge quantification (Povinec et al., 2006; McCormack et al., 2014), whilst qualitative investigations (e.g., detailed coastal spring characterisation studies) are lacking (Stieglitz et al., 2005). Dale and Miller (2007) studied the fluctuations of temperature and salinity of intertidal spring discharge in Delaware, U.S.A. and found high seasonal variability in sediment temperature at the spring outlet. The authors concluded that thermal and salinity fluctuations must be considered when attempting to interpret biological productivity in groundwater springs.

1.2 Intertidal springs

The intertidal zone is part of the coastal environment, located between the low and high tide marks, where sediments are susceptible to transport due to wave action (Morales, 2022). Since groundwater is generally considered to be nutrient enriched compared to marine water (Cave and Henry, 2011), discharge to intertidal and marine environments should be considered for coastal water budget calculations, biological productivity assessments and coastal hydrological modelling. Groundwater springs are often important biodiversity hotspots (Eamus et al., 2006), with intertidal springs important features that allow vegetation, fauna, and microbial species to exist in a marine setting (Miller and Ullman, 2004). They also contribute to sediment transfer processes (Fanjul et al., 2008). In coastal areas where groundwater discharge occurs through springs, sand boils or other localised features, the resulting flow of water and sediment can create distinctive patterns and features on the seafloor. These features can play a role in shaping coastal morphology, influencing the formation of beaches, sandbars, and other nearshore landforms (Post et al., 2020).

Historically, intertidal springs have been an important source of drinking water for the local indigenous population around the world e.g., in North Queensland, Australia (Stieglitz, 2005), and provide water supply, for example, bathing and washing (Moosdorf and Oehler, 2017). Also, beach springs have been considered spiritually relevant for numerous indigenous communities (Taniguchi et al., 2019). Particularly, the Kaurna people in South Australia have recognised the springs at Sellicks Beach, South Australia, and other nearby beaches, as part of their traditional heritage. The Tjilbruke Dreaming history describes the creation of freshwater springs along the southern coastline of South Australia, where Tjilbruke the ancestor of the Kaurna people wept for his nephew. During their journey Tjilbruke's tears formed the freshwater springs along the coast (Malone, 2012).

1.3 Sand boils

Sand boils consist of conical sand vents that carry sediments and provide paths for groundwater movement to the surface (Kolb, 1975; Bonelli and Nicot, 2013; Werner et al., 2020).

Sand boil occurrence has been observed along the Mississippi River as early as 1941 (USACE, 1941) with subsequent studies focused on understanding and predicting sand boil formation (Kolb, 1975; Wolff 2002). For example, Glynn et al. (2012) applied a statistical model, geomorphology data and grain size analyses for predicting sand boil formation along the Middle Mississippi River Valley. Their methodology showed potential on predicting the locations of future sand boils. Recent field investigations of sand boils along the Mississippi River by Robbins et al., (2019) aimed to study the vertical hydraulic gradient in sand boils by comparing theoretical values of vertical hydraulic gradients to their measurements and results. Their results correlate to the findings of Guhman and Pederson (1992), indicating that the sediments present at the surface of the sand boil are finer compared to the sediments present towards the bottom of the conduit. They concluded that the head loss in a sand boil is a function of grain, conduit diameter and flow rate.

In the Netherlands, sand boils have been identified in deep polders (De Louw et al., 2010). Particularly, De Louw et al. (2010) studied the sand boils located in the Noordplas Polder. The authors identified 54 sand boils, mainly occurring at the edges of the Noordplas Polder, in ditches or ditch banks. Water fluxes and chloride concentrations were investigated, and it could be shown that the sand boils contribute the largest water fluxes and highest chloride concentrations to the polder compared to diffuse seepage to the surface. Continued efforts by De Louw et al. (2013) identified natural saltwater upconing due to the groundwater discharge of the sand boils within the polder. Field measurements and 3D numerical simulations indicated that water contributions from the boils comprises a mixture of groundwater with a wide range of salinity and derived from varying depths.

Sellicks Beach, located in South Australia, has been identified as an area where sand boils have been observed within the intertidal zone (Ramirez-Lagunas, 2020). Sand boils were visible during low tide periods but were observed to be completely submerged by seawater during high tide. Based on salinity investigations, the water discharged from the sand boils is believed to be a result of mixing between groundwater and seawater. Furthermore, observations made by Ramirez-Lagunas et al. (2020) have demonstrated that the water discharged from the sand boils also led to the release of sediments onto the surface. This phenomenon is believed to have implications for sediment transport processes in the beach environment and may be of significance for local ecosystem dynamics. The observed release of sediment into the water may also have implications for water quality in coastal environments. These observations highlight the importance for continued research into the occurrence of beach sand boils and their potential impact on coastal environments.

The study of beach sediments is an important factor as it provides an insight into the physical, chemical, and biological processes that shape and form coastlines. Particularly, grain size distribution analyses can provide information regarding the source and transport of the sediments (Folk and Ward, 1957). Historically, sediment investigations in coastal areas have focused their efforts on the impact of hydraulic forces like wave and wind action on the sediment characteristics (e.g., size, degree of sorting, permeability) (Inman, 1949; Folk, 1962; Klein et al., 2005; Nugroho and Putra, 2018). However, to the author's knowledge, no research has been conducted to investigate the influence of sand boils on the sediment characteristics in beach environments.

1.4 Aims and objectives

The objective of this Master by Research thesis was to analyse the intertidal springs discharge from a coastal multi-aquifer system in Sellicks Beach, South Australia. Following the introduction (Chapter 1), Chapter 2 consists of a description of the area of study detailing the climate, sediment transport, geology, and hydrogeology of the area. In Chapter 3, a methodology was designed to investigate the spatial distribution, extent, temporal variations, origins, and patterns of groundwater-seawater mixing processes within these springs. The methodology consisted of applying near-surface electromagnetic (EM) geophysical techniques, stable isotopes (^{2}H and ^{18}O), water levels, electrical conductivity (EC), pH, and thermal infrared (TIR) imagery. In Chapter 4 the sediment characteristics of sand boils were investigated in detail on the basis of the sand boils within springs in Sellicks Beach, South Australia. The distribution patterns of sediment grain sizes and spatial variability within the intertidal zone and within the sand boils were analysed. Measurements were also taken to determine sand boil dimensions, sand layer thickness, porosity, permeability, hydraulic conductivity, and water discharge, with the objective of better understanding the impact of sand boils on an intertidal environment.

This research project presents the first documented effort (to the authors' knowledge) to comprehensively analyse the sediment characteristics of intertidal sand boils in addition to hydrogeophysical measurements and water sampling, thus expanding the existing knowledge on intertidal hydrological processes.

Chapter 2

2.1 Area of study

The study site is located at Sellicks Beach, in the southwest of the Willunga Basin, approximately 46 km south of Adelaide, South Australia (Figure 2.1). At this location, there are intertidal springs that appear as groupings of sand boils at various locations above the low-tide mark.

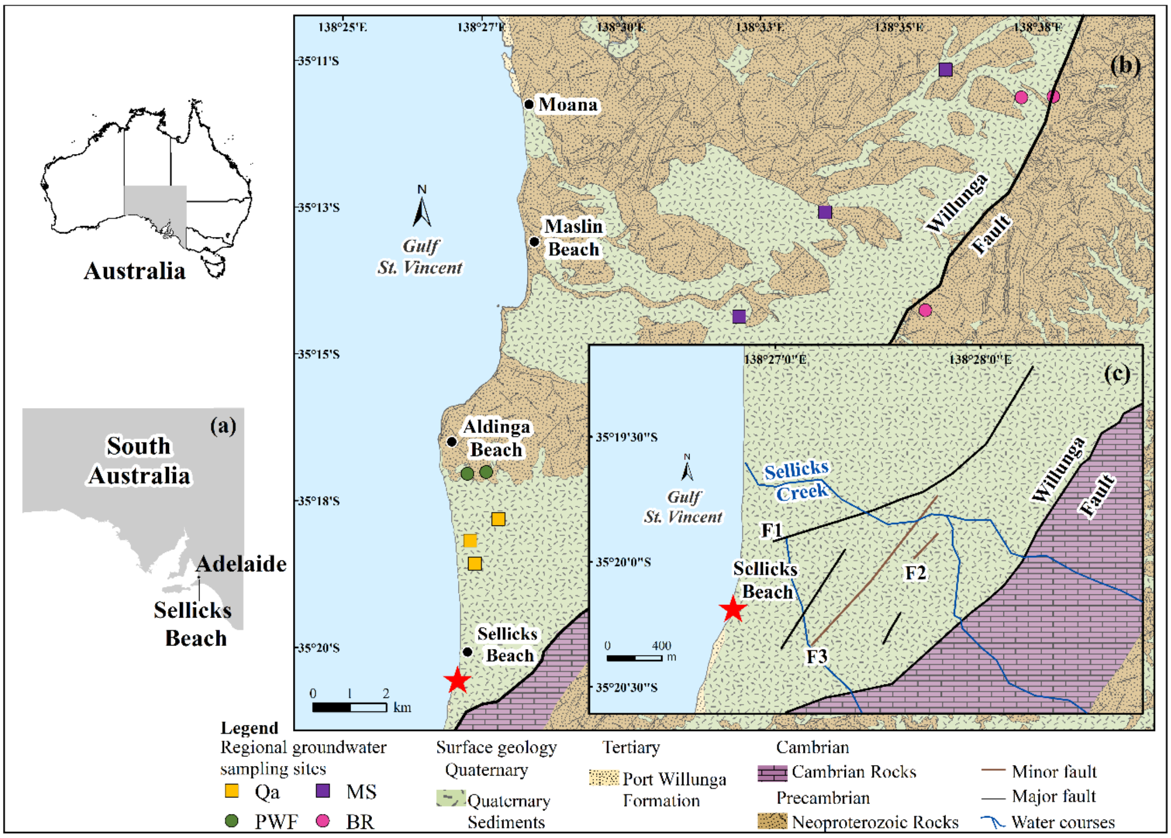

Figure 2.1 Locality map of Sellicks Beach and the surrounding area: (a) Location of Sellicks Beach within South Australia, (b) Map of the southern Willunga Basin, showing surface geology, the Willunga Fault and regional groundwater sampling points (see Table 1) in the Quaternary (Qa), Port

Willunga Formation (PWF), Maslin Sands (MS) and basement rocks (BR) aquifers, and (c) inset map, showing local water courses, and major and minor faults near the study site.

2.2 Climate

The Mediterranean climate of the study area comprises hot, dry summers and cold, wet winters, with mean annual rainfall of approximately 442 mm/yr (Noarlunga, Bureau of Meteorology station: 023885; Bureau of Meteorology, 2020). Measurements of sand boils at Sellicks Beach were undertaken during May 2017 (early winter), November 2019 (late spring) and September 2020 (early spring). The average minimum and maximum air temperatures recorded at the Bureau of Meteorology station 023885 were (respectively) 13.2°C and 22.0°C in 2017, 12.9°C and 22.3°C in 2019, and 12.3°C and 21.2°C in 2020. In May 2017, the average maximum and minimum daily temperatures were 17.3°C and 11.1°C, respectively. In November 2019, maximum and minimum temperatures were 22.7°C and 12.4°C, respectively, on average. Whereas in September 2020, the average maximum and minimum daily temperatures were 13.0°C and 8.6°C, respectively (Bureau of Meteorology, 2020).

2.3 Sediment transport

Sediment movement along the coast is influenced by various processes, with three major factors being particularly significant. These comprise waves, tidal currents, and onshore winds (Short, 2010). Waves have a significant impact on sediment transport, as they can cause erosion and deposition along the coastline. Transport is influenced by the size and energy of the waves, as well as the slope and composition of the seafloor (Greenwood, 1978). Tidal currents are another important factor that affect sediment transport around the coast. Tides can cause significant changes in sea level, resulting in the movement of water and sediments in and out of the nearshore zone (Dalrymple and Choi, 1978). The velocity of onshore wind currents can significantly affect sediment transport, especially in areas with exposed beaches. Rotnicka (2011) demonstrated that the rate of sediment transport due to wind is directly proportional to the velocity of the wind.

Along the Adelaide coastline, the tidal range fluctuates from around 2.4 m during spring tides to nearly 0 m during neap tides. Despite this, the sea level can also be significantly influenced by the effects of winds and atmospheric pressure gradients. Tidal currents in the waters along the Adelaide coastline generally flow parallel to the shore in a north-south direction, with velocities that can reach up to 0.2 to 0.3 m/s. The dominant prevailing winds in the southwest direction generate a wind-set current towards the north at a velocity of around 0.15 m/s for a wind speed of 25 knots. When this wind-set current combines with the northerly tidal current, it can cause a net northerly movement of sediment suspended by waves from the seabed. Nevertheless, compared to waves, tidal and wind-generated currents play a lesser role in transporting sand in the nearshore zone (Department for Environment and Heritage, 2005).

At Sellicks Beach, the environment is mostly microtidal (~2 m tidal range), where the moderate wave energy varies seasonally, with lower wave energy in summer and moderate wave energy in winter (Cann et al., 2014). This fluctuation in wave energy can cause seasonal changes in sediment transport and beach morphology. Sellicks Beach is a dissipative beach and presents a low-sloping profile, where its morphology dissipates wave energy. The beach slope in the study site is 1.72° (tanβ=0.03). Dissipative beaches are characterised by wide, flat surf zones, low gradient beach slopes (tanβ=0.01-0.03) with abundant fine sediments (Komar, 1998; Sherman, 2019). Waves in dissipative beaches maintain a consistent height or undergo a gradual decrease in height as they approach the shore before breaking, as described by Wright et al. (1979).

In the area of study, dynamic processes (e.g., wind-driven waves) can present seasonal variations, but the dominant southerly winds are the main controlling factor for the net northward transport of sand along the coastline of the Adelaide Metropolitan area. The medium energy waves approach the shore at an oblique angle, leading to the occurrence of littoral transport, which can be described as the movement of sediments in the nearshore by waves and currents. As the waves hit the beach obliquely, their energy causes the sediment to move along the beach, resulting in the net northward drift of beach sediments on the coastline (ACWS, 2006).

Sand sediments found on the beaches of the Adelaide Metropolitan area comprise mainly of quartz grains with varying amounts of shelly fragments depending on the location. These differences in grain size and composition are a result of natural sorting (Department for Environment and Heritage, 2005). Despite the continuous impact of wave energy, the grains do not tend to reduce in size due to their smooth surface, which makes them less likely to break during collision with other grains (Coastal Management Branch, 1984).

2.4 Geology

At Sellicks Beach, the Port Willunga Formation (PWF) outcrops as low coastal cliffs (Figure 2.2), which have experienced significant erosion, deep gullying, and rotational slumping, creating a series of alluvial fan sediments and platforms (Bourman et al., 2016). May and Bourman (1984), identified in the southern area of the beach, an extensive platform of the PWF that outcrops within the intertidal zone, and that contributes to concentrated marine erosion of the cliffs.

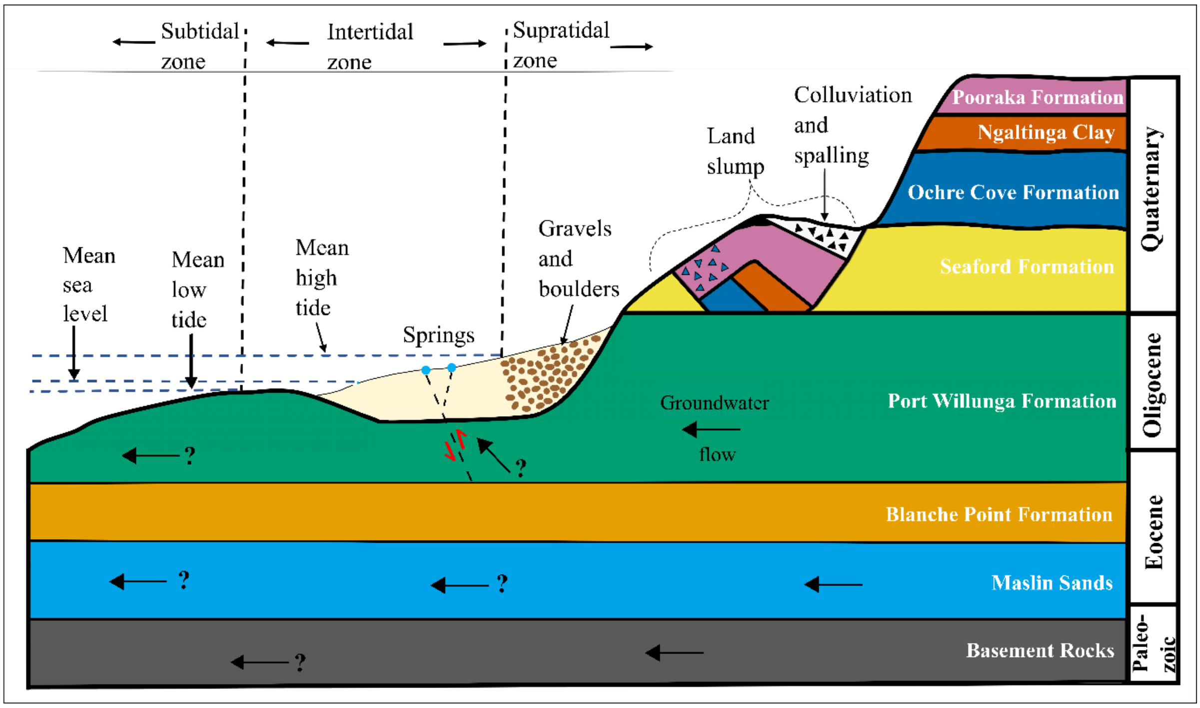

Figure 2.2. Conceptual model of the intertidal zone, and the location of the springs at Sellicks Beach. The following geological formations are represented in the idealised cross-section: Quaternary (sands and interbedded clays), Port Willunga Formation (sands and limestone), Maslin Sands (sands and clays) and basement rocks (slate, quartzite, and shale). Modified geological cross section from Cann et al. (2014). Not to scale.

Sediments at the beach consist of sand and gravels, with seasonal variations in sediment transport leading to geomorphic changes in the beach profile and sediment distribution. For example, Cann et al. (2014) observed that in summer, the volume of sand is greater compared to winter, when higher wave energy exposes the PWF platform, leaving gravels and sand visible only in narrow areas along the beach at low tide. They also established that the cobble-size gravels (located above the high tide mark) originate from the Neoproterozoic and Cambrian rocks outcropping nearby and are transported to the beach by coastal erosion as well as being impacted by northward longshore transport. The Quaternary alluvial fan sediments consist of poorly consolidated sands exposed in the cliffs and transported to the near-shore by marine erosion (e.g. wave action) and heavy rainfall events (May and Bourman, 1984; Cann et al., 2014).

2.5 Structural geology

In the Willunga Basin, neotectonism has highly influenced the geology of the coastline (Preiss, 2019), where active normal, reverse, and oblique faulting has been documented (Jayawardena, 2013; Preiss, 2019). The Willunga Fault (Figure 2.1) is an NE-SW oriented active reverse fault, (Tokarev, 2005; Lubiniecki et al., 2019). The stratigraphy at Sellicks Beach is complex (Figure 2.2), where tectonic activity and marine erosion have created a large rotational land slump and unstable cliffs, due in part to its proximity to the Willunga Fault and the occurrence of numerous smaller faults in the area (May and Bourman, 1984). For example, geophysical investigations by Reed (1982) were able to identify an extensive fault zone north of the main Willunga Fault, located at the top of the PWF cliffs approximately 200 m from the study site, and possibly extending further to the west. The fault zone consists of a major fault (F1) and two minor faults (F2 and F3; Figure 2.1). Additionally, Lubiniecki et al. (2019) identified small faults (‘deformation bands’; Aydin, 1978) with displacements of a few millimetres in the PWF cliff faces, approximately 60 m from the study site.

2.6 *Hydrogeology*

Martin (1988) defined the Willunga Basin as a complex multi-aquifer system, where regional groundwater flows from the northeast of the basin towards the coast. The basin comprises four main hydrogeological units, Quaternary (Qa), PWF, Maslin Sands (MS) and fractured basement rocks (BR) (Figure 2.2). The Quaternary aquifer is mainly unconfined and considered as low yielding aquifer. The main sources of groundwater within the basin are the Maslin Sand and the PWF aquifers (Knowles, 2007). Rainfall and streambed infiltration recharge the Qa, PWF and MS aquifers, while lateral inflows to lower units from the Precambrian/Cambrian basement rocks aquifer also occur at the boundary of the basin (Adelaide and Mount Lofty Ranges NRM Board, 2007; Shanafield et al., 2020).

Groundwater discharge from the Willunga Basin’s aquifers to the sea has been described in previous studies (Martin, 1998; Lamontagne et al., 2008; Short et al. 2014; Post et al. 2018). The limited groundwater monitoring along the Willunga Basin coastline makes it challenging to estimate groundwater discharge to the sea (Lamontagne et al., 2008). Nevertheless, Lamontagne et al. (2008) used a flow net methodology to calculate discharge rates of 670 ML/yr from the PWF and 120 ML/yr from the MS aquifers. Short et al. (2014) obtained EC and ^{222}Rn measurements of the intertidal zone and within beach sediments from part of the Willunga Basin coastline and identified groundwater discharge to the sea to be spatially intermittent. Therefore, Lamontagne et al.'s (2008) assumption that groundwater discharge occurs along the entire coastline likely overestimated discharge rates to the ocean.

The sedimentary aquifers within the Willunga Basin provide fresh groundwater for the irrigation of vineyards and other agricultural crops (e.g., barley, wheat, almonds, and olives) (Harrington and Cook, 2012; Bardsley et al., 2017). The Willunga Basin is comprised of fluvial Quaternary sediments, overlying mid- to late-Tertiary marine fossiliferous strata (Port Willunga Formation, Blanche Point Formation, Maslin Sands Formation), which are underlain by Precambrian/Cambrian basement rocks (Fairburn, 1998). The wedge-shaped basin, bounded to the east and south by the Willunga Fault, is part of the much larger St Vincent Basin, which formed during the continental separation of Australia and Antarctica ~43 million years ago (Dyson, 1998; Martin, 1998). According to monitoring wells located in the southwest of the Willunga Basin (~6 km northeast of the study site), groundwater levels in the Port Willunga Formation aquifer from the last 10 years have been largely stable, with maximum fluctuations of ~1 m. Groundwater levels within the Maslin Sands and basement rock aquifers have also remained fairly stable (maximum fluctuations of ~0.5 m) (DEW, 2021).

Chapter 3

Characterisation of intertidal springs in a faulted multi-aquifer setting.

Abstract

In intertidal zones, groundwater is often present as seepage that provides freshwater and nutrients to marine ecosystems. Point discharge or springs in intertidal zones have been observed in many locations, often in the form of sand boils. The spatial extent, temporal variability and source of intertidal springs are rarely documented and typically, not well understood. This study examined four intertidal groundwater springs at Sellicks Beach, South Australia, during May 2017, November 2019 and September 2020 using a combination of hydrogeophysical methods. A thermal infrared survey undertaken in 2017 showed springs as groupings of closely spaced sand boils that were warmer (15°C) than the surrounding saturated beach sediments (7°C). The four springs ranged in diameter from 0.20 to 0.45 m. Electromagnetic geophysical surveys identified a resistive anomaly (3.5 to 5.0 ohm.m), assumed to represent freshwater upwelling at the location of a spring, that extended 10 m horizontally and at least 6.7 m vertically. The average electrical conductivity of water discharging from the springs was 18.4 mS/cm, while seawater was 54.8 mS/cm. $\delta^{18}O$ and $\delta^{2}H$ data from the springs showed a variation between winter and spring, likely caused by variations in mixing ratios between seawater and groundwater. The springs are proximal to major regional fault systems that likely create preferential flow paths that control spring location and flow rates. The observations of

spring characteristics highlight the critical role of seawater-groundwater mixing ratios, preferential flow paths and tidal variations in creating temporal variability in spring discharge and salinity.

3.1 Introduction

The intertidal zone is a vital link between terrestrial and marine environments (Benkendorff, 2008) that is influenced by sea-level fluctuations, groundwater discharge, meteorological forces and sediment transport (Smith, 1986). Intertidal discharge of groundwater is an important phenomenon that shapes ecological and sedimentological processes within intertidal zones and the near-shore environment (Miller and Ullman, 2004; McAllister et al., 2015). For example, groundwater is generally nutrient enriched compared to seawater, and in many places, groundwater discharge provides the primary source (e.g., rather than surface water discharge) of nutrients (Charette et al., 2001; Lee et al., 2009; Cave and Henry, 2011; Liu et al., 2018), and trace elements (Charette and Sholkovitz, 2006; Beck et al., 2007; Rodellas et al., 2014) to marine water bodies. Furthermore, groundwater discharge is known to modify the geomorphology of beaches, whereby high rates of groundwater discharge tend to destabilise intertidal sediments (Bokuniewicz et al., 2008; Post et al., 2020).

The composition of groundwater discharge within intertidal zones is typically a combination of recycled seawater that entered the subsurface during high tide, and (usually) fresher groundwater resulting from net recharge to aquifers in inland regions (Moore, 1999; Li and Barry, 2000; Robinson et al., 2007; Xin et al., 2010). The main processes that control groundwater discharge within intertidal zones include: the subsurface hydraulic properties, the regional aquifer hydraulic gradient, water density variations between the discharging groundwater and seawater, and ocean tides and waves (Taniguchi et al., 2002; Burnett et al., 2003). While intertidal groundwater discharge in the form of diffuse seepage is widespread, under certain circumstances, localised discrete-discharge features may appear (Dale and Miller, 2007; Röper et al., 2014). The former leads to often extensive seepage faces, whereby saturated surface conditions are maintained over large areas, allowing benthic aquatic organisms to survive within intertidal zones during low tides (Waska and Kim, 2011). The latter has been previously described as seeps, springs, boils, and sand boils (Johannes, 1980; Stieglitz, 2005; De Louw et al., 2010; Moore, 2010).

Intertidal discharge to the ground surface can occur from faults and fractures that provide preferential paths for groundwater flow (Taboroši et al., 2013). An example of fracture-controlled point discharge was analysed by El Hage et al. (2020), who used thermal satellite images from the Lebanese coastal region to study groundwater seeps. They identified point discharge zones, and mapped faults and fractures to assess the possibility of using fracture-controlled groundwater discharge as an alternative source of freshwater. Groundwater discharge through discrete flow features may lead to the ejection of sand from the subsurface (e.g., de Louw et al., 2010; Werner et al., 2020). De Louw et al. (2010) described groundwater vents through which sediment is brought to the surface by the action of groundwater discharge as sand boils. In the sand boils that they studied, the vents arose from heave and fracturing of peat layers within Dutch polders. Werner et al. (2020) distinguished sand boils from boiling sand, whereby the latter was used when the sediment surface appears as a boiling fluid of more distributed sediment movement than the isolated vents of sand boils.

A number of techniques have been applied previously to characterise point discharge features. The most common of these methods are based on temperature and salinity variations (Taniguchi et al., 2019). For example, thermal infrared (TIR) imaging has been used to map diffuse seepage and point discharge in coastal environments, where there is a thermal contrast between groundwater and seawater (e.g., Danielescu et al., 2019). Mulligan and Charette (2006) and Duarte et al. (2006) used airborne TIR images to delineate the spatial variability of diffuse discharge in Waquoit Bay (Massachusetts) and western Hawai'i, respectively. Röper et al. (2014) used ground-based handheld TIR imagery to detect and map the horizontal extent of intertidal springs in north-western Germany.

Geochemical tracers are widely used techniques in groundwater discharge studies that provide information on the origin, composition and age of groundwater (Aggarwal et al., 2009). The radioactive isotope radon is frequently used in submarine groundwater discharge (SGD) investigations (Cable et al., 1996; Burnett et al., 2006; Povinec et al., 2012), as it is often several orders of magnitude more concentrated in groundwater than in surface waters (Burnett and Dulaiova, 2006; Tait et al., 2013). Short et al. (2014) used radon measurements of the surf zone and porewater from beach sediments to characterise potential SGD along the coastline of the Willunga Basin in South Australia (from Moana Beach to Sellicks Beach). Their results indicated potential groundwater discharge zones along the coastline. The stable isotopes of water, ^{2}H and ^{18}O have also been used to characterise groundwater and seawater mixing (Terwey, 1984). For example, Povinec et al. (2006) used $\delta^{2}H$ and $\delta^{18}O$ data to investigate the mixing between groundwater from springs and seawater along the coast of Sicily. Their results showed that the spring water composition consisted of up to 50% continental groundwater.

In coastal areas, electromagnetic (EM) geophysical methods have been applied to study the groundwater salinity variability within subsurface sediments (Yechieli et al., 2001; Schneider and Kruse, 2003; Levi et al., 2008). For example, Paepen et al. (2020) conducted EM surveys to map groundwater discharge along the coast of Belgium. Their results identified a large zone (>100 m) of low bulk conductivity (3.5 to 6.5 mS/cm), associated with diffuse groundwater discharge, and concluded that EM techniques provide valuable information for intertidal groundwater discharge investigations.

Each of the techniques described above (hydrochemical and environmental tracers, temperature-based methods, EM geophysical methods) offer useful insights into subsurface processes within intertidal zones. However, these methods are more usually adapted in combination (rather than in isolation) due to limitations in their spatial and temporal resolution and in the information content of each (e.g., Stieglitz, 2005; Swarzenski and Izbicki, 2009). This way, valuable information of point discharge features can be obtained to determine their spatial extent, geometry, water quality and mixing patterns within dynamic intertidal zones.

The aim of this study was to characterise intertidal springs discharging from a structurally complex coastal multi-aquifer system, located in Sellicks Beach, South Australia. Figure 3.1 shows an example of the springs targeted in this research. The methodology applied in this investigation aimed to evaluate their spatial distribution, extent, temporal variability, origins, and groundwater-seawater mixing patterns. A combination of near-surface EM geophysical techniques, stable isotopes (^{2}H and ^{18}O), water levels, electrical conductivity (EC), pH and TIR imagery was applied. This research describes the first published attempt (to the authors' knowledge) to obtain detailed measurements and sampling of intertidal sand boils, thereby adding to the existing knowledge base of intertidal hydrological processes.

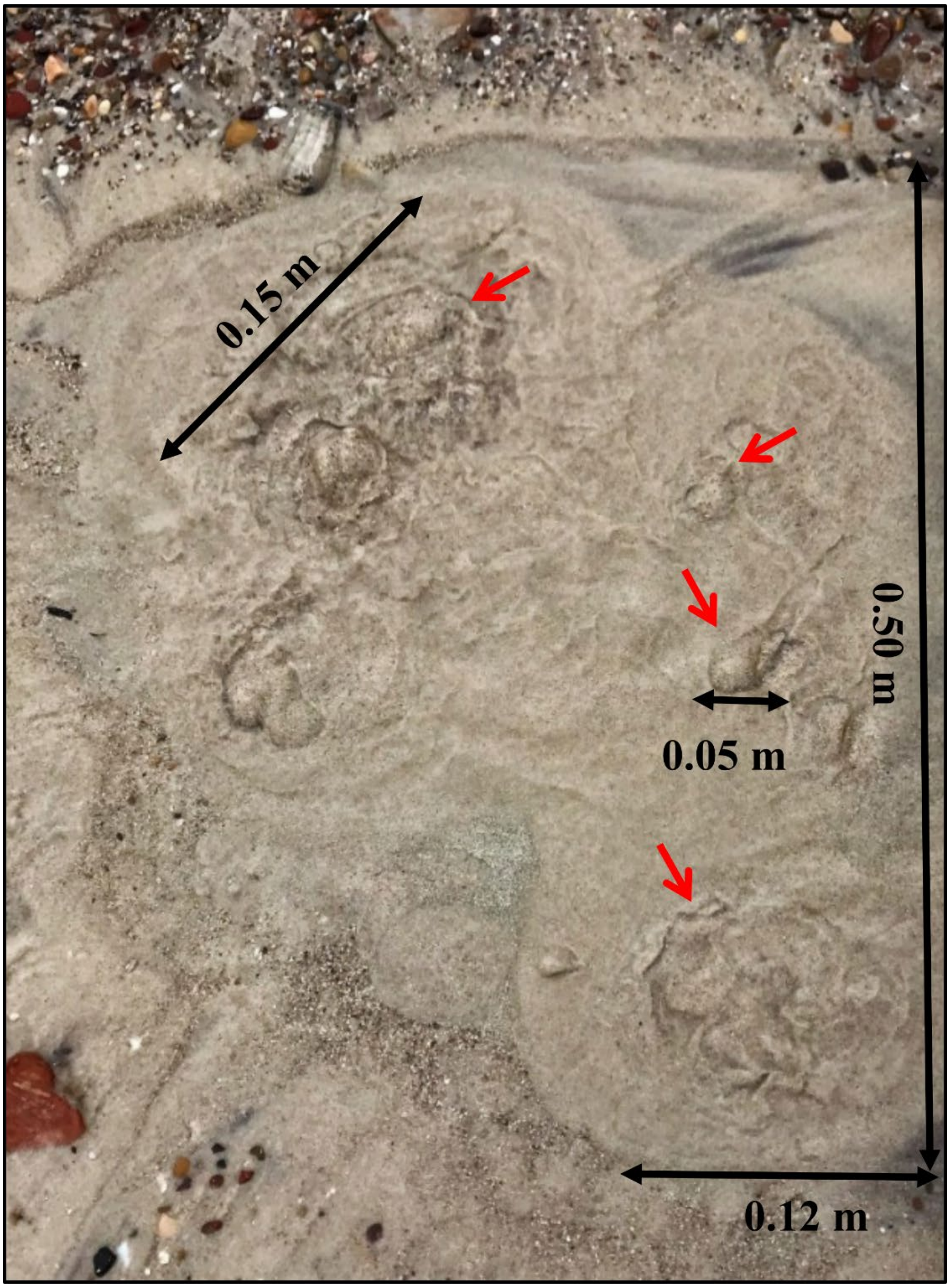

Figure 3.1. Photo showing an example of an intertidal spring (Spring F; location shown in Figure 3.2) at Sellicks Beach, South Australia. Image shows sand boils with diameters ranging from 0.05 to 0.15 m.

3.2 Methods

Field investigations were designed to explore the characteristics of intertidal springs and were conducted at the southern end of the Sellicks Beach coastline (Figure 2.1). At this location, intertidal springs occur as groupings of closely spaced sand boils (e.g., Figure 3.1). Field investigations were undertaken between 23 to 26 May 2017, 14 November 2019 and 17 to 18 September 2020. In the 2017 field campaign, Spring D was visible during daytime, and Springs A, B and C were visible to the naked eye only at night. We speculate that changes in the beach profile (e.g., sand thickness) and tidal fluctuations may explain why Springs A, B and C were only observed at night and not during daylight hours. Average daytime low tide was 0.73 m, while average night-time low tide was 0.45 m (Bureau of Meteorology, 2017). Further observations are required to improve the current understanding of spring temporal variability at the field site. Springs E and F were visible in the daytime and only during the 2019 field campaign. During the 2020 field campaign, Spring G was visible in the daytime (Figure 3.2). Additional intertidal observations from the 2020 campaign included the measurement of the thickness of the sand overlying the PWF. This involved the use of a solid metal stake to determine the depth of refusal to the more competent PWF formation.

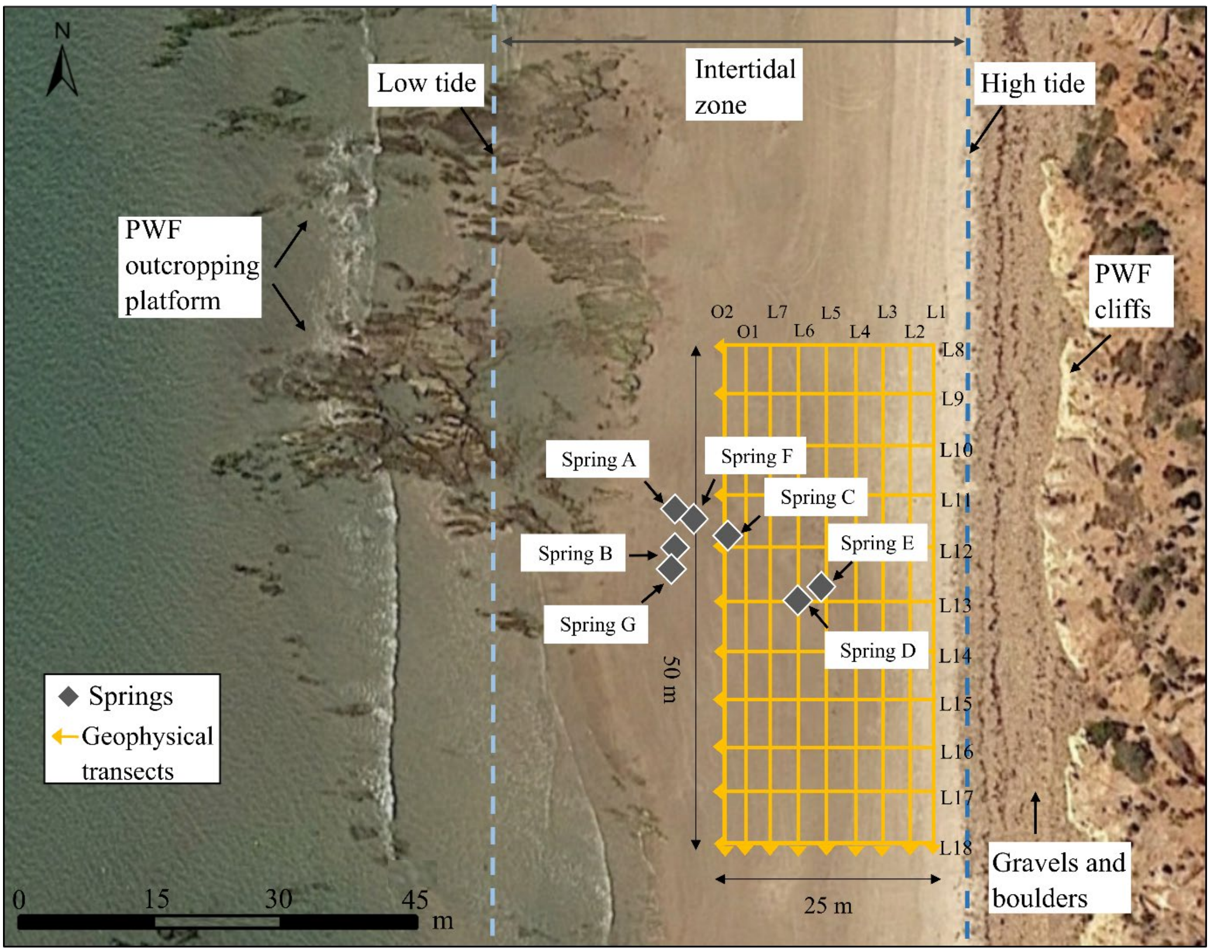

Figure 3.2. Location of the intertidal springs at the study site in Sellicks Beach. Survey transect lines from the EM geophysical survey are also shown and the dashed lines represent average low and high tide levels (Bureau of Meteorology, 2020) at Sellicks Beach.

EM geophysical measurements of the subsurface were collected at low tide over the study site using a CMD-Explorer instrument (www.gfinstruments.cz), with apparent conductivity (mS/m) measurements recorded every 1 sec along a survey grid and locations determined using a Real Time Kinematic (RTK) positioning instrument (www.trimble.com). The CMD-Explorer is a ground-based, multi-depth EM instrument that measures both in-phase and out-of-phase data at set time intervals.

The instrument has an operating frequency of 10 kHz and has three receiver coils, with 1.48, 2.82 and 4.49 m intercoil spacings. These three transmitter-receiver coil separation spacings and frequency output provide an effective depth of investigation of 2.2, 4.2 and 6.7 m (horizontal coplanar configuration, high-depth mode). The out-of-phase data that the instrument records are converted to apparent conductivity, using a low induction number approximation (McNeill, 1980). Data inversion was conducted using the Aarhus Workbench software package (www.aarhusgeosoftware.dk). The inversion routine uses the AahusInv code (Auken et al., 2015), previously used for ground-based EM data (Christiansen et al., 2016). Inverted data in the results section is presented as resistivity (ohm.m; equivalent to 1/apparent conductivity (S/m)). The EM survey comprised a survey grid of 20 transects, which included 9 north-south transects lines of 50 m length, and 11 east-west transects lines of 25 m (Figure 3.2). The inverted data were collated, and nearest neighbour interpolation was used to create resistivity layers of the study site with the software package Surfer 11 (www.goldensoftware.com).

During the May 2017 field campaign, a TIR mapping survey was used to evaluate the spatial distribution of the groundwater discharge from the springs within the intertidal zone. The survey was conducted using a handheld FLIR E5-XT thermal camera with a measurement range of –20 to 400°C and measurement accuracy of ±2°C. The TIR mapping was conducted at low tide when the springs were exposed and at night to avoid solar interference on the thermal signature of the springs.

The 2017 field campaign involved sampling seawater and Spring D for salinity (EC), temperature, pH and the stable isotopes of water. EM geophysical surveys, TIR mapping of the study site and water level time series measurements from a shallow piezometer installed in Spring D was also undertaken.

During the 2019 field campaign, only salinity, temperature, pH and the stable isotopes of water were sampled in Spring E and F. The 2020 field campaign involved seawater and Spring G sampling for salinity, temperature, pH, the stable isotopes of water and sand thickness measurements.

Water samples were collected from Springs D, E, F, G and the sea using a hand pump connected to a 1-m length of flexible hosing. EC, pH and temperature were measured in the field using a handheld YSI® multi-parameter probe. Spring and seawater samples were obtained approximately every 12 hours for 3 days during the 2017 field campaign. In the 2019 campaign three spring and seawater samples were obtained (at 30 minutes intervals) during low tide. Spring and seawater samples were obtained approximately every 15 minutes for 2 days at low tide, during the 2020 field campaign. Samples were filtered (0.45 μm) and collected in 2-mL glass vials to analyse the stable isotopes of hydrogen (^{2}H) and oxygen (^{18}O), using a Picarro L2130-*i* Isotope δ^{18}O/δ^2H Ultra High Precision Isotopic Water Analyser (Picarro, 2020). Results are reported against the Vienna Standard Mean Ocean Water (VSMOW) in per mil (‰), using delta (δ) notation.

A shallow polyvinyl chloride (PVC) piezometer was installed in Spring D (see Figure 4) to a depth of 0.76 m and protruded to a height of 0.5 m above ground. The piezometer had a 0.1 m long slotted screen and was equipped with an In-Situ Aqua TROLL 200® datalogger to record temperature, pressure, and EC at 1-minute intervals from 23-26 May 2017. Due to the location of the spring in the intertidal zone, seawater entered the piezometer during high-tide periods. Another In-Situ Aqua TROLL 200® datalogger was deployed offshore of the study site to measure the tidal fluctuations during the 2017 field campaign.

3.3 Results

3.3.1 Spring observations

The physical location and size of the springs within the intertidal zone of Sellicks Beach changed between the three field campaigns. In May 2017 (Southern Hemisphere winter), four springs (Springs A, B, C and D) were identified, while in November 2019 (Southern Hemisphere late spring) only two springs were identified (Springs E and F) and September 2020 (Southern Hemisphere early spring), only Spring G was observed. The diameter of the sand boils within the springs also showed distinct differences between field campaigns. For example, the sand boil within Spring F (November 2019, Figure 3.1) had an average diameter of 0.1 m, while the sand boils from the observed springs identified in the 2017 and 2020 campaigns were considerably smaller, with an average diameter of 0.01 m. The thickness of the sand layer measured in the 2020 campaign varied from 0.82 m to 0.38 m (east-west), decreasing towards the sea and from 0.45 m to 0.64 m (north-south). Particularly, the sand thickness at the location of Springs A, B, C, D, E and F was 0.43 m, 0.41 m, 0.54 m, 0.70 m, 0.69 m and 0.45 m, respectively.

3.3.2 EM geophysical survey

The data from the EM geophysical survey showed the spatial variability in the resistivity of the subsurface around Spring D to a depth of 6.7 m based on the transmitter and receiver separations of the CMD instrument (Figure 3.3). The 2.2 m depth slice of the inverted resistivity data, shows a central, more resistive anomaly (10 x 12 m) of about 5 ohm.m (compared to the surrounding material), located directly beneath the visible surface expression of Spring D. This central anomaly represents spring discharge of groundwater from the saturated sand and sediments of the underlying PWF. The eastern boundary up against the base of the PWF cliffs has resistivity values of ~2.0 ohm.m and is influenced by an increase in thickness of unsaturated beach sediments, including the existence of gravels and boulders. To the north and south (along the beach) of the central anomaly there are resistivity values of <1.5 ohm.m, associated with seawater saturated sand and PWF sediments. The depth slice at 4.2 m depth shows a similar spatial distribution of resistivity values as the shallow layer at 2.2 m depth. Meanwhile, the depth slice at 6.7 m depth shows that the size of the resistivity anomaly is influenced by Spring D and increased by 5 m along the length of the western boundary (seawards).

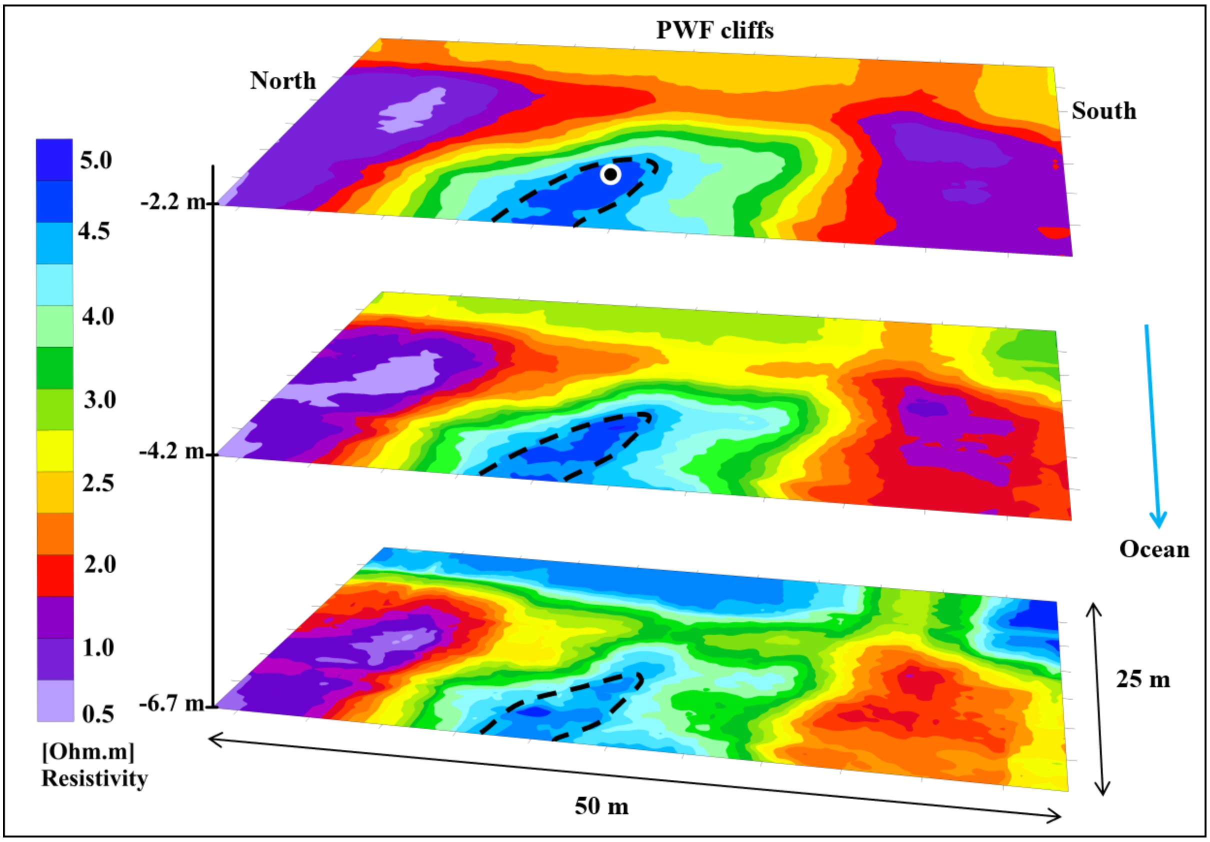

Figure 3.3. Multi-depth resistivity model of inverted EM data collected across the 20 transect lines (survey grid 50 m x 25 m) at the study site. A more resistive zone is present at the location of Spring D (black circle) and increases in size towards the seaside of the model domain. The dashed line represents the central, resistive anomaly created by groundwater discharge from Spring D (5.0 ohm.m).

Transect line L6 parallel to the coastline shows that the resistive anomaly (5 ohm.m) located below the surface expression of Spring D is present across the vertical extent of the depth profile (Figure 3.4). Low resistivity (<1.5 ohm.m) zones in the north and south of the profile, associated to the seawater saturated sand and PWF sediments, extend from the surface to 3 m below the ground. In particular, a low resistivity feature (~1.0 ohm.m) is present across the profile (north-south) at 0.5 m below the ground level and correlates with the average sand thickness measured in the area.

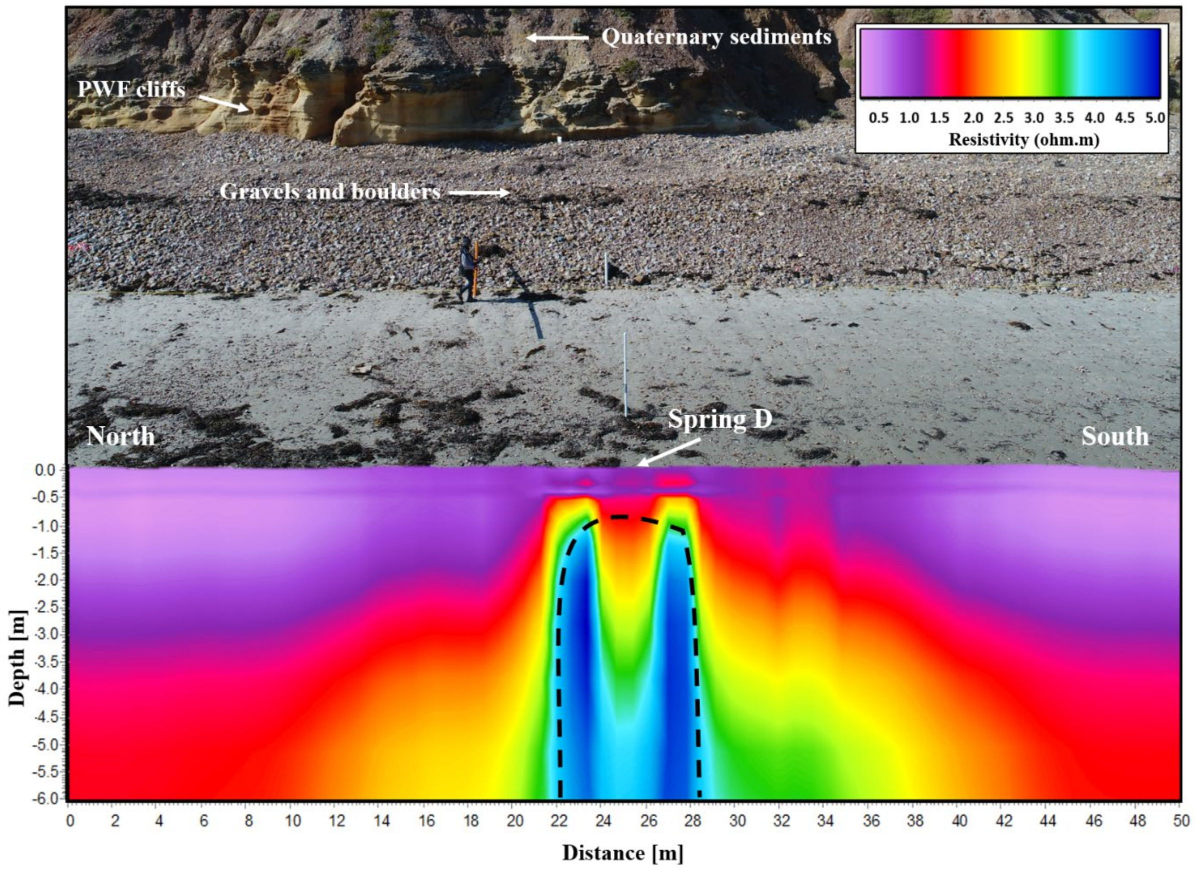

Figure 3.4. North-south EM transect line (L6) depth profile overlaid on aerial imagery. The dashed line represents the resistive anomaly (5.0 ohm.m) near Spring D.

3.3.3 TIR mapping survey

The ground-based TIR mapping was used to identify discrete groundwater discharge features that were not visible to the naked eye during the daytime (Figure 3.5). Specifically, this method detected three additional springs in the vicinity of Spring D (Springs A, B and C; Figure 3.2) at night during the May 2017 campaign. The approximate diameter of Springs A-D ranged from 0.20 to 0.45 m, based on the thermal imagery and where the temperature changed from 7 to 19°C. The size of the sand boils within the springs had diameters ranging from 0.005 to 0.15 m. The temperature of the springs (~19°C) was distinctively higher than the adjacent seawater and saturated sand (~7°C), and the measured ambient air temperature (10°C). The heat map showed that the flow direction of the springs followed the downward slope of the beach towards the sea. The temperature of the springs detected with the thermal camera was similar to the measured average temperature (21.2°C) of the discharging water in Spring D using the multi-parameter probe at low tide (Table 3.1). Temperature data from regional groundwater and the springs was higher, compared to seawater and ambient air. Average groundwater temperature from the Qa and PWF aquifers was 18°C and 23.4°C, respectively. Whereas average groundwater temperature from the deeper MS and BR aquifers was 21°C and 22.8°C, respectively (Table 3.1).

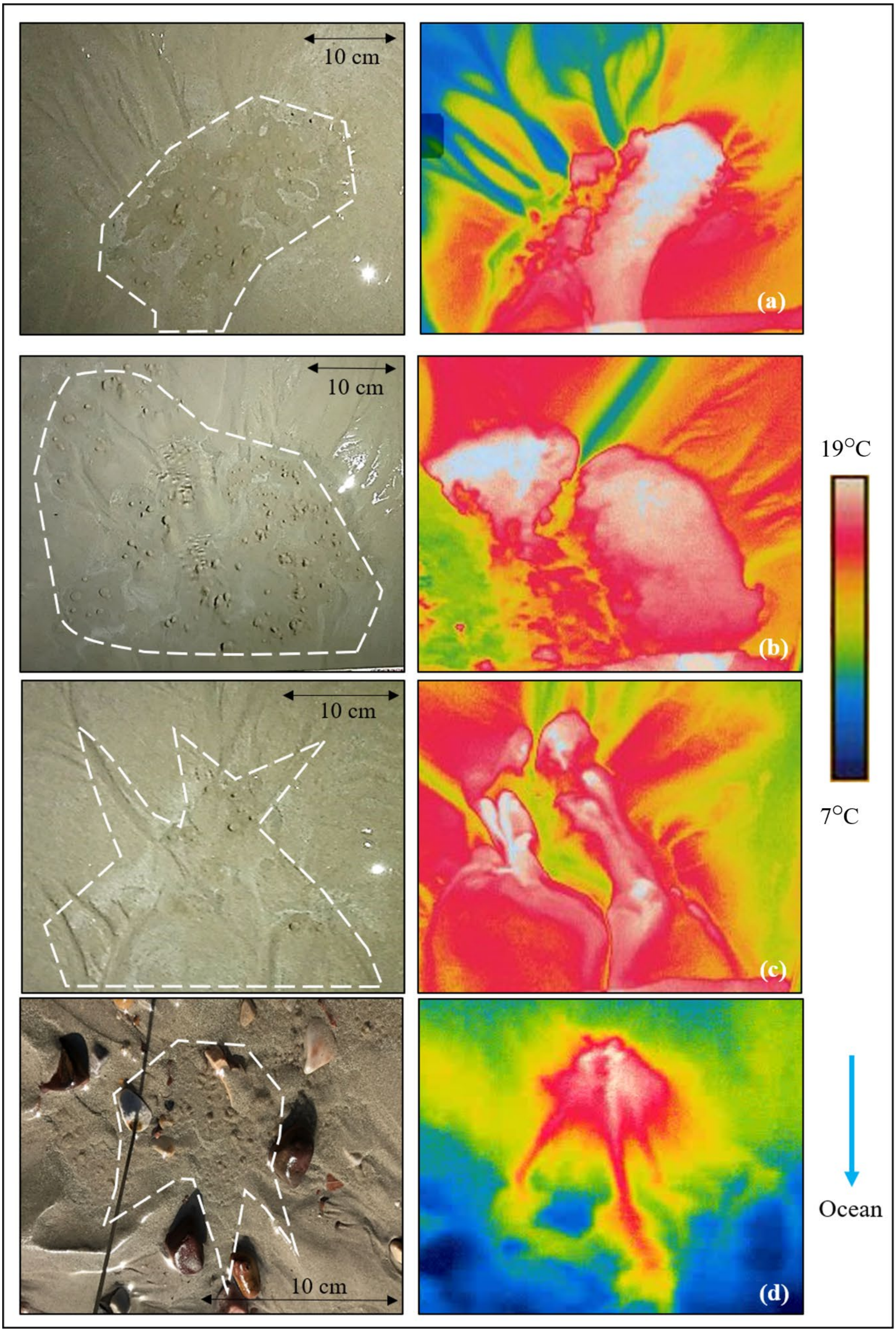
10 cm
(a)
10 cm
(b)
19°C
7°C
10 cm
(c)
10 cm
(d)
Ocean

Figure 3.5. Visible light and thermal images of the four intertidal springs from the 2017 field campaign. (a) Spring A, (b) Spring B, (c) Spring C, and (d) Spring D. The dashed white circles shown in the visible light images highlight the location of spring discharge and the sand boils within the springs. For spring location, see Figure 3.2. The black arrow shows the downward slope of the beach towards the sea.

3.3.4 EC, pH and stable isotopes of water

EC (measure of salinity), pH, $\delta^{18}O$ and $\delta^{2}H$ data from the springs, seawater, and regional groundwater from the Willunga Basin are given in Table 3.1. There was significant variability in the EC between sampling campaigns and the four major springs. Spring D (2017 campaign) had an average EC value of 24.8 mS/cm at low tide, whilst at mid to high tide the EC was 47.3 mS/cm. At low tide, the average EC recorded in Springs E and F (2019 campaign) was 16.7 mS/cm, whereas Spring G (2020 campaign) had a lower average EC of 13.1 mS/cm at low tide. In comparison, the measured average seawater EC was 56 mS/cm during the 2017 campaign, whereas during the 2020 campaign it was 54.4 mS/cm. Average salinity values from regional groundwater from the Qa and PWF aquifers (see Figure 2.1 for well locations) was 15.7 mS/cm and 3.95 mS/cm, respectively. Whereas average salinity values from the deeper MS and BR aquifers (see Figure 2) was 2.3 mS/cm and 5.16 mS/cm, respectively.

Table 3.1. $\delta^{2}H$ and $\delta^{18}O$, EC, pH and temperature data from sampled springs D, E, F and G, seawater, local rainfall, and regional groundwater from the Quaternary aquifer (Qa), the Port Willunga

Formation (PWF), the Maslin Sands aquifer (MS) and the basement rocks (BR). See Figure 2.1 for location of the regional groundwater monitoring wells. Elevation data and water levels are reported in metres above the Australian Height Datum (m AHD, approximately mean sea level). ND = no data. NA= not applicable.

Sample source	**Sample date/time**	**Tide level**	**Easting**	**Northing**	**Elevation**	**$\delta^{18}O$**	**$\delta^{2}H$**	**EC**	**T**	**pH**
					(m AHD)	**(‰, VSMOW)**		**mS/cm**	**°C**	
Spring D	24/05/17 9:45	low	267879	6086627	0.6	-2.4	-13.3	27.7	20.6	7.31
	24/05/17 19:30	high				1	6.3	54.3	20.2	7.74
	24/05/17 22:30	mid				-0.4	-1.5	55.8	20.6	7.54
	25/05/17 10:10	low				-2.8	-16.4	26.7	21.3	7.03
	25/05/17 23:00	mid				-0.5	-2.6	31.8	21.1	7.59
	26/05/17 11:30	low				-3.6	-20.5	20.2	23.3	7.28
	26/05/17 11:00	low				-2.5	-15.2	ND	ND	ND
Spring E	14/11/19 12:09	low	267880	6086627	0.08	-3.9	-21.4	16.9	18.3	6.98
	14/11/19 12:37	low				-3.9	-21.8	16.5	21.0	6.97
Spring F	14/11/19 13:02	low	267866	6086638	-0.37	-3.8	-21.4	17.0	21.1	6.88
Spring G	17/09/20 11:28	low	267866	6086635	-0.18	-3.9	-23.1	13.2	18.3	6.88
	17/09/20 11:45	low				-4.2	-24.0	13.2	18.5	6.81
	17/09/20 12:00	low				-4.4	-25.2	13.3	17.6	6.91
	17/09/20 12:12	low				-4.2	-24.5	13.0	17.6	6.84
	17/09/20 12:29	low				-4.2	-24.4	13.4	17.3	6.96
	17/09/20 12:59	low				-4.4	-24.9	12.9	18.6	6.7
	17/09/20 13:15	low				-4.4	-25.0	13.2	19.5	6.83
	18/09/20 10:03	low				-4.4	-25.1	13.0	22.1	6.87
	18/09/20 10:19	low				-4.4	-24.7	12.9	21.8	6.84
	18/09/20 10:36	low				-4.3	-24.2	13.0	21.7	6.74
	18/09/20 10:50	low				-4.4	-24.7	13.1	21.6	6.77
	18/09/20 11:20	low				-4.4	-25.5	13.2	21.8	6.85
	18/09/20 11:35	low				-4.4	-25.3	13.1	22.4	6.84
	18/09/20 11:50	low				-4.4	-25.0	13.1	23.1	6.8
	18/09/20 12:15	low				-4.4	-25.0	13.0	22.7	6.86
	18/09/20 12:33	low				-4.4	-25.0	12.9	22.7	6.79
	18/09/20 13:15	low				-4.3	-25.1	13.0	23.5	6.85
	18/09/20 13:30	low				-4.8	-26.0	12.9	23.3	6.76
	18/09/20 13:50	low				-4.7	-25.4	12.9	23.1	6.83

Seawater	24/05/17 9:45	low	267832	6086627	NA	0.8	5.0	57.0	19.8	7.7
	24/05/17 22:30	high				0.6	2.4	56.6	18.8	7.84
	25/05/17 19:00	mid				0.9	5.5	56.2	19.6	ND
	17/09/20 11:00	low	267830	6086640	-0.5	0.9	5.5	54.4	14.9	7.69
	17/09/20 11:30	low				1.1	6.7	54.5	14.7	7.74
	17/09/20 12:00	low				1.0	6.6	54.8	14.7	7.57
	17/09/20 12:29	low				1.0	6.6	54.9	14.9	7.58
	17/09/20 13:00	low				0.8	4.6	54.0	14.9	7.72
	18/09/20 9:31	low				1.1	6.0	54.5	18.0	7.79
	18/09/20 10:08	low				1.0	5.9	54.5	16.3	7.84
	18/09/20 10:36	low				0.9	5.9	54.1	16.2	7.82
	18/09/20 11:07	low				0.8	4.4	54.3	18.9	7.67
	18/09/20 12:00	low				0.9	5.0	54.2	17.3	7.65
	18/09/20 12:36	low				0.8	5.0	54.6	18.8	7.77
	18/09/20 13:00	low				0.8	4.2	54.1	18.1	7.74
	18/09/20 13:30	low				0.8	5.1	54.6	18.0	7.59
	18/09/20 13:50	low				0.9	5.2	54.2	20.3	7.7
Rainfall	05/17	NA	273533	6129692	2.0	-3.9 -5.3 -3.5	-18.7 -24.8 -12.5	ND	ND	ND
Qa	03/08/11	NA	268211	6090419	12.0	-4.6	-21.3	17.8	17.7	7.9
	05/08/11		268342	6089792	6.0	-4.3	-20.7	13.7	17.7	8
	29/08/11		268979	6091009	17.0	-4.6	-21.6	15.6	18.5	7.6
PWF	06/02/13	NA	268134	6092241	19.1	-4.6	-21.6	4	21.5	7.1
	06/02/13		268139	6092241	18.9	-4.2	-20.3	6	ND	7.3
	07/02/13		268652	6092289	20.9	-4.7	-21.3	3.1	24.2	7.4
	07/02/13		268655	6092289	20.9	-4.7	-23.6	2.7	24.6	8.1
MS	01/04/13	NA	275556	6096525	60.9	-5.1	-29.3	2.5	22.2	6.67
	01/10/12		277909	6099383	63.3	-5.4	-29.3	2.7	19.5	7.04
	01/04/13		281190	6103272	96.3	-5.2	-28.9	1.7	21.3	6.38
BR	01/03/14	NA	280643	6096705	182	-4.9	-26.6	1.4	18	7.2
	01/05/14		284135	6102541	211	-5	-27	2	26	7.5
	01/03/14		283263	6102519	163	-5.5	-30.6	5.3	24.4	7

In the 2017 field campaign, Spring D had an average pH at low tide and mid-high tide of 7.2 and 7.6, respectively. Springs E and F (2019 campaign) had an average pH of 6.9 and Spring G (2020 campaign) had the lowest average pH (6.8) at low tide. The average seawater pH of the 2017 and 2020 field campaigns only varied between 7.7 to 7.8. Average pH values from four observation wells in each of the regional Qa, PWF, MS and BR aquifers were 7.8, 7.4, 6.7 and 7.2, respectively (NCRIS Groundwater Database, 2022). Overall, the recorded pH in the springs from the three field campaigns was lower than in the adjacent seawater. Samples collected over the mid and high tide periods showed increasing pH, which corresponded with increases in salinity.

Rainfall isotope data from May 2017 were obtained from the Australian Global Network of Isotopes in Precipitation (GNIP) for Adelaide (BOM station: 94672; Bureau of Meteorology, 2020) and plot adjacent to the Adelaide Local Meteoric Water Line (LMWL) and varied from δ^2H -3.5 to -5.3 ‰, and δ^{18}O from -12.4 to -24.8 ‰ (Figure 8). Regional groundwater samples from the Qa aquifer (see Figure 2 for locations) had δ^2H values that ranged from -21.6 to -20.7 ‰ and δ^{18}O values that ranged from -4.6 to -4.2 ‰. In contrast, groundwater from the PWF aquifer showed relatively more depleted δ^2H and δ^{18}O values ranging from -23.6 to -20.2 ‰ and from -4.7 to -4.1 ‰, respectively. δ^2H and δ^{18}O samples from the deeper aquifers, the MS and BR, were more depleted than the overlying PWF and Qa aquifers, varying from -26.6 to -30.6 ‰ and from -5.5 to -4.9 ‰, respectively.

The δ^{18}O and δ^2H values of the springs fall to the right of the LMWL, with δ^2H varying from -20.5 to 6.3 ‰, and δ^{18}O from -3.6 to 1.0‰ for Spring D (2017 campaign) (Figure 3.5). Depleted values from Spring D were identified at low tide periods (δ^2H= -20.5 ‰, and δ^{18}O= -3.6 ‰), while more enriched δ^2H and δ^{18}O values (δ^2H= 6.3 ‰, and δ^{18}O= 1.0 ‰) were recorded during mid- to high tide, indicating likely mixing with seawater, which had average δ^2H and δ^{18}O values of 4.3 ‰ and 0.8 ‰, respectively. δ^{18}O and δ^2H data from the 2019 field campaign, showed depleted values at low tide for Spring E and F, with δ^2H varying from -21.8 to -21.4 ‰, and δ^{18}O from -3.9 to -3.8 ‰. At low tide, average δ^2H and δ^{18}O data from Spring G (2020 campaign) was more depleted (-24.9 ‰

and -4.4 ‰, respectively) than the 2017 and 2019 samples. While average δ^2H and δ^{18}O from seawater (2020 campaign) was 5.5 ‰ and 0.9 ‰, respectively.

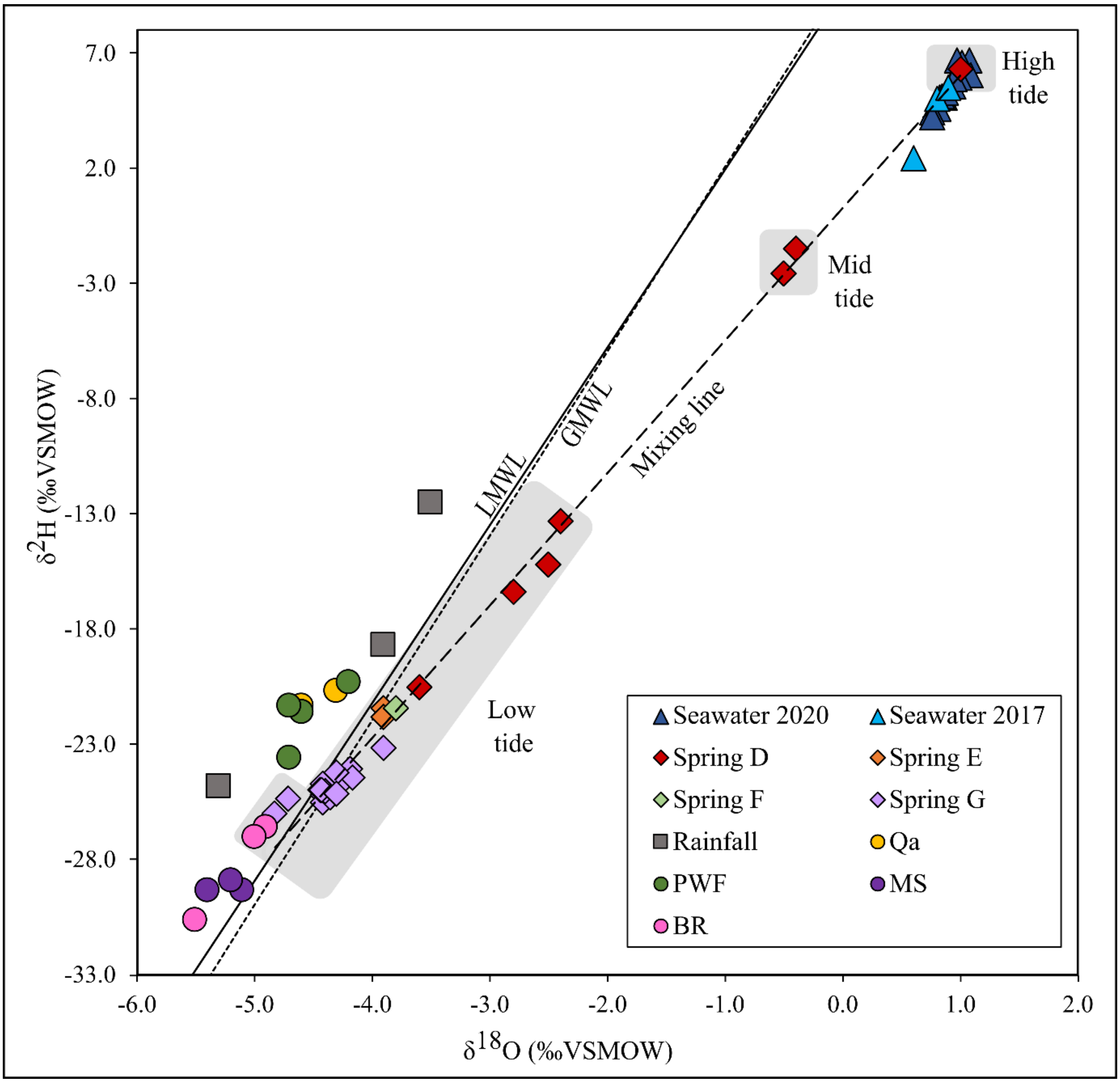

Figure 3.5. δ^2H versus δ^{18}O for sampled Springs D, E, F and G, seawater, regional groundwater and rainfall. The Adelaide Local Meteoric Water Line (LMWL) is $\delta^2H = 7.7\delta^{18}O + 9.6$ (Banks et al., 2009) and the Global Meteoric Water Line (GMWL) is $\delta^2H = 8\delta^{18}O + 10$ (dashed line; Craig, 1961). Regional groundwater includes samples from the Quaternary (Qa), Port Willunga Formation (PWF),

Maslin Sands (MS) and basement rock (BR) aquifers. The spring water mixing line between the end members of seawater and regional groundwater is $\delta^2H = 5.9\delta^{18}O + 0.5$ with and R^2 value of 0.99.

The proportion of regional groundwater (GW) and seawater (SW) mixing at Spring D was approximated using a simple binary-mixing approach (Table 3.2). Mixing calculations using average $\delta^{18}O$ values from Spring D at low tide from the 2017 campaign (-2.8 ‰), PWF (-4.6 ‰) and seawater (0.9 ‰) end-members, showed that spring discharge was comprised of approximately 67% groundwater (PWF). At high tide, the more enriched average $\delta^{18}O$ (1.0 ‰) values from Spring D showed a high proportion of seawater (86%) and lower groundwater contribution (14%). Mixing calculations for Springs E and F (November 2019), using average $\delta^{18}O$ (-3.8 ‰) at low tide, resulted in a similarly high proportion of groundwater contribution (86%) at the springs. Mixing calculations using average $\delta^{18}O$ data from Spring G (2020 campaign) at low tide (-4.4 ‰) also showed high groundwater contribution (97%) to the spring mixture. Additional mixing calculations using δ^2H and EC data indicate that δ^2H data tends to overestimate the groundwater contribution to the springs compared to calculations based on $\delta^{18}O$ and EC (Table 3.2).

Table 3.2. Binary mixing calculations between groundwater (GW) and seawater (SW) end-members using $\delta^{18}O$, δ^2H and EC data.

Groundwater-Seawater mixing								
Percentage (%)	2017				2019		2020	
	Low tide		High tide		Low tide		Low tide	
	GW	SW	GW	SW	GW	SW	GW	SW
δ^2H	81	19	14	86	99	1	100	0

$\delta^{18}O$	67	33	14	86	86	14	97	3
EC	60	40	18	82	76	24	82	18

The GW-SW mixing processes of the springs are presented in the EC vs δ^2H plot (Figure 3.6). There are two well distinguished groups of samples, represented at the left side of the plot by regional GW (average δ^2H and EC values of -24.8 ‰ and 6.0 mS/cm, respectively), and on the right by the SW end-member (average δ^2H values of 4.3 ‰ and average EC of 56.6 mS/cm). The average $\delta^{18}O$ and δ^2H composition of the springs (-3.7 ‰, and -20.7 ‰, respectively) was similar to both the isotopic signature of the nearby Qa ($\delta^{18}O$= -4.5‰ and δ^2H= -21.2 ‰) and PWF aquifers ($\delta^{18}O$= -4.6 ‰ and δ^2H= -21.7 ‰), but significantly differed from the composition of the MS ($\delta^{18}O$= –5.2 ‰ and δ^2H= -29.2 ‰) and BR ($\delta^{18}O$= -5.1 ‰ and δ^2H= -28.1 ‰) aquifers. Our mixing processes analysis (Figure 3.6) shows that the isotopic values of the springs more closely resemble those of the upper aquifers (Qa and PWF), rather than the deeper MS and BR aquifers, which show isotopic signatures that are more depleted. These results indicate that the GW contribution most likely originates from the upper aquifers rather than the MS and BR aquifers. However, given that there is no major difference in their isotopic composition, we cannot accurately determine which aquifer is the main supplier of fresh GW to the springs.

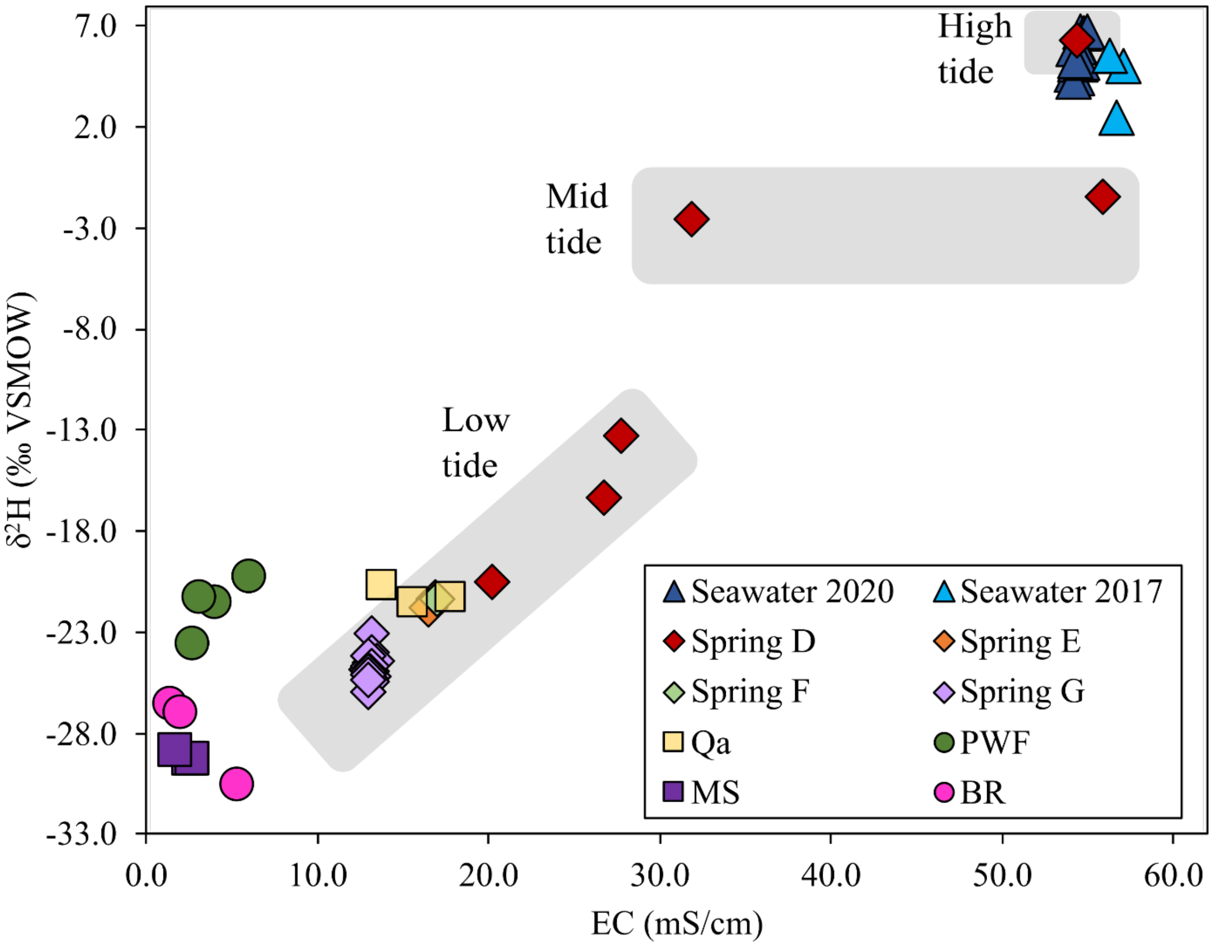

Figure 3.6. δ^{2}H versus EC for sampled Springs D, E, F and G, regional groundwater and seawater samples. Regional groundwater samples include the Quaternary (Qa), Port Willunga Formation (PWF), Maslin Sands (MS) and basement rocks (BR) aquifers.

3.3.4 Time series water level observations

Time series water level observations from the shallow piezometer installed in Spring D together with measured sea levels offshore from the study site for the May 2017 field campaign are shown in Figure 3.7. Over the field campaign period, sea level reached its maximum at ~1.0 m AHD at high tide, and then decreased to 0.4 m AHD at low tide. During high tide periods Spring D was fully inundated by seawater. Analysis of the measured sea and water levels over the 4 days of monitoring showed that the spring response to tidal sinusoidal oscillations varies asymmetrically at the location of Spring D, and that spring water levels are dependent on tidal range between 0.65 m AHD (high tide) to -0.46 m AHD (low tide).

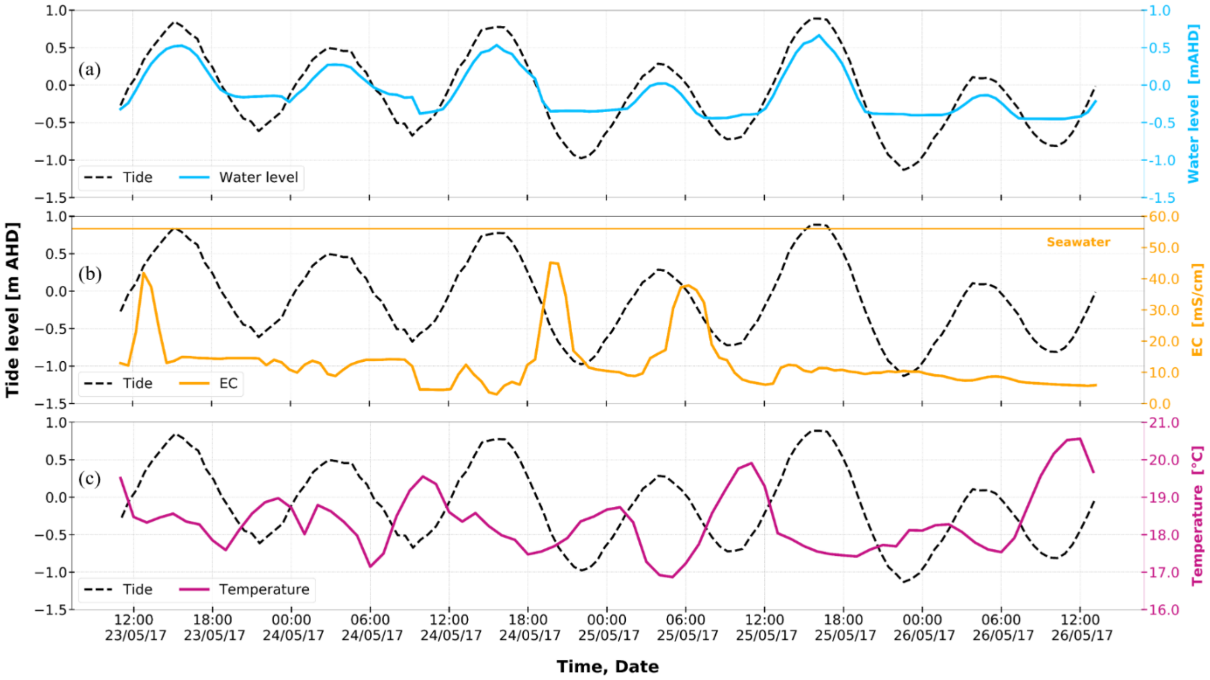

Figure 3.7. Temporal variations of (a) water levels, (b) EC and (c) temperature at Spring D and ocean tide (dashed line) during 23-26 May 2017.

Time series measurements of EC at Spring D also showed a change in salinity with the tidal cycle (Figure 3.7c). During high tide periods the average salinity was ~44 mS/cm, compared to low tide, where the salinity of Spring D reached its minimum of ~1.89 mS/cm. The time series EC results were consistent with measurements that were taken with a handheld YSI EC meter, where a maximum EC of 55.8 mS/cm was recorded during or shortly after high tide, and a minimum EC of 20.2 mS/cm observed during low tide periods. These salinity fluctuations with time show the influence of mixing seawater at the spring, where increasing salinity correlated to high tide periods, when Spring D was inundated by seawater. Over the measurement period, a time lag in the change in salinity at Spring D was occasionally observed. For example, on May 24, the high tide was recorded at 15:39, while the highest EC (53.3 mS/cm) was recorded at 19:38, ~3 hours later (Figure 3.7).

The average water temperature of Spring D was 18.4°C, with a maximum value of 20.7°C recorded at low tide, and minimum of 16.8°C during high tide (Figure 3.7b). In comparison, handheld measurements using TIR imagery at low tide showed average spring temperature values of 21.3°C and seawater of 19.4°C. The presence of seawater during high tide periods was represented by low temperature values (~17°C), while daytime observations at low tide (i.e., 23/05/17, 11:00) showed increased temperatures values (~20°C). Overall, these early winter transient temperature patterns seemed to be influenced by the interaction of ocean tides and solar radiation.

3.4 Discussion

3.4.1 Spring and sand boils observations

Results from the intertidal observations undertaken by this study during the three field campaigns (May 2017, Nov 2019 and Sept 2020), demonstrated the seasonal variability of the surface expression of the Sellicks Beach springs. From visual observations, the largest spring (Spring F; Figure 3.1), with an approximate diameter of 0.50 m, was identified in the late spring campaign (Nov 2019). The diameter of the sand boils within Spring F were identified as the largest throughout this study (~0.1 m). In the winter campaign (May 2017) Spring A was identified at night with the TIR camera and had an approximate diameter of 0.30 m. However, the diameter of the sand boils within Spring A were significantly smaller (~0.01 m) compared to Spring F. Given the close proximity between the locations of Springs A and F (~1.5 m; Figure 3.2), the continual changes in the geomorphology of the beach and the sand deposition, these two springs are considered to be the same spring. Nevertheless, the internal mechanisms that control the surface characteristics of the sand boils (e.g., sand boil diameter) within the springs should be considered in future studies.

At Sellicks Beach, previous studies have identified that the PWF cliffs and platforms have experienced significant erosion (May and Bourman,1984; Bourman et al., 2016). Particularly, Cann et al. (2014) conducted field observations at Sellicks Beach for over forty years and described the erosion and distribution of beach sediments at Sellicks Beach. They attributed the origin and transport of the gravels, located at the high-tide level of the beach, to coastal and rainfall erosion of the alluvial fan sediments and the PWF cliffs (Figure 3.3). They concluded that sediment transport along Sellicks Beach is predominantly influenced by seasonal changes. Specifically, longshore sediment transport occurs during wintertime when wave energy is high. These seasonal erosion and sediment transport mechanisms are likely to influence the surface expression of the intertidal springs. For example, the seasonal variation of sand thickness that overlays the PWF rocks can provide distinctive preferential flow paths and may be a controlling factor of the temporal changes of the location and occurrence of the springs and sand boils.

3.4.2 Structural controls on spring discharge

Previous studies that focused on groundwater discharge to the sea from the Willunga Basin (Martin, 1998, Lamontage et al., 2005) suggested diffuse discharge along the coastline. However, this study demonstrated that discrete discharge from the basin can also occur as intertidal springs. The reason for the occurrence of this point discharge seems to be structural and linked to the faults and fractures identified in the area, associated with neotectonic activity (Jayawardena 2013; Lubiniecki et al. 2019). The nearby outcropping Willunga Fault is a clear example of the structural complexity at Sellicks Beach, where additional active faults, deformation bands, and land slumping have been identified in the Port Willunga Formation cliffs (Preiss, 2019) and platforms. Evidence documented by Reed (1982) of the faults at the top of the PWF cliffs (Figure 3.2), approximately 200 m from the study site, brings to mind the possibility that this set of faults can extend towards the ocean and could have a greater influence in the creation of the preferential flow paths that control the intertidal seeps. Further geophysical investigations can help in the mapping and detection of the faults within the intertidal zone and determine their extent towards the ocean.

3.4.4 EC, pH and stable isotopes of water

Intertidal spring $\delta^{18}O$ and $\delta^{2}H$ composition is characterised by a considerable tidal and seasonal variability. Isotope enrichment was observed at high tide, where seawater inundates the springs. Additionally, winter samples were more enriched, compared to early-late spring values. Water mixing calculations using average $\delta^{18}O$, $\delta^{2}H$ and EC data also showed seasonal variability. In the winter campaign (May 2017) at low tide periods, the average groundwater contribution to spring discharge was 69%, while during high tide periods this decreased to 15%. For the late and early spring campaigns (Nov 2019 and September 2020, respectively), the average groundwater contribution to the springs at low tide was 87% and 93%, respectively. These seasonal comparisons correlate to previous studies of the area that indicate that seasonal changes of seawater levels and wave energy can considerably influence the water composition of intertidal springs (Short et al., 2014; Cann et al., 2014). pH values also showed seasonal variations; during the spring campaign, the average pH was 7.4, while for the late and early spring campaigns the pH ranged between 6.8 and 6.9.

3.4.5 Time series analysis

The response observed in the water level and tidal data can be attributed to filtering processes occurring at the beach (Lanyon et al., 1982), something which has previously been observed in estuarine settings (e.g., Carey et al., 2009). In Figure 10(a), the flat sections in the water levels of Spring D are indicative of seepage face formation at the beach, whereby the head at the point of discharge levels out at an elevation close to the land surface. Similar patterns have been observed in other studies of intertidal zones (e.g., Turner, 1993; Li et al., 2006; Carey et al., 2009). At low tide periods, spring water discharge occurs in the intertidal zone because the water levels in Spring D remain above seawater levels. Meanwhile, at high tide periods, tidal and wave action drive seawater to the intertidal zone, where it infiltrates and mixes with groundwater, causing seawater recirculation (Robinson et al., 2007; Heiss and Michael, 2014).

3.5 Conclusions

This study aimed to characterise intertidal springs identified as groupings of closely spaced sand boils, located in Sellicks Beach, South Australia, to better understand groundwater-surface water interactions in coastal environments. The combined use of EM geophysics and handheld TIR imagery proved to be a reliable, rapid and non-invasive methodology to locate and describe the surface expressions of the intertidal springs and their spatial distribution in the subsurface.

$\delta^{18}O$ and $\delta^{2}H$ data indicated that isotope composition of the intertidal springs is characterised by a significant seasonal variability (winter and spring), and isotope enrichment due to groundwater-seawater mixing processes and tidal variations. We may conclude that water from the springs is controlled by a mixture of two main end members, fresh regional groundwater and seawater. With different proportions of groundwater in the mixture, i.e. up to 100% at low tide in early spring 2020 and down to 14% at low tide in early winter 2017. However, our results cannot accurately determine which aquifer is feeding the springs or if it is mainly a combined contribution due to the complex multi-aquifer setting. Temperature time series measurements and water levels at spring D showed variations strongly driven by the tidal cycle. Additional handheld temperature measurements and TIR imagery revealed clear contrasts between seawater, spring water and the surrounding saturated sediments.

The presence of intertidal springs in Sellicks Beach is likely a result of the structurally complex nature of the area. The cliffs and outcropping intertidal platforms display faults and fractures that provide preferential flow paths for groundwater flow. A more comprehensive characterisation of the fractured rock system underneath the beach sand would enhance our current understanding of the source and structural, geological controls of the springs. Future work should develop a temporal assessment of the springs to better understand their seasonal variability, including spring heads and discharge. Also, sediment transport analysis would be greatly beneficial to characterise and understand the release of water and sediment from intertidal sand boils within springs.

Chapter 4

Sediment characterisation of intertidal sand boils

4.1 Introduction

The intertidal zone is the area of the beach that is exposed during low tide and becomes fully submerged during high tide. This zone is considered to be a vital transition zone between terrestrial and marine environments (Benkendorff, 2008). Intertidal groundwater discharge has been recognised as a process with an important ecological role because of the high nutrient input to the biological habitat that this zone represents (Miller and Ullman, 2004; Waska and Kim, 2011). Furthermore, groundwater discharge is known to modify the geomorphology of beaches, whereby high rates of groundwater discharge tend to destabilise intertidal sediments (Bokuniewicz et al., 2008; Post et al., 2020). Therefore, the study of intertidal groundwater discharge is critical in understanding the ecological and physical processes that occur in this transitional zone.

In some cases, groundwater discharge to intertidal zones leads to the formation of sand boils, which are point discharge features with sufficient flow to mobilise and eject sand particles (Kolb, 1975; de Louw et al., 2010; Werner et al., 2020). Sand boils are often encountered near rivers and dams and within polders (Williams, 1974; de Louw et al., 2013; Van Beek et al., 2013), where the presence of upwelling groundwater from preferential pathways, and sediment mobilisation may initiate structural failure mechanisms (e.g., levee failure and river breach).

Sand boils field-based case studies have been conducted along the river Po in Northern Italy (Marchi et al., 2020, Aielli et al., 2019), where a total of 130 sand boils have been documented. They conducted size measurements and found sand boils with diameters > 3 m. They also collected water and sediment discharge measurements. Their grain size distribution analyses found that finer sand particles were ejected from the sand boils. Marchi et al. (2020) concluded that data obtained in their field investigations (diameter, depth, and particle size) is vital for the study of sand boil models.

Sand boils have been considered as important paths for groundwater movement (Guhman and Pederson, 1992). For example, Guhman and Pederson (1992) described sand boils in the Nebraska Sand Hills (USA), occurring mainly within 30 m of the Dismal River, that have existed for at least 100 years. They concluded that these sand boils are the primary path for groundwater flow to the surface within the area. Sand boil locations changed over time, with some becoming inactive while new sand boils formed in other locations. Guhman and Pederson (1992) found that sand boils extended to depths of ~40 m, while the dimensions of sand boil conduits showed significant changes, with diameters ranging from ‘pencil size’ to 10 m. The sand within the conduits was found to be well sorted, with finer particles ejected from the sand boils were carried away by river flow.

To study sand boils laboratory experiments have been undertaken to replicate these erosion mechanisms. Particularly, to understand the initiation of erosion mechanisms, Sterpi (2003) conducted a laboratory experiment where a vertical flow in silty sand was applied. Results indicated that erosion increased with time under a constant hydraulic gradient. For soil stability studies, Wan and Fell (2004) used various sediments, such as gravel, sand and clay and applied upward and downward water flows. Their results indicated that suffusion starts at lower hydraulic gradients (0.8 or less) that previously predicted in the theory described by Terzaghi (1922). Terzaghi (1922) showed the gradient (1.0) required to cause heave, sand boils and boiling sand in both cohesive and non-cohesive sediments.

Ahlinhan and Achmus (2010) studied stable and unstable non-cohesive soils and conducted numerous laboratory experiments. They used horizontal and upward flow to study the hydraulic gradient at which suffusion initiates. Their results revealed that for unstable soils, the critical hydraulic gradient for upward flow somewhat depends on the relative density, which is a marker of the level of compaction in non-cohesive soils. Townsend et al. (1988) and Schmertmann (2000) studied the minimum gradient for piping in the lateral direction in clean, fine, uniform sands. Their experiments showed gradients as low as 0.08. Yang and Wang (2017) also conducted laboratory experiments on stable and unstable sand, they compared their measured hydraulic gradient to predicted hydraulic gradient models (theory based), and their results indicated that no single predicted model applies to all types of soil.

In Australia, sand boils have been identified along the shoreline of Sellicks Beach. Observations made by Ramirez-Lagunas et al. (2022) found a total 7 sand boils within the intertidal zone of Sellicks Beach, South Australia. The sand boils were exposed during low tide periods and fully inundated by seawater at high tide. The size of the sand boils had diameters ranging from 0.005 to 0.15 m. Their average EC results showed fluctuations with time (24.8 mS/cm), increasing salinity values were recorded during high tide periods (47.3 mS/cm). Results indicated that water discharged from the sand boils is the result of groundwater-seawater mixing. Their study concluded that further investigations are needed to understand the dynamics of sand boils and their impact on the complex physical processes within intertidal zones.

Grain size distribution analyses can provide a valuable insight on sediment transport, source, and environment characteristics (Folk and Ward, 1957; McLean and Kirk, 1969). Beach sediment characteristics like grain size distribution patterns and degree of sorting have been widely studied (Griffiths, 1951; Klein et al., 2005; Nugroho and Putra, 2018), including the impact of hydraulic forces (e.g., wave action) on beach sediments (Inman, 1949; Folk, 1962). However, the impact of hydraulic forces due to the presence of sand boil in beach settings has not been explored. Therefore, further research is needed to understand the effects of sand boils on sediment transport and how they may impact the existing grain size distribution and sorting patterns in intertidal settings.

According to Komar (1998), the main factors that control mean grain sizes of beach sediments are the source of the sediments, the wave energy levels and the slope of the beach. Short and Wright (1983) classified beach environments according to their wave and sediment characteristics into three types, reflective, intermediate, and dissipative. Reflective beaches display low waves, steep slopes, coarse sediments, and narrow intertidal zones. Intermediate beaches are dynamic with moderate waves and medium size sediments. Meanwhile dissipative beaches present higher waves, low beach slopes, abundant fine sediments, and wide intertidal zones. Dissipative beaches experience minimal spatial longshore variability (Sherman, 2019).

The aim of this study is to investigate the sediment characteristics of the intertidal sand boils located in Sellicks Beach, South Australia. The methodology involved quantifying the grain size distribution and characterising the spatial variability in the intertidal zone and within a sand boil. Additionally, sand boil dimensions, sand thickness, permeability, hydraulic conductivity, and water discharge measurements were obtained to further understand the impact of sand boils in an intertidal environment. This study describes the first published attempt (to the authors' knowledge) to obtain detailed sediment characteristics of intertidal sand boils, thereby adding to the existing knowledge base of intertidal hydrological processes.

4.2 Methods

Field investigations were conducted from 17 to 18 September 2020, at the southern end of the Sellicks Beach coastline (Figure 1), where intertidal springs occur as groupings of closely spaced sand boils. Field activities included beach sediment sampling (samples from the sand boils and surrounding area within the intertidal zone), measurements of the thickness of the sand sediments overlying the PWF, observations of sand boil dimensions and spring discharge measurements.

4.2.1 Sediment sampling

For the sediment collection activities, a grid was designed (Figure 4.1) to better represent the sediment distribution within the sand boil and its surroundings. The activities consisted of collecting a total of 72 sediment samples, at various depths (surface, 5, 10 cm and 15 cm) at each site. Samples were stored in airtight plastic bags to prevent cross-contamination and humidity. The locations of each sampling site were recorded using a Real Time Kinematic (RTK) positioning instrument (www.trimble.com). For the grain size distribution analysis, all sediment samples were oven-dried at 110°C for 24 hours. The analysis was conducted using a set of standard stainless-steel sieves, with mesh sizes ranging from 19 to 0.075 mm, the sieves were stacked and placed on a mechanical sieve shaker and each sample was shaken for 35 mins.

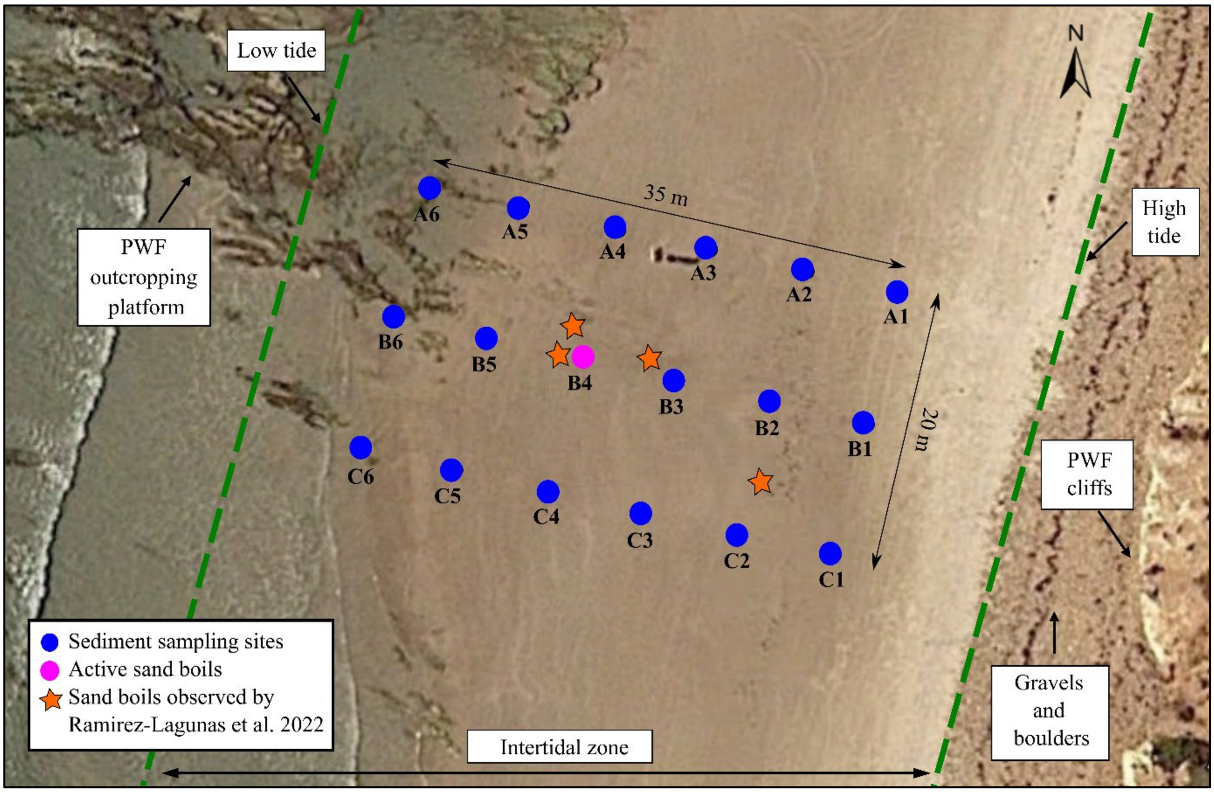

Figure 4.1. Location of the sediment sampling sites (blue circles), active sand boil (magenta circle) and sand boils previous observed (orange stars) by Ramirez-Lagunas et al. (2022), within the intertidal zone of Sellicks Beach. The green dashed lines represent average low and high tide levels (Bureau of Meteorology, 2020).

The process of preparing samples for grain size analysis involves initially drying each sample in an oven at 110°C for a duration of 24 hours. Subsequently, once the samples have undergone drying and cooling, the next step involves sieving them using a machine equipped with a "shaker" instrument.

The selected sieve opening sizes are as follows: 19 mm, 9.5 mm, 4.75 mm, 2.36 mm, 1.18 mm, 1 mm, 0.71 mm, 0.5 mm, 0.425 mm, 0.25 mm, 0.18 mm, 0.15 mm, 0.125 mm, and 0.075 mm. To ensure the stability of the sieving column, given the number of sieving pans, each sample is divided and sieved in two separate stacks. Each stack undergoes shaking for a standardized duration of 35 minutes.

4.2.2 Porosity and permeability

Porosity of the sediment samples was calculated with the water saturation method. The method consisted in saturate the samples in an oven proof container of know volume, weight both the empty container and the container with the fully saturated sample with water of known density and proceed to oven dry it for 24 hours at 110°C. Porosity was calculated using equation 1. This method was applied three times per sample to obtain the average porosity.

$$n = \frac{Vv}{Vt}$$

Where n is porosity, Vv is void volume (ml) and Vt is total volume (ml) of the sample.

After the average porosity was calculated the next step is to calculate the permeability k, of the samples using Kozeny's (1927) permeability model:

$$k = c_o \frac{d^2}{36} \frac{n^3}{(1-n)^2}$$

Where n is porosity, d is the mean grain diameter and c_o is a constant that can vary from 1/2 (assuming capillary tubes have circular cross-sections) to 1/6 (Carman, 1937).

The mean grain diameter d was calculated as suggested by Folk and Ward (1957), which considers particle diameters, such as d_{16} or d_{50} and d_{84} (diameters at which 16%, 50% and 84%) of the samples, that were obtained in the previous grain size distribution analyses.

$$log_2 d = \frac{log_2 d_{16} + log_2 d_{50} + \ log_2 d_{84}}{3}$$

The calculated hydraulic conductivity K, was obtained using the following equation:

$$K = \frac{k \times \rho \times g}{\mu}$$

Here, k is permeability, ρ is density of the sand boil water (999.74 kg/m^3), g is gravity (taken as 9.81 m/s^2) and μ is the dynamic viscosity of the water (8.90E-04 kg/ms at 25°C).

4.2.3 Hydraulic conductivity

In addition to the calculated hydraulic conductivity of the sediment samples, the KSAT meter (Figure 4.2) was used to obtain and compare hydraulic conductivity values. The KSAT meter is an instrument designed by METER Group Inc. and measures the saturated hydraulic conductivity of soils with the constant or falling head methods. The falling head method is recommended for all samples, disregarding their permeability, by the instrument developer and is considered to provide extremely precise fully automated measurements. For the constant head method, a capillary tube with a sealing cap is needed, and it is installed in the burette. This semi-automated method requires manual readings at selected intervals.

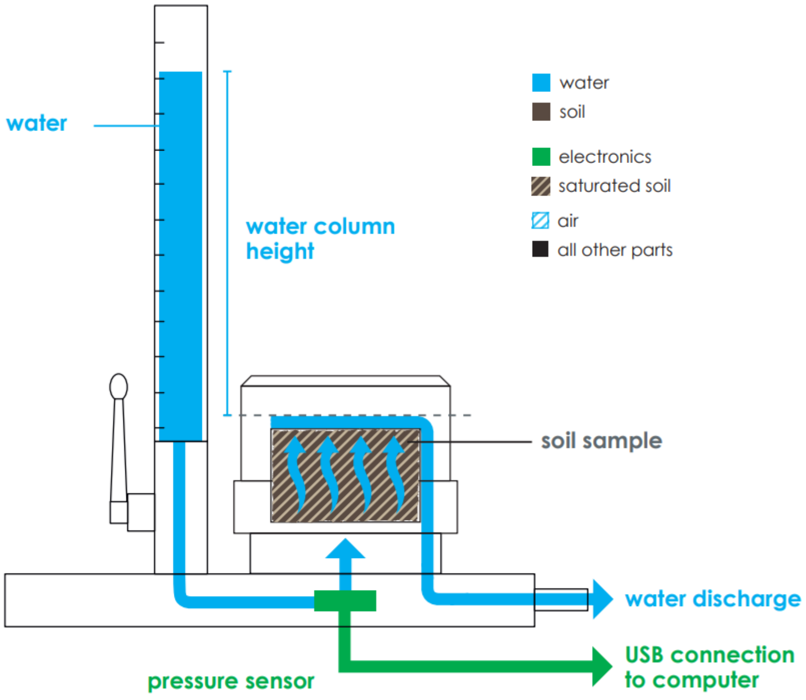

Figure 4.2. KSAT meter schematics (metergroup.com).

The preparation procedure involved filling a 250 ml soil sampling ring with sediments. Subsequently, the saturation plate and filter paper were positioned atop the ring, followed by placement in a container with approximately 2 cm of water. After a 45-minute waiting period, the water level was elevated nearly to the ring's height. The red sealing, along with the porous plate, was then placed and saturated. The setup was inverted, and after removing the saturation plate and filter paper, saturation was continued for an additional hour. After the sample was saturated, the sample was placed in the KSAT meter, and using the software provided by METER Group Inc., the measurements can begin. To compare results, both hydraulic conductivity measuring methods were used.

The samples that were used in the hydraulic conductivity measurements (KSAT) were obtained from sediment collected during the 2020 field campaign. It is important to acknowledge that this approach diverges from the ideal undisturbed in-situ hydraulic conductivity measurement protocol. Nonetheless, it is adopted to facilitate a practical and representative assessment of the sediment's hydraulic behaviour.

4.2.4 Water flow

Flow measurements were conducted by ringing the spring (location B4 in Figure 4.2.1) using the top half of a plastic bucket to allow collection of the flow into a 750 ml rectangular container over 5 recorded time intervals. Measurements were conducted at low tide.

4.3 Results and Discussion

The active spring (location B4, Figure 4.1) identified at low tide during the field work activities is shown in Figure 4.3.1. The spring had an average diameter of 0.45 m and contained several (~50) bubbling sand boils. Within the spring discharge area, the sand thickness was 0.18 m, while at profile 1 (closest to the cliffs, Figure 4.1) the average thickness of sand was 0.72 m, while at profile 6 (closest to the ocean, Figure 4.1) the average sand thickness was 0.44 m. These results indicate a decrease in sand thickness towards the ocean.

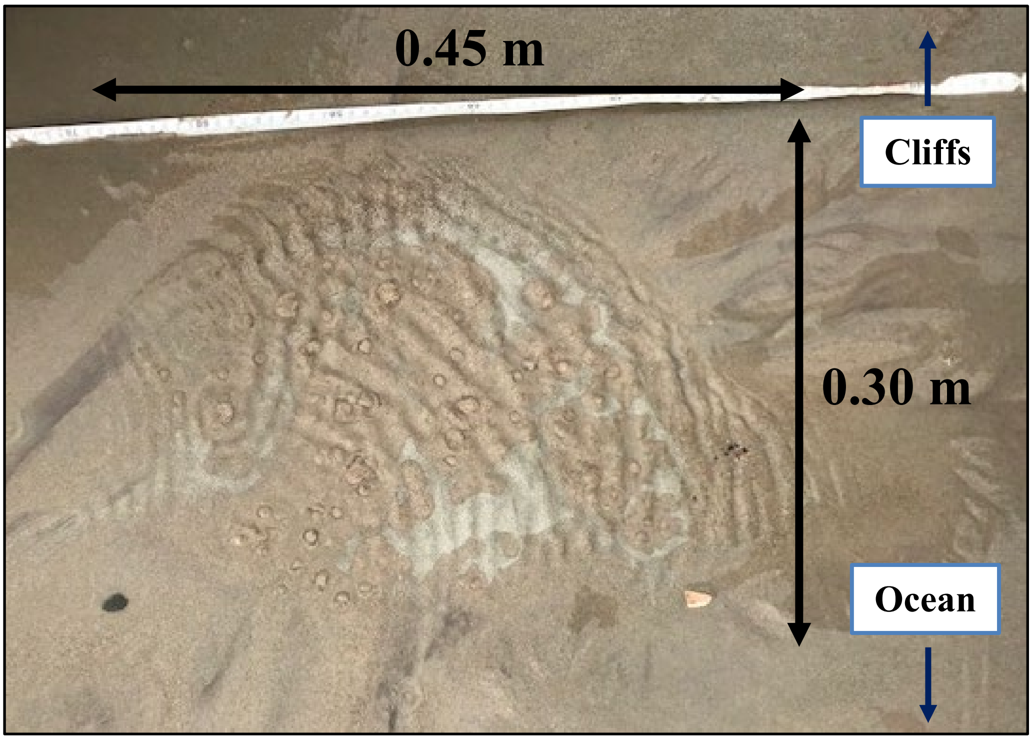

Figure 4.3.1. Sand boils within spring B4 (location shown in Figure 4.1)

4.3.1 Sediment size

Observations at the study site showed that at low tide a narrow sandy beach is exposed. Bigger clasts (e.g., gravels and boulders) are located above the high tide mark, near the PWF cliffs (Figure 4.3.2).

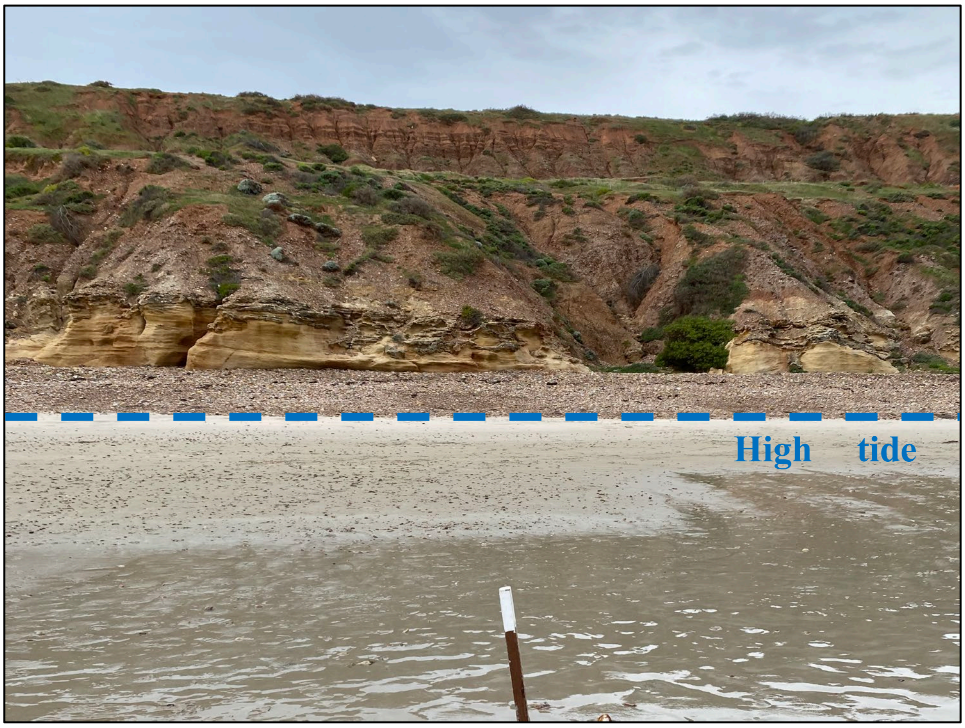

Figure 4.3.2. Photograph of the location of the sediment sampling activities, showing the narrow sand strip exposed at low tide periods and the presence of bigger clasts above the high tide line.

At the intertidal zone, sediment analysis with depth (surface, 5, 10 and 15 cm) showed the predominance of fine (64.37%) and medium (17.55%) sands (Table 4.3.1). Mean particle sizes of depth samples ranged from 0.20 to 0.24 mm. In terms of gradation, all samples were poorly graded, with all calculated Coefficient of Uniformity (Cu) values less than 1.9 and calculated Coefficient of

Curvature (Cc) less than 1. Beach sediments were thereby of fairly constant size in areas not impacted by sand boils.

However, one of the non-spring samples showed more diverse sediment sizes, particularly, at 15 cm depth. Sample A3 comprised mostly of fine sands (47.75%), medium sands (19.50%) and pebbles (12.78%). But at 15 cm depth the pebble content increased to 48.5%, while the fine and medium sand content decreased to 14.6% and 7.02%, respectively. Depth samples at A3 collected at 5, 10 and 15 cm were poorly/uniformly graded, with calculated Cu values of 1.3, 1.5 and 1.6, respectively.

Figure 4.3.3. Example of a non-spring sediment sample. Location C3 surface from Figure 4.2.1.

Table 4.3.1. Average percentage of each sediment classification at all non-spring locations (Figure 4.2.1). Size classes after Wentworth (1922).

Wentworth size class	Grain size (mm)	Percentage (%)
Pebble	>4 to 64	1.79
Granule	>2 to 4	1.60
Very coarse sand	>1 to 2	1.56
Coarse sand	>0.50 to 1	3.46
Medium sand	>0.25 to 0.5	17.55
Fine sand	>0.125 to 0.25	64.37
Very fine sand	>0.0625 to 0.125	9.63

Conversely, sediment sizes at sampling locations within the area of groundwater discharge were markedly more heterogeneous (Figure 4.3.4). At the spring, sediments comprised mostly of fine sands (35.21%), pebbles (27.73%) and medium sands (16.68%) (Table 4.3.2). Mean particle size at the surface, 5 cm, 10 cm and 15 cm depth were 0.49, 0.98, 1.18 and 2.63 mm, respectively. In terms of gradation, the surface sample was poorly/uniformly graded, with a calculated Cu value of 1.4 and Cc 0.6. Samples collected at 5, 10 and 15 cm were well graded, with Cu values of 12, 20.8 and 45.5, respectively.

Figure 4.3.4. Spring sediment sample. Location B4 surface from Figure 4.2.1.

Table 4.3.2. Average percentage of each sediment classification at the active sand boils within the spring (Figure 4.2.1). Size classes after Wentworth (1922).

Wentworth size class	Grain size (mm)	Percentage (%)
Pebble	>4 to 64	27.73
Granule	>2 to 4	9.91
Very coarse sand	>1 to 2	3.48
Coarse sand	>0.50 to 1	4.31
Medium sand	>0.25 to 0.5	16.68

Fine sand	>0.125 to 0.25	35.21
Very fine sand	>0.0625 to 0.125	2.68

Ramirez-Lagunas (2023) identified the intertidal springs at Sellicks Beach to be temporally and spatially variable. Kolb, 1975 and de Louw et al. (2010) have shown that, around the throat of a sand boil, elevated water fluxes cause sediment mobilisations, removing finer particles and pushing them upwards. Once the finer particles reach the surface, incoming tides are able to remove fine particles away from the sand boils, and possibly bringing in, at every tidal cycle, new sediments from nearby locations within the study site and ever further away. Based on this observation, it could be speculated that the non-spring location A3 is potentially a former active and now inactive sand boil location, given that bigger clasts with similar sizes to the active sand boils were found at 15 cm depth.

4.3.2 Porosity and permeability

Porosity (*n*) results revealed that at non-spring locations average porosity of the samples was 35%, with minimum and maximum values of 31% and 39%, respectively. Average porosity of the samples at the active spring was 27%, with minimum and maximum values of 26% and 29%, respectively. Porosity of sample A3 at 15 cm presented the lowest recorded porosity (25%) from all the samples, given that bigger grain sizes were found at that location. This correlates with findings from Ogolo et al., (2015) and Atapour and Mortazavi (2018), that porosity is inversely related to grain size and decreases as grain size increases. Additionally, porosity values are within the ranges established by Freeze and Cherry (1979) for sands and gravels. All porosity results can be found in Appendix 3.

Permeability (k) values were calculated using both 1/2 and 1/6 for the constant c_o established by Carman (1937; Equation 2). For $c_o = 1/2$, the average permeability from non-spring locations was 8.2x10^{-8} cm^2, with minimum and maximum values of 3.2x10^{-8} cm^2 and 3.2x10^{-7} cm^2, respectively. For $c_o = 1/6$, average permeability from non-spring locations was 2.7x10^{-8} cm^2, with minimum and maximum values of 1.1x10^{-8} cm^2 and 1.1x10^{-7} cm^2, respectively. Average permeability at the active spring for $c_o = 1/2$ was 6.2x10^{-7} cm^2, with minimum and maximum values of 4.4x10^{-7} cm^2 and 8.1x10^{-7} cm^2, respectively. While for $c_o = 1/6$, average permeability from non-spring locations was 2.1x10^{-7} cm^2, with minimum and maximum values of 1.5x10^{-7} cm^2 and 2.7x10^{-7} cm^2, respectively. Permeability of sample A3 at 15 cm for $c_o = 1/2$ was 3.0x10^{-6} cm^2 and for $c_o = 1/6$ was 1.0x10^{-6} cm^2. Permeability results are within the range established by Freeze and Cherry (1979; Figure 4.3.5) for sands and gravels.

Permeability results showed a negative correlation with porosity. Average higher permeability (7.3x10^{-7} cm^2) and average lower porosity (28%) was found in the spring samples, while non-spring samples presented average lower permeability (5.5x10^{-8} cm^2) and average higher porosity (35%). This correlates with the findings of Masch and Denny (1966) that indicated that grain size and porosity have an effect on the permeability of unconsolidated sediments, indicating that permeability tends to increase with increasing particle sizes. For this study, bigger particle sizes were found at the spring location (pebbles and sands), compared to the smaller particles (fine sands) at non-spring locations.

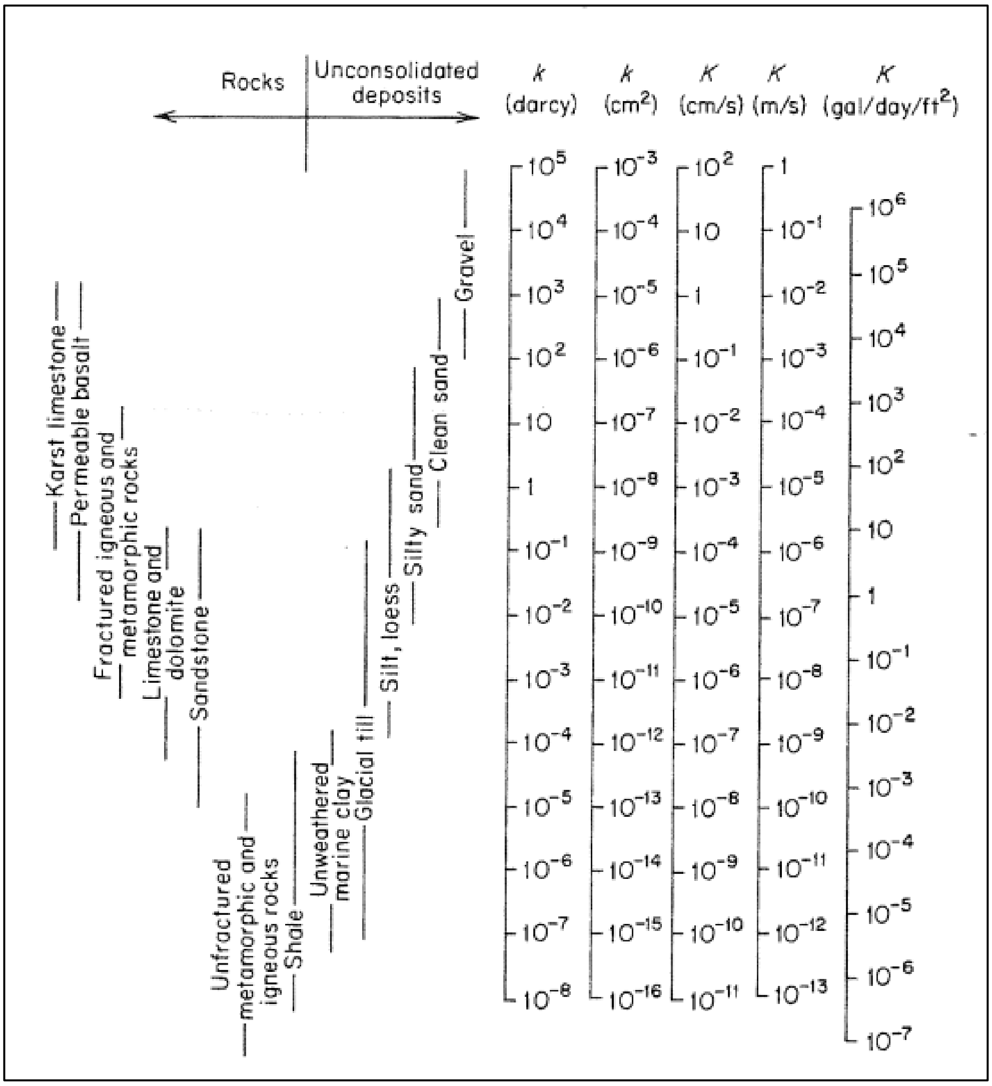

Figure 4.3.5. Values of permeability (k) and hydraulic conductivity (K) from Freeze and Cherry, 1979.

4.3.3 Hydraulic conductivity

Given that hydraulic conductivity calculations use the values of permeability (equation 4), two calculations were required, one with permeability values calculated with $c_o = 1/2$ and another one with $c_o = 1/6$. Average hydraulic conductivity results of non-spring samples for $c_o = 1/2$ and $c_o = 1/6$ were 9.0x10^{-4} m/s and 3.0x10^{-4} m/s, respectively. While average hydraulic conductivity results of the samples of the active spring for $c_o = 1/2$ and $c_o = 1/6$ were 6.8x10^{-3} m/s and 2.3x10^{-3} m/s, respectively. Calculated hydraulic conductivity values are within the range established by Freeze and Cherry (1979; Figure 4.3.4) for sands and gravels.

Average hydraulic conductivity obtained with the KSAT Meter using the falling head method for non-spring samples was 1.4x10^{-4} m/s and with the constant head method was 1.7x10^{-4} m/s. Hydraulic conductivity for the active spring using the falling head method was 1.2x10^{-4} m/s, and 1.1x10^{-4} m/s with the constant head method. Hydraulic conductivity of sample A3 15 cm using the falling head method was 5.3x10^{-4} m/s, and 7.7x10^{-4} m/s with the constant head method. Hydraulic conductivity values obtained with both methods using the KSAT Meter presented less variability compared to results calculated using the hydraulic conductivity equation based on Kozeny's (1927) permeability model (equation 2), this difference can be associated to instrument and user errors.

Freeze and Cherry (1979) acknowledged that porosity can be of great influence on hydraulic conductivity and indicated that for well-sorted sands with higher porosity higher hydraulic conductivities are likely. However, in this study, the non-spring samples presented the higher average porosity (35%) but lower average hydraulic conductivity (3.8×10^{-4} m/s), compared to samples from the active spring that showed lower average porosity (28%) and higher average hydraulic conductivity (2.3×10^{-3} m/s). These results can be associated to the poorly-graded nature of the sediments (Freeze and Cherry, 1979). Additionally, Morin (2005) found a negative correlation between porosity and hydraulic conductivity in unconsolidated sand with gravel sediments. Their results indicate that porosity that can increase with decreasing hydraulic conductivity.

4.3.4 Water flow

Measured spring water flow rates are presented in table 4.3.4. The average water flow rate at the spring was 1805 L/day. Observations by Ramirez-Lagunas et al. (2023) indicated that the number, dimensions, and water discharged from the spring location varied seasonally. Accordingly, groundwater discharge calculations represent a snapshot in time. Groundwater discharge results presented in this study (Table 4.3.4) can present additional limitations such as the influence of the tide cycle changing the discharge rates of the springs at high tide periods (when the springs are fully submerged by seawater). Groundwater recharge and changes to the inland hydraulic head and gradients can also be a controlling factor affecting the volume of water discharging from the springs. For instance, higher recharge would lead to an increase in the gradient towards the coast and thereby contribute to increased discharge at the springs.

Table 4.3.4. Water flow rates obtained at the active spring (location B4; Figure 4.2.1), at low tide on 18 September 2020, at 10 minutes intervals.

Flow rate (L/day)
1182
2589
1171
1261
2817

4.4 Conclusions

The sediment characteristics of the intertidal sand boils within springs located in Sellicks Beach, South Australia were investigated through determination of grain size distributions, porosity, permeability, and hydraulic conductivities of sediments at Sellicks Beach. The influence of these sediment characteristics on sand boils were investigated. The grain size analysis revealed that the sediments at the study site exhibited spatial variability. The non-spring locations showed similar sediment sizes, consisting mainly of fine and medium sands. In contrast, the active sand boils within the spring exhibited more diverse range of sediment sizes, including fine sands, pebbles, and medium sands. The presence of larger clasts at 15 cm depth in location A3 suggested its potential as an inactive sand boil location.

Porosity measurements assessed the void spaces within the sediments at Sellicks Beach. Results indicated an inverse relationship between grain size and porosity, highlighting that larger grain sizes correspond to lower porosity. These findings align with established knowledge and contribute to our understanding of the sediment properties at Sellicks Beach. Permeability results fell within the expected range for sands and gravels. The comprehensive approach of applying both the use of the KSAT Meter and calculations based on permeability provided a more robust evaluation of the groundwater flow characteristics. The hydraulic conductivity measurements obtained using the two KSAT Meter methods (constant and falling head) showed less variability compared to calculations based on the hydraulic conductivity equation with varying constants (Co). This methodological approach ensured a more accurate estimation of the hydraulic conductivity values and their implications for groundwater movement.

It is worth noting that most field-based sand boil studies have been conducted near rivers, dams or polders (e.g., Dismal River and Noordplas Polder), rather than in coastal areas like our case study located in the intertidal zone. Thus, investigating sand boils specifically in intertidal environments fills a significant gap in the knowledge and allows for a more comprehensive understanding of the complex interactions between groundwater dynamics, sediment transport, and coastal erosion.

Future studies focusing on sand boils in intertidal environments could greatly benefit from temporal measurements of sand boil dimensions, water discharge and hydraulic gradients, as they provide valuable insights into the processes controlling coastal sand boil formation. Additionally, comparing field results with theoretical values found in the literature and with laboratory studies, can enhance our understanding of the underlying mechanisms involved in the initiation of sand boils.

Chapter 5

Conclusions

This research project aimed to investigate the intertidal springs in Sellicks Beach, South Australia, and their groundwater-seawater interactions and sediment characteristics. Existing literature on sand boils predominantly focuses on the study of such features along rivers, dams, or in polder settings. By focusing on intertidal springs and their sediment characteristics, the study fills a notable gap in the current knowledge on sand boils in intertidal environments and their impacts on sediment transport and costal erosion.

The research work included the location and description of intertidal springs using non-invasive techniques such as electromagnetic (EM) geophysics and handheld thermal infrared (TIR) imagery, allowing for the identification of their spatial distribution (Chapter 3). Additionally, the study used the stable isotopes of water ($\delta^{18}O$ and $\delta^{2}H$), to assess the seasonal variability and the influence of groundwater-seawater mixing processes and tidal variations. The isotope data was able to identify the sources of water feeding the intertidal springs and showed that discharge from the springs is controlled by a mixture of two main end members, fresh regional groundwater, and seawater. Nevertheless, the findings were not able to accurately determine which aquifer is feeding the intertidal springs. The complexity of the multi-aquifer setting, and structural geology of the site makes it challenging to determine whether the springs are primarily feed from the Port Willunga Formation aquifer, the Quaternary aquifer, a combination of both aquifers, or presenting a contribution from the deeper aquifers.

Chapter 4 describes the methodology that was used to investigate the sediment characteristics of the intertidal sand boils within the springs. It involved estimating the hydraulic conductivity of the sand boil sediments using a KSAT Meter. This approach provided a more accurate estimation of hydraulic conductivity compared to the grain size distribution method. The study identified spatial variations in sediment sizes and their potential impact on the occurrence and behaviour of sand boils within the intertidal springs. The analysis revealed variations in sediment grain sizes across the study area, with non-spring locations consisting mainly of fine and medium sands, while active sand boils within the springs exhibited a wider range of sediment sizes, including fine sands, pebbles, and medium sands. These observations suggest the potential presence of inactive sand boils based on the occurrence of larger clasts at specific depths in certain locations (e.g., location A3).

Several limitations applying to the current research work should be noted. Firstly, the study was limited by the restricted fieldwork opportunities due to the tidal nature of the site. Fieldwork could only be conducted during low tide periods, which significantly limits the available time for data collection. This can affect the comprehensiveness of the study's findings and the ability to capture the full range of hydrological and sedimentological processes occurring within the intertidal springs.

Another significant limitation is the inability to employ invasive techniques, such as ERT geophysics that injects current into the ground, digging or removing large amounts of sand to expose the faults and fractures in the rock system, due to the cultural importance of Sellicks Beach. Beyond cultural considerations, factors such as beach protection measures and the local population's presence further restrict the implementation of invasive methods. As a result, the understanding of the source and structural controls of the intertidal springs may be limited to the available non-invasive methods, such as non-invasive geophysical surveys and imagery.

Furthermore, the popularity of Sellicks Beach and the frequent presence of visitors can introduce potential sources of noise during data collection. The presence of foot traffic and recreational activities on the beach may affect the sediment dynamics and complicate the interpretation of field measurements. Despite the discussed limitations, this study has provided valuable insights into the groundwater-surface water interactions, sediment characteristics, and hydraulic properties of the intertidal springs at Sellicks Beach.

Future research efforts can include a comprehensive characterisation of the fractured rock system (PWF) underneath the beach sand, which would enhance our current understanding of the sources and structural, geological controls of the springs. Future studies can obtain a temporal assessment of the springs to better understand their seasonal variability, including monitoring spring heads and water discharge. This would provide insights into the dynamics and behaviour of the intertidal springs throughout different seasons. Additionally, sediment transport analysis would be greatly beneficial to characterize and understand the release of water and sediment from intertidal sand boils within the springs. This analysis would contribute to a better understanding of the sediment dynamics and the role of intertidal sand boils in the overall sediment transport processes. In addition, comparing field results with theoretical values from the literature and laboratory studies can further improve our understanding of the underlying mechanisms involved in intertidal sand boil processes.

Bibliography

ACWS, 2006. An integrated environmental monitoring program for Adelaide’s Coastal Waters. Canberra.

Adelaide and Mount Lofty Ranges NRM Board, 2007. Water Allocation Plan for the McLaren Vale Prescribed Wells Area. Adelaide.

Aggarwal, P., Fröhlich, K., Kulkarni, K.M., 2009. Environmental Isotopes In Groundwater Studies, in: Silveira, L., Usunoff, E.J. (Eds.), Groundwater. EOLSS Publications, pp. 69–92.

Ahlinhan, M.F., Achmus, M., 2010. Experimental Investigation of Critical Hydraulic Gradients for Unstable Soils. Scour Eros., Proceedings. https://doi.org/doi:10.1061/41147(392)58

Aielli, S., Pavan, S., Parodi, S., Rosso, A., Tanda, M.G., Marchi, M., Vezzoli, G., Pantano, A., Losa, D., Sirtori, M., 2019. Collection and Analysis of the Reactivation Data of the Historical Sand Boils in the Po River Levees BT - Internal Erosion in Earthdams, Dikes and Levees, in: Bonelli, S., Jommi, C., Sterpi, D. (Eds.), . Springer International Publishing, Cham, pp. 327–335.

Atapour, H., Mortazavi, A., 2018. The influence of mean grain size on unconfined compressive strength of weakly consolidated reservoir sandstones. J. Pet. Sci. Eng. 171, 63–70. https://doi.org/https://doi.org/10.1016/j.petrol.2018.07.029

Auken, E., Christiansen, A.V., Kirkegaard, C., Fiandaca, G., Schamper, C., Behroozmand, A.A., Binley, A., Nielsen, E., Effersø, F., Christensen, N.B., Sørensen, K., Foged, N., Vignoli, G.,

2015. An Overview Of A Highly Versatile Forward And Stable Inverse Algorithm For Airborne, Ground-Based And Borehole Electromagnetic And Electric Data. Explor. Geophys. 46, 223–235. https://doi.org/10.1071/EG13097

Aydin, A., 1978. Small Faults Formed As Deformation Bands In Sandstone, in: Byerlee, J.D., Wyss, M. (Eds.), Rock Friction And Earthquake Prediction. Birkhäuser Basel, pp. 913–930. https://doi.org/10.1007/978-3-0348-7182-2_22

Bardsley, D.K., Palazzo, E., Wiseman, N.D., Stringer, R., 2017. The roles of agricultural biodiversity in the McLaren Vale landscape. Department of Environment, Water and Natural Resources (SA). https://doi.org/https://doi.org/APO-103711

Beck, A.J., Tsukamoto, Y., Tovar-Sanchez, A., Huerta-Diaz, M., Bokuniewicz, H.J., Sañudo-Wilhelmy, S.A., 2007. Importance Of Geochemical Transformations In Determining Submarine Groundwater Discharge-Derived Trace Metal And Nutrient Fluxes. Appl. Geochemistry 22, 477–490. https://doi.org/ 10.1016/j.apgeochem.2006.10.005

Benkendorff, K., Fairweather, P., Dittmann, S., 2008. Intertidal Ecosystems, in: Shepherd, S., Bryars, S., Kirkegaard, I., Harbison, P., Jennings, J.T. (Eds.), Natural History Of The Gulf St Vincent. Royal Society Of S.A., Adelaide, Australia.

Bokuniewicz, H., Taniguchi, M., Ishitoibi, T., Charette, M., Allen, M., Kontar, E.A., 2008. Direct Measurements Of Submarine Groundwater Discharge (SGD) Over A Fractured Rock Aquifer In Flamengo Bay Brazil. Estuar. Coast. Shelf Sci. 76, 466–472. https://doi.org/10.1016/j.ecss.2007.07.047

Bonelli, S., Nicot, F., 2013. Erosion in Geomechanics Applied to Dams and Levees. Wiley. https://doi.org/10.1002/9781118577165

Bourman, R.P., Murray-Wallace, C. V, Harvey, N., 2016. Coastal Landscapes of South Australia. University of Adelaide Press. https://doi.org/https://doi.org/10.20851/coast-sa

Bureau of Meteorology, 2017. South Australian Observations. http://www.bom.gov.au/climate/current/annual/sa/archive/2017 (accessed 14.07.22).

Bureau of Meteorology, 2019. South Australian Observations. http://www.bom.gov.au/climate/current/annual/sa/archive/2019 (accessed 14.07.22).

Bureau of Meteorology, 2020. South Australian Observations. http://www.bom.gov.au/sa/observations (accessed 21.09.20).

Burnett, W.C., Aggarwal, P.K., Aureli, A., Bokuniewicz, H., Cable, J.E., Charette, M.A., Kontar, E., Krupa, S., Kulkarni, K.M., Loveless, A., Moore, W.S., Oberdorfer, J.A., Oliveira, J., Ozyurt, N., Povinec, P., Privitera, A.M.G., Rajar, R., Ramessur, R.T., Scholten, J., Stieglitz, T., Taniguchi, M., Turner, J. V, 2006. Quantifying Submarine Groundwater Discharge In The Coastal Zone Via Multiple Methods. Sci. Total Environ. 367, 498–543. https://doi.org/10.1016/j.scitotenv.2006.05.009

Burnett, W.C., Bokuniewicz, H., Huettel, M., Moore, W.S., Taniguchi, M., 2003. Groundwater And Pore Water Inputs To The Coastal Zone. Biogeochemistry 66, 3–33. https://doi.org/10.1023/b:Biog.0000006066.21240.53

Burnett, W.C., Dulaiova, H., 2006. Radon As A Tracer Of Submarine Groundwater Discharge Into A Boat Basin In Donnalucata, Sicily. Cont. Shelf Res. 26, 862–873. https://doi.org/10.1016/j.csr.2005.12.003

Cable, J.E., Burnett, W.C., Chanton, J.P., Weatherly, G.L., 1996. Estimating Groundwater Discharge Into The Northeastern Gulf Of Mexico Using Radon-222. Earth Planet. Sci. Lett. 144, 591–604. https://doi.org/10.1016/S0012-821X(96)00173-2

Cann, J.H., Lower, C.S., Jago, J.B., 2014. Provenance And Sediment Characteristics Of Contemporary Gravel Deposits At Sellicks Beach, Eastern Shore Of Gulf St Vincent, South Australia. Aust. J. Earth Sci. 61, 819–836. https://doi.org/10.1080/08120099.2014.941400

Carey, H., Lenkopane, M.K., Werner, A.D., Li, L., Lockington, D.A., 2009. Tidal controls on coastal groundwater conditions: field investigation of a macrotidal system. Aust. J. Earth Sci. 56, 1165–1179. https://doi.org/10.1080/08120090903246246

Carman, P.C., 1937. Fluid flow through granular beds. Transactions, Institution of Chemical Engineers (London) 15, 150–166.

Cave, R.R., Henry, T., 2011. Intertidal And Submarine Groundwater Discharge On The West Coast Of Ireland. Estuar. Coast. Shelf Sci. 92, 415–423. https://doi.org/10.1016/j.ecss.2011.01.019

Charette, M.A., Buesseler, K.O., Andrews, J.E., 2001. Utility Of Radium Isotopes For Evaluating The Input And Transport Of Groundwater-Derived Nitrogen To A Cape Cod Estuary. Limnol. Oceanogr. 46, 465–470. https://doi.org/10.4319/lo.2001.46.2.0465

Charette, M.A., Sholkovitz, E.R., 2006. Trace Element Cycling In A Subterranean Estuary: Part 2. Geochemistry Of The Pore Water. Geochim. Cosmochim. Acta 70, 811–826. https://doi.org/10.1016/j.gca.2005.10.019

Christiansen, A.V., Pedersen, J.B., Auken, E., Søe, N.E., Holst, M.K., Kristiansen, S.M., 2016. Improved Geoarchaeological Mapping With Electromagnetic Induction Instruments From

Dedicated Processing And Inversion. Remote Sens. 8, 1022. https://doi.org/10.3390/rs8121022

Craig, H., 1961. Isotopic Variations in Meteoric Waters. Science (80-.). 133, 1702–1703. https://doi.org/10.1126/science.133.3465.1702

Coastal Management Branch 1984, Adelaide Coast Protection Strategy Review, Department of Environment and Planning report to the Coast Protection Board, Adelaide.

Dale, R.K., Miller, D.C., 2007. Spatial And Temporal Patterns Of Salinity And Temperature At An Intertidal Groundwater Seep. Estuar. Coast. Shelf Sci. 72, 283–298. https://doi.org/10.1016/j.ecss.2006.10.024

Dalrymple, R.W., Choi, K., 1978. Sediment transport by tides BT - Sedimentology. Springer Berlin Heidelberg, Berlin, Heidelberg, pp. 993–998. https://doi.org/10.1007/3-540-31079-7_181

Danielescu, S., MacQuarrie, K.T.B., Faux, R.N., 2009. The integration of thermal infrared imaging, discharge measurements and numerical simulation to quantify the relative contributions of freshwater inflows to small estuaries in Atlantic Canada. Hydrol. Process. 23, 2847–2859. https://doi.org/10.1002/hyp.7383

de Louw, P.G.B., Oude Essink, G.H.P., Stuyfzand, P.J., van der Zee, S.E.A.T.M., 2010. Upward Groundwater Flow In Boils As The Dominant Mechanism Of Salinization In Deep Polders, The Netherlands. J. Hydrol. 394, 494–506. https://doi.org/ 10.1016/j.jhydrol.2010.10.009

de Louw, P.G.B., Vandenbohede, A., Werner, A.D., Oude Essink, G.H.P., 2013. Natural saltwater upconing by preferential groundwater discharge through boils. J. Hydrol. 490, 74–87. https://doi.org/https://doi.org/10.1016/j.jhydrol.2013.03.025

Department for Environment and Heritage, 2005. Adelaide's Living Beaches A Strategy for 2005–2025

DEW, 2021. McLaren Vale Prescribed Wells Area 2019–20 water resources assessment. DEW Technical Note 2021/12. Government of South Australia, Department for Environment and Water.

Duarte, T.K., Hemond, H.F., Frankel, D., Frankel, S., 2006. Assessment Of Submarine Groundwater Discharge By Handheld Aerial Infrared Imagery: Case Study Of Kaloko Fishpond And Bay, Hawai'i. Limnol. Oceanogr. Methods 4, 227–236. https://doi.org/10.4319/lom.2006.4.227

Dyson, I.A., 1998. Estuarine Facies Of The North Maslin Sand And South Maslin Sand, Maslin Beach. MESA J. 11, 42–46.

Eamus, D., Hatton, T., Cook, P., Colvin, C., 2006. Ecohydrology: Vegetation Function, Water and Resource Management. CSIRO Publishing, Melbourne.

El Hage, M., Robinson, C.A., El-Baz, F., Shaban, A., 2020. Fracture-Controlled Groundwater Seeps Into The Mediterranean Sea Along The Coast Of Lebanon. Arab. J. Geosci. 13, 520. https://doi.org/10.1007/s12517-020-05565-7

Fairburn, B., 1998. The Willunga Embayment — An Stratigraphic Revision. MESA J. 11, 35–41.

Fanjul, E., Grela, M.A., Canepuccia, A., Iribarne, O., 2008. The Southwest Atlantic intertidal burrowing crab Neohelice granulata modifies nutrient loads of phreatic waters entering coastal area. Estuar. Coast. Shelf Sci. 79, 300–306. https://doi.org/https://doi.org/10.1016/j.ecss.2008.04.005

FitzGerald, D.M., 1996. Geomorphic Variability and Morphologic and Sedimentologic Controls on Tidal Inlets. J. Coast. Res. 47–71.

Freeze, R.A., Cherry, J.A., 1979. Groundwater, 0-13-365312-9. Prentice-Hall.

Glynn, E., Quinn, M., Kuszmaul, J., Wilson, J., 2012. Predicting Piping Potential Along Middle Mississippi River Levees, in: 6th International Conference on Scour and Erosion.

Griffiths, J.C., 1951. Size versus Sorting in Some Caribbean Sediments. J. Geol. 59, 211–243. https://doi.org/10.1086/625853

Greenwood, B., 1978. Sediment transport by waves BT - Sedimentology. Springer Berlin Heidelberg, Berlin, Heidelberg, pp. 1016–1028. https://doi.org/10.1007/3-540-31079-7_183

Folk, R.L., 1962. Petrography and origin of the Silurian Rochester and McKenzie Shales, Morgan County, West Virginia. J. Sediment. Res. 32, 539–578. https://doi.org/10.1306/74D70D17-2B21-11D7-8648000102C1865D

Folk, R.L., Ward, W.C., 1957. Brazos River bar [Texas]; a study in the significance of grain size parameters. J. Sediment. Res. 27, 3–26. https://doi.org/10.1306/74D70646-2B21-11D7-8648000102C1865D.

Guhman, A.I., Pederson, D.T., 1992. Boiling sand springs, Dismal River, Nebraska: Agents for formation of vertical cylindrical structures and geomorphic change. Geology 20, 8–10. https://doi.org/10.1130/0091-7613(1992)020<0008:BSSDRN>2.3.CO;2

Harrington, N., Cook, P.G., 2012. Willunga Research Update, October 2012. Adelaide.

Heiss, J.W., Michael, H.A., 2014. Saltwater-freshwater mixing dynamics in a sandy beach aquifer over tidal, spring-neap, and seasonal cycles. Water Resour. Res. 50, 6747–6766. https://doi.org/10.1002/2014WR015574

Inman, D.L., 1949. Sorting of Sediments in the Light of Fluid Mechanics. J. Sediment. Res. 19, 51–70.

Jayawardena, C.L., 2013. Characteristics Of Neotectonic Faulting In The Mount Lofty And Flinders Ranges, South Australia. Sch. Earth Environ. Sci. University of Wollongong, Wollongong, New South Wales. https://doi.org/ro.uow.edu.au/theses/4093/

Johannes, R.E., 1980. The Ecological Significance Of The Submarine Discharge Of Groundwater. Mar. Ecol. Prog. Ser. 3, 365–373. https://doi.org/10.3354/meps003365

Klein, A.H. da F., Silva, G.M. da, Ferreira, Ó., Dias, J.A., 2005. Beach Sediment Distribution for a Headland Bay Coast. J. Coast. Res. 285–293.

Knowles, I., Teubner, M., Yan, A., Rasser, P., Lee, J.W., 2007. Inverse groundwater modelling in the Willunga Basin, South Australia. Hydrogeol. J. 15, 1107–1118. https://doi.org/10.1007/s10040-007-0189-6

Kolb, C.R., 1975. Geologic Control of Sand Boils Along Mississippi River Levees, in: Geomorphology and Engineering.

Komar, P.D., 1998. Beach Processes and Sedimentation, 2nd ed.

Kozeny, J., 1927. Ueber kapillare Leitung des Wassers im Boden. Sitzungsber Akad,Wiss., Wien 136 (2a), 271–306.

Lamontagne, S., La Salle, C.L.G., Hancock, G.J., Webster, I.T., Simmons, C.T., Love, A.J., James-Smith, J., Smith, A.J., Kämpf, J., Fallowfield, H.J., 2008. Radium And Radon Radioisotopes In Regional Groundwater, Intertidal Groundwater, And Seawater In The Adelaide Coastal Waters Study Area: Implications For The Evaluation Of Submarine Groundwater Discharge. Mar. Chem. 109, 318–336. https://doi.org/10.1016/j.marchem.2007.08.010

Lanyon, J.A., Eliot, I.G., Clarke, D.J., 1982. Groundwater-level variation during semidiurnal spring tidal cycles on a sandy beach. Mar. Freshw. Res. 33, 377–400. https://doi.org/https://doi.org/10.1071/MF9820377

Lee, Y.W., Hwang, D.W., Kim, G., Lee, W.C., Oh, H.T., 2009. Nutrient Inputs From Submarine Groundwater Discharge (SGD) In Masan Bay, An Embayment Surrounded By Heavily Industrialized Cities, Korea. Sci. Total Environ. 407, 3181–3188. https://doi.org/10.1016/j.scitotenv.2008.04.013

Levi, E., Goldman, M., Hadad, A., Gvirtzman, H., 2008. Spatial Delineation Of Groundwater Salinity Using Deep Time Domain Electromagnetic Geophysical Measurements: A Feasibility Study. Water Resour. Res. 44. https://doi.org//10.1029/2007WR006459

Li, L., Barry, D.A., 2000. Wave-Induced Beach Groundwater Flow. Adv. Water Resour. 23, 325–337. https://doi.org/10.1016/S0309-1708(99)00032-9

Li, L., Horn, D.P., Baird, A.J., 2006. Tide-Induced Variations in Surface Temperature and Water-Table Depth in the Intertidal Zone of a Sandy Beach. J. Coast. Res. 22, 1370–1381.

Liu, Y., Jiao, J., Cheng, H., 2018. Tracing Submarine Groundwater Discharge Flux In Tolo Harbor, Hong Kong (China). Hydrogeol. J. 26, 1857–1873. https://doi.org/10.1007/s10040-018-1736-z

Lubiniecki, D.C., White, S.R.S., King, R.C., Holford, S.P., Bunch, M.A., Hill, S.M., 2019. Structural Evolution Of Carbonate-Hosted Cataclastic Bands Adjacent To A Major Neotectonic Fault, Sellicks Beach, South Australia. J. Struct. Geol. 126, 11–24. https://doi.org/10.1016/j.jsg.2019.05.004

Malone, G.D.F., 2012. Phases of Aboriginal Inclusion in the Public Space in Adelaide, South Australia since Colonisation. Sch. Environ. Flinders University, Adelaide, South Australia .

Masch, F. D., & Denny, K. J., 1966. Grain size distribution and its effect on the permeability of unconsolidated sands. Water Resources Research, 2(4), 665–677.

Michela, M., García, M.M.F., Guido, G., Laura, T., 2021. Field measurements on a large natural sand boil along the river Po, Italy. Q. J. Eng. Geol. Hydrogeol. 54, qjegh2020-097. https://doi.org/10.1144/qjegh2020-097

Martin, R.R., 1998. Willunga Basin – Status Of Groundwater Resources 1998. Primary Industries And Resources South Australia Report Book 98/28, Adelaide.

Martin, R. R., 2006. Hydrogeology and Numercial Groundwater Flow Model for the McLaren Vale Prescribed Wells Area Summary Report, Adelaide and Mount Lofty Ranges Natural Resource Management Board.

May, R.I., Bourman, R.P., 1984. Coastal Landslumping In Pleistocene Sediments At Sellicks Beach, South Australia. Trans. R. Soc. South Aust.

McAllister, S.M., Barnett, J.M., Heiss, J.W., Findlay, A.J., MacDonald, D.J., Dow, C.L., Luther III, G.W., Michael, H.A., Chan, C.S., 2015. Dynamic Hydrologic And Biogeochemical

Processes Drive Microbially Enhanced Iron And Sulfur Cycling Within The Intertidal Mixing Zone Of A Beach Aquifer. Limnol. Oceanogr. 60, 329–345. https://doi.org/10.1002/lno.10029

McCormack, T., Gill, L.W., Naughton, O., Johnston, P.M., 2014. Quantification of submarine/intertidal groundwater discharge and nutrient loading from a lowland karst catchment. J. Hydrol. 519, 2318–2330. https://doi.org/10.1016/j.jhydrol.2014.09.086

McLean, R.F., Kirk, R.M., 1969. Relationships between grain size, size-sorting, and foreshore slope on mixed sand - shingle beaches. New Zeal. J. Geol. Geophys. 12, 138–155. https://doi.org/10.1080/00288306.1969.10420231

McNeill, J.D., 1980. Electromagnetic Terrain Conductivity Measurement At Low Induction Numbers Tech. Note TN-6. Geonics Limited. Ontario, Canada.

Miller, D.C., Ullman, W.J., 2004. Ecological Consequences Of Ground Water Discharge To Delaware Bay, United States. Groundwater 42, 959–970. https://doi.org/10.1111/j.1745-6584.2004.tb02635.x

Moore, W.S., 1999. The Subterranean Estuary: A Reaction Zone Of Ground Water And Sea Water. Mar. Chem. 65, 111–125. https://doi.org/10.1016/S0304-4203(99)00014-6

Moore, W.S., 2010. The Effect Of Submarine Groundwater Discharge On The Ocean. Ann. Rev. Mar. Sci. 2, 59–88. https://doi.org/10.1146/annurev-marine-120308-081019

Moosdorf, N., Oehler, T., 2017. Societal use of fresh submarine groundwater discharge: An overlooked water resource. Earth-Science Rev. 171, 338–348. https://doi.org/10.1016/j.earscirev.2017.06.006

Morales, J.A., 2022. Tide-Dominated Systems II: Tidal Flats and Wetlands BT - Coastal Geology, in: Morales, J.A. (Ed.), . Springer Nature Switzerland, Cham, pp. 289–307. https://doi.org/10.1007/978-3-030-96121-3_20

Morin, Roger H., 2005. Negative correlation between porosity and hydraulic conductivity in sand-and-gravel aquifers at Cape Cod, Massachusetts, USA. USGS Staff .

Mulligan, A.E., Charette, M.A., 2006. Intercomparison Of Submarine Groundwater Discharge Estimates From A Sandy Unconfined Aquifer. J. Hydrol. 327, 411–425. https://doi.org/10.1016/j.jhydrol.2005.11.056

NCRIS Groundwater Database, 2022. http://groundwater.anu.edu.au/fieldsite/willunga (accessed 22.07.22).

Nugroho, S.H., Putra, P.S., 2018. Spatial distribution of grain size and depositional process in tidal area along Waikelo Beach, Sumba. Mar. Georesources Geotechnol. 36, 299–307. https://doi.org/10.1080/1064119X.2017.1312649

O’Driscoll, M., Dewalle, D., Humphrey, C., Iverson, G., 2019. Groundwater Seeps: Portholes to Evaluate Groundwater’s Influence on Stream Water Quality. J. Contemp. Water Res. Educ. 166, 57–78. https://doi.org/10.1111/j.1936-704X.2019.03302.x

Ogolo, N., Akinboro, O., Inam, J., Akpokere, F., Onyekonwu, M.O., 2015. Effect of Grain Size on Porosity Revisited. https://doi.org/10.2118/178296-MS

Paepen, M., Hanssens, D., De Smedt, P., Walraevens, K., Hermans, T., 2020. Combining Resistivity And Frequency Domain Electromagnetic Methods To Investigate Submarine Groundwater Discharge In The Littoral Zone. Hydrol. earth Syst. Sci. 24, 3539–3555. https://doi.org/10.5194/hess-24-3539-2020

Post, V.E.A., Banks, E., Brunke, M., 2018. Groundwater flow in the transition zone between freshwater and saltwater: a field-based study and analysis of measurement errors. Hydrogeol. J. 26, 1821–1838. https://doi.org/10.1007/s10040-018-1725-2

Post, V.E.A., Salmon, U., van Duivenvoorde, W., 2020. The Intertidal Springs Near The Vergulde Draak 1656 Wreck Site, Western Australia: Hydrogeological Characteristics And Archaeological Significance. Hydrogeol. J. 28, 2071–2084. https://doi.org/10.1007/s10040-020-02173-3

Povinec, P.P., Aggarwal, P.K., Aureli, A., Burnett, W.C., Kontar, E.A., Kulkarni, K.M., Moore, W.S., Rajar, R., Taniguchi, M., Comanducci, J.F., Cusimano, G., Dulaiova, H., Gatto, L., Groening, M., Hauser, S., Levy-Palomo, I., Oregioni, B., Ozorovich, Y.R., Privitera, A.M.G., Schiavo, M.A., 2006. Characterisation Of Submarine Groundwater Discharge Offshore South-Eastern Sicily. J. Environ. Radioact. 89, 81–101. https://doi.org/10.1016/j.jenvrad.2006.03.008

Preiss, W. V, 2019. The tectonic history of Adelaide's scarp-forming faults. Aust. J. Earth Sci. 66, 305–365. https://doi.org/10.1080/08120099.2018.1546228

Ramirez-Lagunas, M., Banks, E.W., Werner, A.D., Wallis, I., Shanafield, M., 2023. Characterisation of intertidal springs in a faulted multi-aquifer setting. J. Hydrol. 616, 128457. https://doi.org/https://doi.org/10.1016/j.jhydrol.2022.128457

Reed, G.D., Energy, D. of M. and, 1982. Geophysical Investigation Of The Willunga Fault Zone. Department Of Mines And Energy, Adelaide, South Australia.

Reid, J.E., Howlett, A., 2001. Application of the EM-31 Terrain Conductivity Meter in Highly-Conductive Regimes. Explor. Geophys. 32, 219–224. https://doi.org/10.1071/EG01219

Robbins, B.A., Stephens, I.J., Van Beek, V.M., Koelewijn, A.R., Bezuijen, A., 2019. Field measurements of sand boil hydraulics. Géotechnique 70, 153–160. https://doi.org/10.1680/jgeot.18.P.151

Robinson, C., Li, L., Prommer, H., 2007. Tide-Induced Recirculation Across The Aquifer-Ocean Interface. Water Resour. Res. 43. https://doi.org/10.1029/2006wr005679

Rodellas, V., Garcia-Orellana, J., Tovar-Sánchez, A., Basterretxea, G., López-Garcia, J.M., Sánchez-Quiles, D., Garcia-Solsona, E., Masqué, P., 2014. Submarine Groundwater Discharge As A Source Of Nutrients And Trace Metals In A Mediterranean Bay (Palma Beach, Balearic Islands). Mar. Chem. 160, 56–66. https://doi.org/10.1016/j.marchem.2014.01.007

Röper, T., Greskowiak, J., Massmann, G., 2014. Detecting Small Groundwater Discharge Springs Using Handheld Thermal Infrared Imagery. Ground Water 52, 936–942. https://doi.org/10.1111/gwat.12145

Rotnicka, J., 2011. Impact of Beach Surface Type on the Rate of Sand Transport by Wind. J. Coast. Res. 2058–2062.

Salama, R.B., 1996. Physical and Chemical Techniques for Discharge Studies - Part 1. CSIRO Publishing, Australia. https://doi.org/10.1071/9780643105331

Schmertmann, J.H., 2000. The No-Filter Factor of Safety against Piping through Sands. Judgm. Innov., Proceedings. https://doi.org/doi:10.1061/9780784405376.006

Schneider, J.C., Kruse, S.E., 2003. A Comparison Of Controls On Freshwater Lens Morphology Of Small Carbonate And Siliciclastic Islands: Examples From Barrier Islands In Florida, USA. J. Hydrol. 284, 253–269. https://doi.org/10.1016/j.jhydrol.2003.08.002

Shanafield, M., Gutiérrrez-Jurado, K., White, N., Hatch, M., Keane, R., 2020. Catchment-Scale Characterization Of Intermittent Stream Infiltration; A Geophysics Approach. J. Geophys. Res. Earth Surf. 125, e2019JF005330. https://doi.org/10.1029/2019jf005330

Sherman, D.J., 2019. Dissipative Beaches BT - Encyclopedia of Coastal Science, in: Finkl, C.W., Makowski, C. (Eds.), Springer International Publishing, Cham, pp. 724–725. https://doi.org/10.1007/978-3-319-93806-6_123

Short, A.D., 2010. Sediment Transport around Australia—Sources, Mechanisms, Rates, and Barrier Forms. J. Coast. Res. 26, 395–402.

Short, M.A., Lamontagne, S., Cook, P.G., Cranswick, R., 2014. Characterising The Distribution Of Near-Shore Submarine Groundwater Discharge Along A Coastline Using 222Rn And

Electrical Conductivity. Aust. J. Earth Sci. 61, 319–331. https://doi.org/10.1080/08120099.2014.884018

Smith, N.P., 1986. The Rise And Fall Of The Estuarine Intertidal Zone. Estuaries 9, 95–101. https://doi.org/10.2307/1351941

Sterpi, D., 2003. Effects of the Erosion and Transport of Fine Particles due to Seepage Flow. Int. J. Geomech. 3, 111–122. https://doi.org/10.1061/(ASCE)1532-3641(2003)3:1(111)

Stevens, L., Meretsky, V., 2008. Springs Ecosystem Ecology and Conservation, in: Stevens, L., Meretsky, V. (Eds.), Aridland Springs in North America: Ecology and Conservation. University of Arizona Press, Tucson, Arizona, pp. 3–10.

Stieglitz, T., 2005. Submarine Groundwater Discharge Into The Near-Shore Zone Of The Great Barrier Reef, Australia. Mar. Pollut. Bull. 51, 51–59. https://doi.org/10.1016/j.marpolbul.2004.10.055

Swarzenski, P.W., Izbicki, J.A., 2009. Coastal Groundwater Dynamics Off Santa Barbara, California: Combining Geochemical Tracers, Electromagnetic Seepmeters, And Electrical Resistivity. Estuar. Coast. Shelf Sci. 83, 77–89. https://doi.org/10.1016/j.ecss.2009.03.027

Taboroši, D., Jenson, J.W., Mylroie, J.E., 2013. Field Observations Of Coastal Discharge From An Uplifted Carbonate Island Aquifer, Northern Guam, Mariana Islands: A Descriptive Geomorphic And Hydrogeologic Perspective. J. Coast. Res. 29, 926. https://doi.org/10.2112/JCOASTRES-D-12-00054.1

Tait, D.R., Santos, I.R., Erler, D. V, Befus, K.M., Cardenas, M.B., Eyre, B.D., 2013. Estimating Submarine Groundwater Discharge In A South Pacific Coral Reef Lagoon Using Different

Radioisotope And Geophysical Approaches. Mar. Chem. 156, 49–60. https://doi.org/10.1016/j.marchem.2013.03.004

Taniguchi, M., Burnett, W.C., Cable, J.E., Turner, J. V, 2002. Investigation Of Submarine Groundwater Discharge. Hydrol. Process. 16, 2115–2129. https://doi.org/10.1002/hyp.1145

Taniguchi, M., Dulai, H., Burnett, K.M., Santos, I.R., Sugimoto, R., Stieglitz, T., Kim, G., Moosdorf, N., Burnett, W.C., 2019. Submarine Groundwater Discharge: Updates On Its Measurement Techniques, Geophysical Drivers, Magnitudes, And Effects. Front. Environ. Sci. 7. https://doi.org/10.3389/fenvs.2019.00141

Terwey, J.L., 1984. Isotopes In Groundwater Hydrology, In: Proceedings Of The Harare Symposium: Challenges In African Hydrology And Water Resources. IAHS, Netherlands, pp. 155–160.

Terzaghi, K., 1922. Der grundbruch an stauwerken und seine verhutung. Wasserkraft 17, 445–449.

Tokarev, V., 2005. Neotectonics Of The Mount Lofty Ranges (South Australia). Sch. Earth Environ. Sci. University of Adelaide, Adelaide, South Australia.

Townsend, F.C.D., Bloomquist, D., Shiau, J.M.,Martinez, R., Rubin, H., 1988. Analytical and Experimental Investigation of Piping and Filter Design for Sands, Report to the Bureau of Reclamation. Department of Civil Engineering, University of Florida, Gainesville, Florida.

Turner, I., 1993. Water table outcropping on macro-tidal beaches: A simulation model. Mar. Geol. 115, 227–238. https://doi.org/https://doi.org/10.1016/0025-3227(93)90052-W

Tsai, C.-C., Lin, W.-C., Chu, M.-C., Chi, C.-C., 2022. Experimental study on the mechanism of sand boils and associated settlements due to soil liquefaction in loose sand. Eng. Geol. 306, 106708. https://doi.org/https://doi.org/10.1016/j.enggeo.2022.106708

U.S. Army Corps of Engineers (USACE), 1941. Investigation of underseepage: Lower Mississippi River levees. Vicksburg, MS.

Van Beek, V., Bezuijen, A., Sellmeijer, H., 2013. Backward Erosion Piping. Eros. Geomech. Appl. to Dams Levees, Wiley Online Books. https://doi.org/https://doi.org/10.1002/9781118577165.ch3

Wan, C.F., Fell, R., 2004. Experimental investigation of internal erosion by the process of suffusion in embankment dams and their foundations. ANCOLD Bull. 69–78.

Waska, H., Kim, G., 2011. Submarine Groundwater Discharge (SGD) As A Main Nutrient Source For Benthic And Water-Column Primary Production In A Large Intertidal Environment Of The Yellow Sea. J. Sea Res. 65, 103–113. https://doi.org/10.1016/j.seares.2010.08.001

Werner, A.D., Jazayeri, A., Ramirez-Lagunas, M., 2020. Sediment Mobilisation And Release Through Groundwater Discharge To The Land Surface: Review And Theoretical Development. Sci. Total Environ. 714, 136757. https://doi.org/10.1016/j.scitotenv.2020.136757

Williams, J.G., 1974. Sand Boils: A Modern Analogue of Ancient Sand Volcanoes. J. Ark. Acad. Sci. 28, 80–81.

Williams, D., 2016. Invertebrates in groundwater springs and seeps, in: Batzer, D., Boix, D. (Eds.), Invertebrates in Freshwater Wetlands. Springer International Publishing, Switzerland, pp. 357–409. https://doi.org/10.1007/978-3-319-24978-0_11

Wilson, W., Moore, J., 1998. Glossary of Hydrology. American Geological Institute, Alexandria, Virginia.

Wolff, T.F., 2002. Performance of Levee Underseepage Controls: A Critical Review.

Wright, L.D., Chappell, J., Thom, B.G., Bradshaw, M.P., Cowell, P., 1979. Morphodynamics of reflective and dissipative beach and inshore systems: Southeastern Australia. Mar. Geol. 32, 105–140.

Xin, P., Robinson, C., Li, L., Barry, D.A., Bakhtyar, R., 2010. Effects Of Wave Forcing On A Subterranean Estuary. Water Resour. Res. 46. https://doi.org/10.1029/2010wr009632

Yang, K.H., Wang, J.Y., 2017. Experiment and statistical assessment on piping failures in soils with different gradations. Mar. Georesources Geotechnol. 35, 512–527. https://doi.org/10.1080/1064119X.2016.1213338

Yechieli, Y., Kafri, U., Goldman, M., Voss, C., 2001. Factors Controlling The Configuration Of The Fresh–Saline Water Interface In The Dead Sea Coastal Aquifers: Synthesis Of TDEM Surveys And Numerical Groundwater Modeling. Hydrogeol. J. 9, 367–377. https://doi.org/10.1007/s100400100146

Appendix 1

First author publication

Journal of Hydrology 616 (2023) 128457

Contents lists available at ScienceDirect

Journal of Hydrology

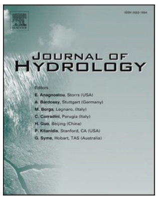

Research papers

Characterisation of intertidal springs in a faulted multi-aquifer setting

M. Ramirez-Lagunas [a,b,*], E.W. Banks [a,b], A.D. Werner [a,b], I. Wallis [a,b], M. Shanafield [a,b]

[a] College of Science and Engineering, Flinders University, GPO Box 2100, Adelaide, SA 5001, Australia
[b] National Centre for Groundwater Research and Training, Flinders University, GPO Box 2100, Adelaide, SA 5001, Australia

ARTICLE INFO

Keywords:

Springs

Geophysics

Temperature

Stable isotopes

Intertidal zone

ABSTRACT

In intertidal zones, groundwater is often present as seepage that provides freshwater and nutrients to marine ecosystems. Point discharge or springs in intertidal zones have been observed in many locations, often in the form of sand boils. The spatial extent, temporal variability and source of intertidal springs are rarely documented and typically, not well understood. This study examined four intertidal groundwater springs at Sellicks Beach, South Australia, during May 2017, November 2019 and September 2020 using a combination of hydro- geophysical methods. A thermal infrared survey undertaken in 2017 showed springs as groupings of closely spaced sand boils that were warmer (15 ◦C) than the surrounding saturated beach sediments (7 ◦C). The four springs ranged in diameter from 0.20 to 0.45 m. Electromagnetic geophysical surveys identified a resistive anomaly (3.5 to 5.0 ohm.m), assumed to represent freshwater upwelling at the location of a spring, that extended 10 m horizontally and at least 6.7 m vertically. The average electrical conductivity of water discharging from the springs was 18.4 mS/cm, while seawater was 54.8 mS/cm. δ18O and δ2H data from the springs showed a variation between winter and spring, likely caused by variations in mixing ratios between seawater and groundwater. The springs are proximal to major regional fault systems that likely create preferential flow paths that control spring location and flow rates. The observations of spring characteristics highlight the critical role of seawater-groundwater mixing ratios, preferential flow paths and tidal variations in creating temporal variability in spring discharge and salinity.

Introduction

The intertidal zone is a vital link between terrestrial and marine environments (Benkendorff et al., 2008) that is influenced by sea-level fluctuations, groundwater discharge, meteorological forces and sediment transport (Smith, 1986). Intertidal discharge of groundwater is an important phenomenon that shapes ecological and sedimentological processes within intertidal zones and the near-shore environment (Miller and Ullman, 2004; McAllister et al., 2015). For example, groundwater is generally nutrient enriched compared to seawater, and in many places, groundwater discharge provides the primary source (e. g., rather than surface water discharge) of nutrients (Charette et al., 2001; Lee et al., 2009; Cave and Henry, 2011; Liu et al., 2018), and trace elements (Charette and Sholkovitz, 2006; Beck et al., 2007; Rodellas et al., 2014) to marine water bodies. Furthermore, groundwater discharge is known to modify the geomorphology of beaches, whereby high rates of groundwater discharge tend to destabilise intertidal sediments (Bokuniewicz et al., 2008; Post et al., 2020).

The composition of groundwater discharge within intertidal zones is typically a combination of recycled seawater that entered the subsurface during high tide, and (usually) fresher groundwater resulting from net recharge to aquifers in inland regions (Moore, 1999; Li and Barry, 2000; Robinson et al., 2007; Xin et al., 2010). The main processes that control groundwater discharge within intertidal zones include: the subsurface hydraulic properties, the regional aquifer hydraulic gradient, water density variations between the discharging groundwater and seawater, and ocean tides and waves (Taniguchi et al., 2002; Burnett et al., 2003). While intertidal groundwater discharge in the form of diffuse seepage is widespread, under certain circumstances, localised discrete-discharge features may appear (Dale and Miller, 2007; Ro¨per et al., 2014). The former leads to often extensive seepage faces, whereby saturated surface conditions are maintained over large areas, allowing benthic aquatic organisms to survive within intertidal zones during low tides (Waska and Kim, 2011). The latter has been previously described as seeps, springs, boils, and sand boils (Johannes, 1980; Stieglitz, 2005; De Louw et al., 2010; Moore, 2010).

Intertidal discharge to the ground surface can occur from faults and fractures that provide preferential paths for groundwater flow (Taboroši et al., 2013). An example of fracture-controlled point discharge was analysed by El Hage et al. (2020), who used thermal satellite images from the Lebanese coastal region to study groundwater seeps. They identified point discharge zones, and mapped faults and fractures to assess the possibility of using fracture-controlled groundwater discharge as an alternative source of freshwater. Groundwater discharge through discrete flow features may lead to the ejection of sand from the sub- surface (e.g., de Louw et al., 2010; Werner et al., 2020). De Louw et al. (2010) described groundwater vents through which sediment is brought to the surface by the action of groundwater discharge as sand boils. In the sand boils that they studied, the vents arose from heave and frac- turing of peat layers within Dutch polders. Werner et al. (2020) distinguished sand boils from boiling sand, whereby the latter was used when the sediment surface appears as a boiling fluid of more distributed sediment movement than the isolated vents of sand boils.

A number of techniques have been applied previously to characterise point discharge features. The most common of these methods are based on temperature and salinity variations (Taniguchi et al., 2019). For example, thermal infrared (TIR) imaging has been used to map diffuse seepage and point discharge in coastal environments, where there is a thermal contrast between groundwater and seawater (e.g., Danielescu et al., 2009). Mulligan and Charette (2006) and Duarte et al. (2006) used airborne TIR images to delineate the spatial variability of diffuse discharge in Waquoit Bay (Massachusetts) and western Hawai'i, respectively. Röper et al. (2014) used ground-based handheld TIR imagery to detect and map the horizontal extent of intertidal springs in north-western Germany.

Geochemical tracers are widely used techniques in groundwater discharge studies that provide information on the origin, composition and age of groundwater (Aggarwal et al., 2009). The radioactive isotope radon is frequently used in submarine groundwater discharge (SGD) investigations (Cable et al., 1996; Burnett et al., 2006; Povinec et al., 2012), as it is often several orders of magnitude more concentrated in groundwater than in surface waters (Burnett and Dulaiova, 2006; Tait et al., 2013). Short et al. (2014) used radon measurements of the surf zone and porewater from beach sediments to characterise potential SGD along the coastline of the Willunga Basin in South Australia (from Moana Beach to Sellicks Beach). Their results indicated potential groundwater discharge zones along the coastline. The stable isotopes of water, ^{2}H and ^{18}O have also been used to characterise groundwater and seawater mixing (Terwey, 1984). For example, Povinec et al. (2006) used δ^{2}H and δ^{18}O data to investigate the mixing between groundwater from springs and seawater along the coast of Sicily. Their results showed that the spring water composition consisted of up to 50 % continental groundwater.

In coastal areas, electromagnetic (EM) geophysical methods have been applied to study the groundwater salinity variability within sub- surface sediments (Yechieli et al., 2001; Schneider and Kruse, 2003; Levi et al., 2008). For example, Paepen et al. (2020) conducted EM surveys to map groundwater discharge along the coast of Belgium. Their results identified a large zone (>100 m) of low bulk conductivity (3.5 to 6.5 mS/cm), associated with diffuse groundwater discharge, and concluded that EM techniques provide valuable information for intertidal groundwater discharge investigations.

Each of the techniques described above (hydrochemical and environmental tracers, temperature-based methods, EM geophysical methods) offer useful insights into subsurface processes within intertidal zones. However, these methods are more usually adapted in combina- tion (rather than in isolation) due to limitations in their spatial and temporal resolution and in the information content of each (e.g., Stie- glitz, 2005; Swarzenski and Izbicki, 2009). This way, valuable information of point discharge features can be obtained to determine their spatial extent, geometry, water quality and mixing patterns within dy- namic intertidal zones.

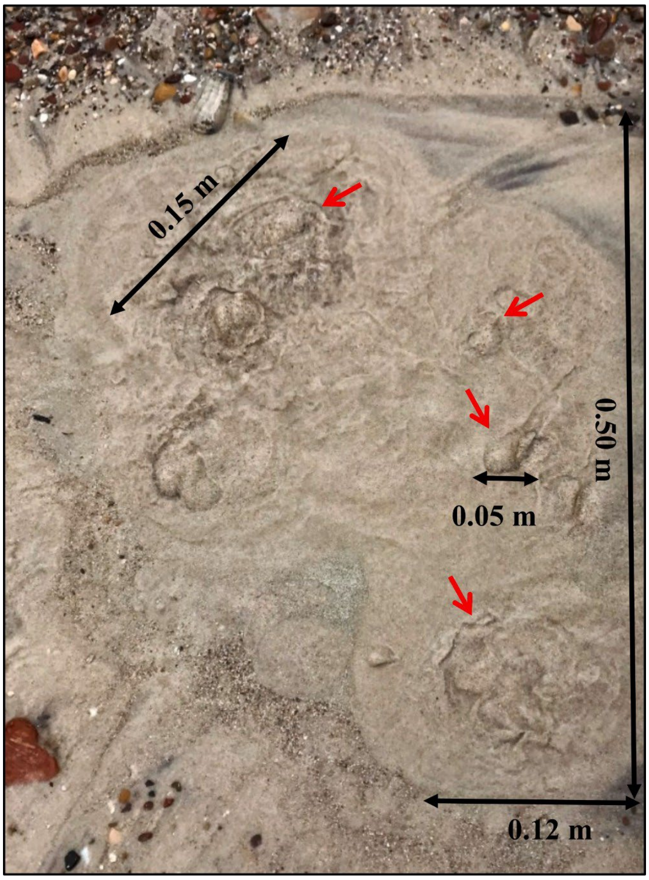

Fig. 1. Photo showing an example of an intertidal spring (Spring F; location shown in Fig. 4) at Sellicks Beach, South Australia. Image shows sand boils (red arrows) with diameters ranging from 0.05 to 0.15 m.

The aim of this study was to characterise intertidal springs discharging from a structurally complex coastal multi-aquifer system, located in Sellicks Beach, South Australia. Fig. 1 shows an example of the springs targeted in this research. The methodology applied in this investigation aimed to evaluate their spatial distribution, extent, temporal variability, origins and groundwater–seawater mixing patterns. A combination of near-surface EM geophysical techniques, stable isotopes (^{2}H and ^{18}O), water levels, electrical conductivity (EC), pH and TIR imagery was applied. This research describes the first published attempt (to the authors' knowledge) to obtain detailed measurements and sampling of intertidal sand boils, thereby adding to the existing knowledge base of intertidal hydrological processes.

Study site

The study site is located at Sellicks Beach, in the southwest of the Willunga Basin, approximately 46 km south of Adelaide, South Australia (Fig. 2). At this location, there are intertidal springs that appear as groupings of sand boils at various locations above the low-tide mark.

The Mediterranean climate of the study area comprises hot, dry summers and cold, wet winters, with mean annual rainfall of approximately 442 mm/yr (Noarlunga, Bureau of Meteorology station: 023885; Bureau of Meteorology, 2020). Measurements of sand boils at Sellicks Beach were undertaken during May 2017 (early winter), November 2019 (late spring) and September 2020 (early spring). The average minimum and maximum air temperatures recorded at the Bureau of Meteorology station 023885 were (respectively) 13.2 ˚C and 22.0 ˚C in 2017, 12.9 ˚C and 22.3 ˚C in 2019, and 12.3 ˚C and 21.2 ˚C in 2020. In May 2017, the average maximum and minimum daily temperatures were 17.3 ˚C and 11.1 ˚C, respectively. In November 2019, maximum and minimum temperatures were 22.7 ˚C and 12.4 ˚C, respectively, on average. Whereas in September 2020, the average maximum and minimum daily temperatures were 13.0 ˚C and 8.6 ˚C, respectively (Bureau of Meteorology, 2020). The adjacent St Vincent Gulf is mostly microtidal (~2 m tidal range) with moderate wave energy.

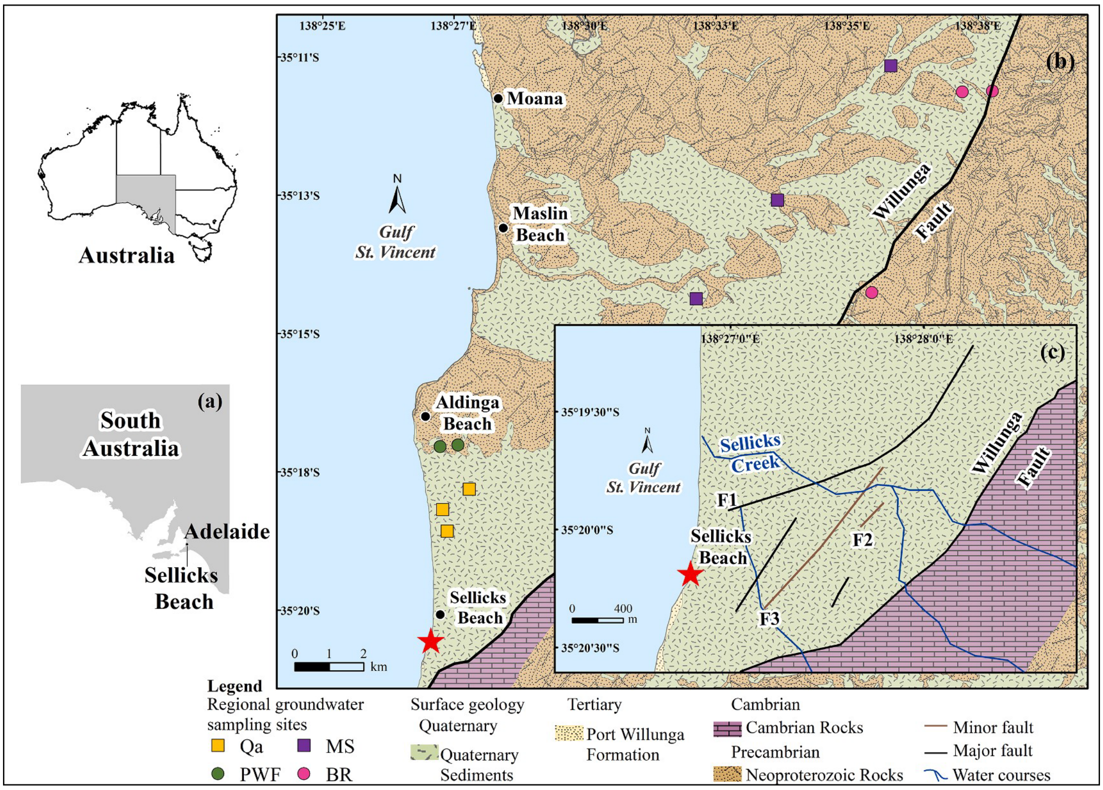

Fig. 2. Locality map of Sellicks Beach and the surrounding area: (a) Location of Sellicks Beach within South Australia, (b) Map of the southern Willunga Basin, showing surface geology, the Willunga Fault and regional groundwater sampling points (see Table 1) in the Quaternary (Qa), Port Willunga Formation (PWF), Maslin Sands (MS) and basement rocks (BR) aquifers, and (c) inset map, showing local water courses, and major and minor faults near the study site.

The sedimentary aquifers within the Willunga Basin provide fresh groundwater for the irrigation of vineyards and other agricultural crops (e.g., barley, wheat, almonds and olives) (Harrington and Cook, 2012; Bardsley et al., 2017). The Willunga Basin is comprised of fluvial Quaternary sediments, overlying mid- to late-Tertiary marine fossiliferous strata (Port Willunga Formation, Blanche Point Formation, Maslin Sands Formation), which are underlain by Precambrian/Cambrian basement rocks (Fairburn, 1998). The wedge-shaped basin bounded to the east and south by the Willunga Fault, is part of the much larger St Vincent Basin, which formed during the continental separation of Australia and Antarctica ~43 million years ago (Dyson, 1998; Martin, 1998). According to monitoring wells located in the southwest of the Willunga Basin (~6 km northeast of the study site), groundwater levels in the Port Willunga Formation aquifer from the last 10 years have been largely stable, with maximum fluctuations of ~1 m. Groundwater levels within the Maslin Sands and basement rock aquifers have also remained fairly stable (maximum fluctuations of ~0.5 m) (DEW, 2021).

At Sellicks Beach, the Port Willunga Formation (PWF) outcrops as low coastal cliffs (Fig. 3), which have experienced significant erosion, deep gullying and rotational slumping, creating a series of alluvial fan sediments and platforms (Bourman et al., 2016). In a study by May and Bourman (1984), they identified in the southern area of the beach, an extensive platform of the PWF that outcrops within the intertidal zone, and that contributes to concentrated marine erosion of the cliffs. Sediments at the beach consist of sand and gravels, with seasonal variations in sediment transport leading to geomorphic changes in the beach profile and sediment distribution. For example, Cann et al. (2014) observed that in summer, the volume of sand is greater compared to winter, when higher wave energy exposes the PWF platform, leaving gravels and sand visible only in narrow areas along the beach at low tide. They also established that the cobble-size gravels originate from the Neoproterozoic and Cambrian rocks outcropping nearby and are trans- ported to the beach by coastal erosion as well as being impacted by northward longshore transport.

In the Willunga Basin, neotectonism has highly influenced the geological setting of the coastline (Preiss, 2019), where active normal, reverse and oblique faulting has been documented (Jayawardena, 2013; Preiss, 2019). The Willunga Fault (location shown in Fig. 2) is an active reverse fault, NE-SW oriented (Tokarev, 2005; Lubiniecki et al., 2019). The stratigraphy at Sellicks Beach is complex (Fig. 3), where tectonic activity and marine erosion have created a large rotational land slump and unstable cliffs, due in part to its proximity to the Willunga Fault and the occurrence of numerous smaller faults in the area (May and Bour- man, 1984). For example, geophysical investigations by Reed (1982) were able to identify an extensive fault zone north of the main Willunga Fault, located at the top of the PWF cliffs approximately 200 m from the study site, and possibly extending further to the west. The fault zone consists of a major fault (F1) and two minor faults (F2 and F3) shown in Fig. 2. Additionally, Lubiniecki et al. (2019) identified small faults (‘deformation bands’; Aydin, 1978) with displacements of a few milli- metres in the PWF cliff faces, approximately 60 m from the study site.

Martin (1998) defined the Willunga Basin as a complex multi-aquifer system, where regional groundwater flows from the northeast of the basin towards the coast. The basin comprises four main hydrogeological units, Quaternary (Qa), PWF, Maslin Sands (MS) and fractured basement rocks (BR) (see Fig. 3). The Quaternary aquifer is mainly unconfined and considered as a low yielding aquifer. The main sources of groundwater within the basin are the Maslin Sand and the PWF aquifers (Knowles et al., 2007). Rainfall and streambed infiltration recharge the Qa, PWF and MS aquifers, while lateral inflows to lower units from the Precambrian/Cambrian basement rocks aquifer also occur at the boundary of the basin (Adelaide and Mount Lofty Ranges NRM Board, 2007; Sha-nafield et al., 2020).

Groundwater discharge from the Willunga Basin’s aquifers to the sea has been described in previous studies (Martin, 1998; Lamontagne et al., 2008; Short et al. 2014; Post et al. 2018). The limited groundwater monitoring along the Willunga Basin coastline makes it challenging to estimate groundwater discharge to the sea (Lamontagne et al., 2008). Nevertheless, Lamontagne et al. (2008) used a flow net methodology to calculate discharge rates of 670 ML/yr from the PWF and 120 ML/yr from the MS aquifers. Short et al. (2014) obtained EC and ^{222}Rn measurements of the intertidal zone and within beach sediments from part of the Willunga Basin coastline and found groundwater discharge to the sea to be spatially intermittent. Therefore, Lamontagne et al.’s (2008) assumption that groundwater discharge occurs along the entire coastline likely overestimated discharge rates to the ocean.

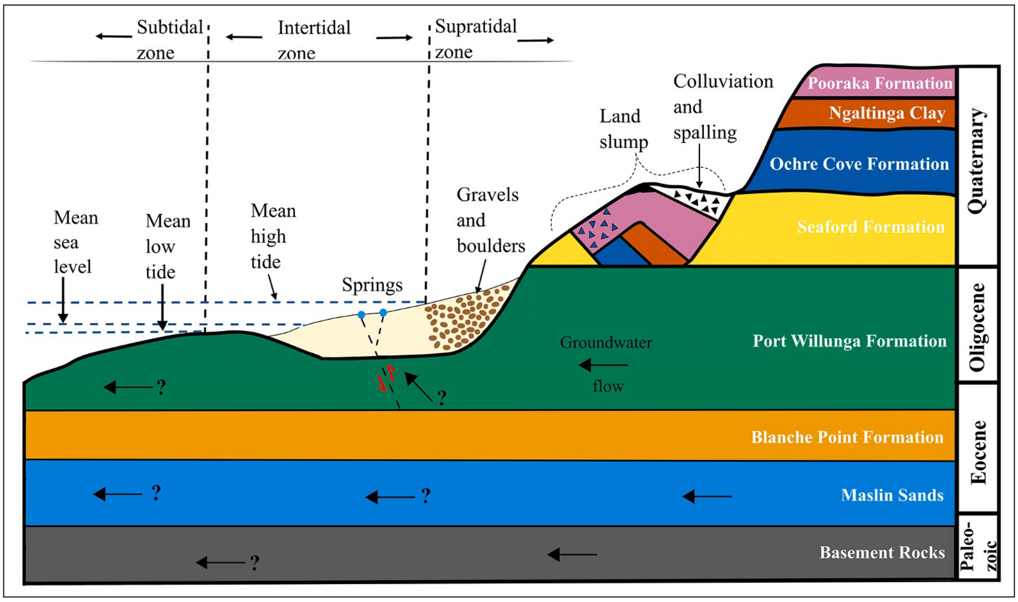

Fig. 3. Conceptual model of the intertidal zone, and the location of the springs at Sellicks Beach. The following geological formations are represented in the idealised cross-section: Quaternary (sands and interbedded clays), Port Willunga Formation (sands and limestone), Maslin Sands (sands and clays) and basement rocks (slate, quartzite and shale). Modified geological cross section from Cann et al. (2014). Not to scale.

Methods

Field investigations were designed to explore the characteristics of intertidal springs and were conducted at the southern end of the Sellicks Beach coastline (Fig. 2). At this location, intertidal springs occur as groupings of closely spaced sand boils (e.g., Fig. 1). Field investigations were undertaken between 23 and 26 May 2017, 14 November 2019 and 17 to 18 September 2020. In the 2017 field campaign, Spring D was visible during daytime, and Springs A, B and C were visible to the naked eye only at night.

We speculate that changes in the beach profile (e.g., sand thickness) and tidal fluctuations may explain why Springs A, B and C were only observed at night and not during daylight hours. Average daytime low tide was 0.73 m, while average night-time low tide was 0.45 m (Bureau of Meteorology, 2017). Further observations are required to improve the current understanding of spring temporal variability at the field site. Springs E and F were visible in the daytime and only during the 2019 field campaign. During the 2020 field campaign, Spring G was visible in the daytime (Fig. 4). Additional intertidal observations from the 2020 campaign included the measurement of the thickness of the sand overlying the PWF. This involved the use of a solid metal stake to determine the depth of refusal to the more competent PWF formation.

EM geophysical measurements of the subsurface were collected at low tide over the study site using a CMD-Explorer instrument (https://www.gfinstruments.cz), with apparent conductivity (mS/m) measurements recorded every 1 *sec* along a survey grid and locations determined using a Real Time Kinematic (RTK) positioning instrument (https://www.trimble.com). The CMD-Explorer is a ground-based, multi-depth EM instrument that measures both in-phase and out-of- phase data at set time intervals. The instrument has an operating frequency of 10 kHz and has three receiver coils, with 1.48, 2.82 and 4.49 m intercoil spacings. These three transmitter-receiver coil separation spacings and frequency output provide an effective depth of investigation of 2.2, 4.2 and 6.7 m (horizontal coplanar configuration, high-depth mode). The out-of-phase data that the instrument records are converted to apparent conductivity, using a low induction number approximation (McNeill, 1980). Data inversion was conducted using the Aarhus Workbench software package (https://www.aarhusgeosoftware. dk). The inversion routine uses the AahusInv code (Auken et al., 2015), previously used for ground-based EM data (Christiansen et al., 2016). Inverted data in the results section is presented as resistivity (ohm.m; equivalent to 1/apparent conductivity (S/m)). The EM survey comprised a survey grid of 20 transects, which included 9 north-south transects lines of 50 m length, and 11 east-west transects lines of 25 m (Fig. 4). The inverted data were collated, and nearest neighbour interpolation was used to create resistivity layers of the study site with the software package Surfer 11 (https://www.goldensoftware.com). During the May 2017 field campaign, a TIR mapping survey was used to evaluate the spatial distribution of the groundwater discharge from the springs within the intertidal zone. The survey was conducted using a handheld FLIR E5-XT thermal camera with a measurement range of –20 to 400 ˚C and measurement accuracy of ± 2 ˚C. The TIR mapping was conducted at low tide when the springs were exposed and at night to avoid solar interference on the thermal signature of the springs.

Fig. 4. Location of the intertidal springs at Sellicks Beach. Survey

transect lines (yellow) from the EM geophysical survey are also shown and the dashed lines represent average low and high tide levels (Bureau of Meteorology, 2020) at Sellicks Beach.

The 2017 field campaign involved sampling seawater and Spring D for salinity (EC), temperature, pH and the stable isotopes of water. EM geophysical surveys, TIR mapping of the study site and water level time series measurements from a shallow piezometer installed in Spring D was also undertaken. During the 2019 field campaign, only salinity, temperature, pH and the stable isotopes of water were sampled in Springs E and F. The 2020 field campaign involved seawater and Spring G sampling for salinity, temperature, pH, the stable isotopes of water and sand thickness measurements.

Water samples were collected from Springs D, E, F, G and the sea using a hand pump connected to a 1-m length of flexible hosing. EC, pH and temperature were measured in the field using a handheld YSI® multi-parameter probe. Spring and seawater samples were obtained approximately every 12 h for 3 days during the 2017 field campaign. In the 2019 campaign three spring and seawater samples were obtained (at 30 min intervals) during low tide. Spring and seawater samples were obtained approximately every 15 min for 2 days at low tide, during the 2020 field campaign. Samples were filtered (0.45 µm) and collected in 2- mL glass vials to analyse the stable isotopes of hydrogen (^{2}H) and oxygen (^{18}O), using a Picarro L2130-*i* Isotope δ^{18}O/δ^{2}H Ultra High Precision Isotopic Water Analyser (Picarro, 2020). Results are reported against the Vienna Standard Mean Ocean Water (VSMOW) in per mil (‰), using delta (δ) notation.

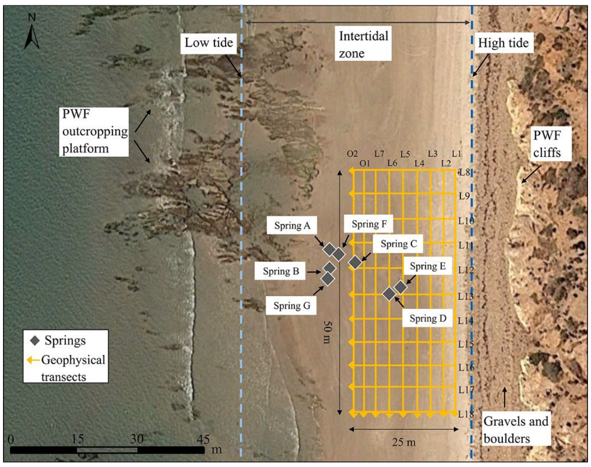

A shallow polyvinyl chloride (PVC) piezometer was installed in Spring D (see Fig. 4) to a depth of 0.76 m and protruded to a height of 0.5 m above ground. The piezometer had a 0.1 m long slotted screen and was equipped with an In-Situ Aqua TROLL 200® datalogger to record temperature, pressure and EC at 1-minute intervals from 23 to 26 May 2017. Due to the location of the spring in the intertidal zone, seawater entered the piezometer during high-tide periods. Another In-Situ Aqua TROLL 200® datalogger was deployed offshore of the study site to measure the tidal fluctuations during the 2017 field campaign.

Results

1.1. Spring observations

The physical location and size of the springs within the intertidal zone of Sellicks Beach changed between the three field campaigns. In May 2017 (Southern Hemisphere winter), four springs (Springs A, B, C and D) were identified, while in November 2019 (Southern Hemisphere late spring) only two springs were identified (Springs E and F) and September 2020 (Southern Hemisphere early spring), only Spring G was observed. The diameter of the sand boils within the springs also showed distinct differences within Spring F (November 2019, Fig. 1) had an average diameter of 0.1 m, while the sand boils from the observed springs identified in the 2017 and 2020 campaigns were considerably smaller, with an average diameter of 0.01 m. The thickness of the sand layer measured in the 2020 campaign varied from 0.82 m to 0.38 m (east–west), decreasing towards the sea and from 0.45 m to 0.64 m (north–south). Particularly, the sand thickness at the location of Springs A, B, C, D, E and F was 0.43, 0.41, 0.54, 0.70, 0.69 and 0.45 m, respectively.

1.2. EM geophysical survey

The data from the EM geophysical survey showed the spatial variability in the resistivity of the subsurface around Spring D to a depth of 6.7 m based on the transmitter and receiver separations of the CMD instrument (Fig. 5). The 2.2 m depth slice of the inverted resistivity data, shows a central, more resistive anomaly (10×12 m) of about 5 ohm.m (compared to the surrounding material), located directly beneath the visible surface expression of Spring D. This central anomaly represents spring discharge of groundwater from the saturated sand and sediments of the underlying PWF. The eastern boundary up against the base of the PWF cliffs has resistivity values of ~2.0 ohm.m and is influenced by an increase in thickness of unsaturated beach sediments, including the existence of gravels and boulders. To the north and south (along the beach) of the central anomaly there are resistivity values of <1.5 ohm. m, associated with seawater saturated sand and PWF sediments. The depth slice at 4.2 m depth shows a similar spatial distribution of re- sistivity values as the shallow layer at 2.2 m depth. Meanwhile, the depth slice at 6.7 m depth shows that the size of the resistivity anomaly is influenced by Spring D and increased by 5 m along the length of the western boundary (seawards).

Transect line L6 parallel to the coastline shows that the resistive anomaly (5 ohm.m) located below the surface expression of Spring D is present across the vertical extent of the depth profile (Fig. 6). Low re- sistivity (<1.5 ohm.m) zones in the north and south of the profile, associated to the seawater saturated sand and PWF sediments, extend from the surface to 3 m below the ground. In particular, a low resistivity feature (~1.0 ohm.m) is present across the profile (north-south) at 0.5 m below the ground level and correlates with the average sand thickness measured in the area.

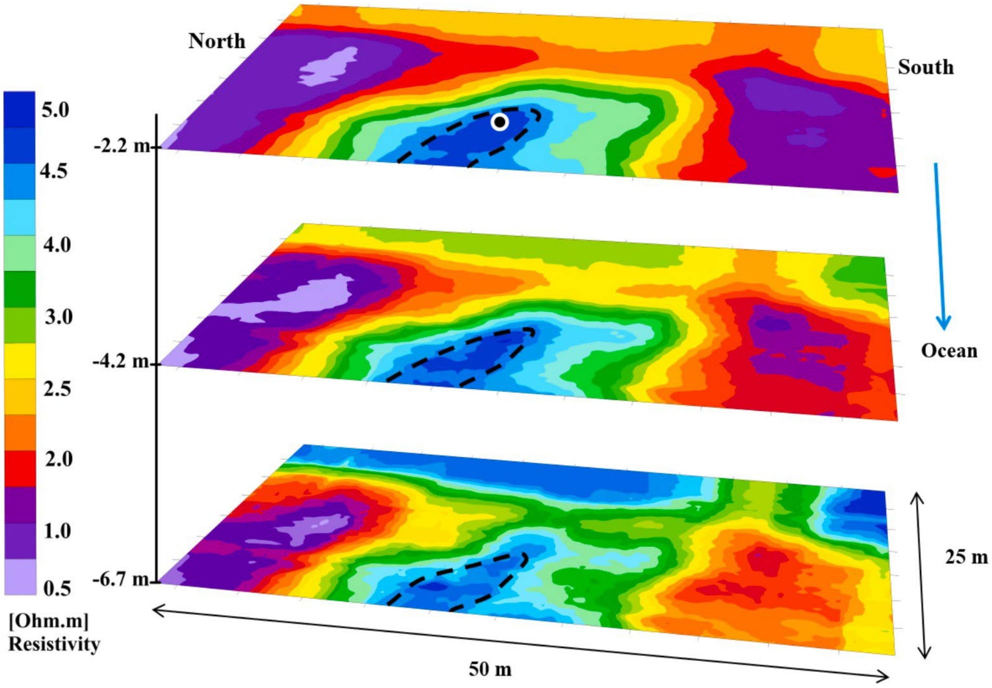

Fig. 5. Multi-depth resistivity model of inverted EM data collected across the 20 transect lines (survey grid 50 × 25 m) at the study site. A more resistive zone is present at the location of Spring D (black circle) and increases in size towards the seaside of the model domain. The dashed line represents the central, resistive anomaly created by groundwater discharge from Spring D (5.0 ohm.m).

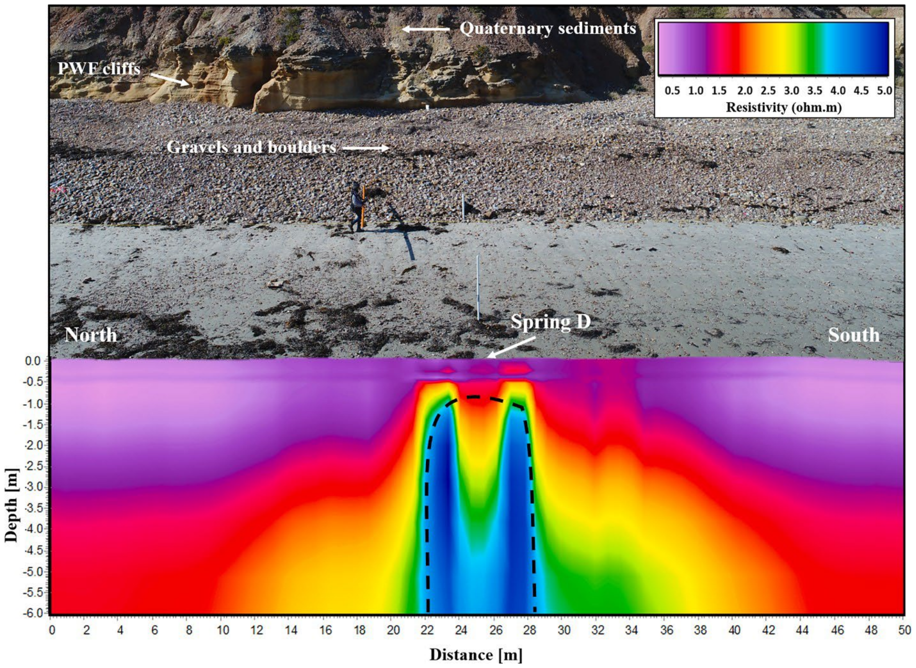

Fig. 6. North-south EM transect line (L6) depth profile overlaid on aerial imagery. The dashed line represents the resistive anomaly (5.0 ohm.m) near Spring D.

1.3. TIR mapping survey

The ground-based TIR mapping was used to identify discrete groundwater discharge features that were not visible to the naked eye during the daytime (Fig. 7). Specifically, this method detected three additional springs in the vicinity of Spring D (Springs A, B and C; Fig. 4) at night during the May 2017 campaign. The approximate diameter of Springs A-D ranged from 0.20 to 0.45 m, based on the thermal imagery and where the temperature changed from 7 to 19 ˚C. The size of the sand boils within the springs had diameters ranging from 0.005 to 0.15 m. The temperature of the springs (~19 ˚C) was distinctively higher than the adjacent seawater and saturated sand (~7 ˚C), and the measured ambient air temperature (10 ˚C). The heat map showed that the flow direction of the springs followed the downward slope of the beach to- wards the sea. The temperature of the springs detected with the thermal camera was similar to the measured average temperature (21.2 ˚C) of the discharging water in Spring D using the multi-parameter probe at low tide (Table 1). Temperature data from regional groundwater and the springs was higher, compared to seawater and ambient air. Average groundwater temperature from the Qa and PWF aquifers was 18 ˚C and 23.4 ˚C, respectively. Whereas average groundwater temperature from the deeper MS and BR aquifers was 21 ˚C and 22.8 ˚C, respectively (Table 1).

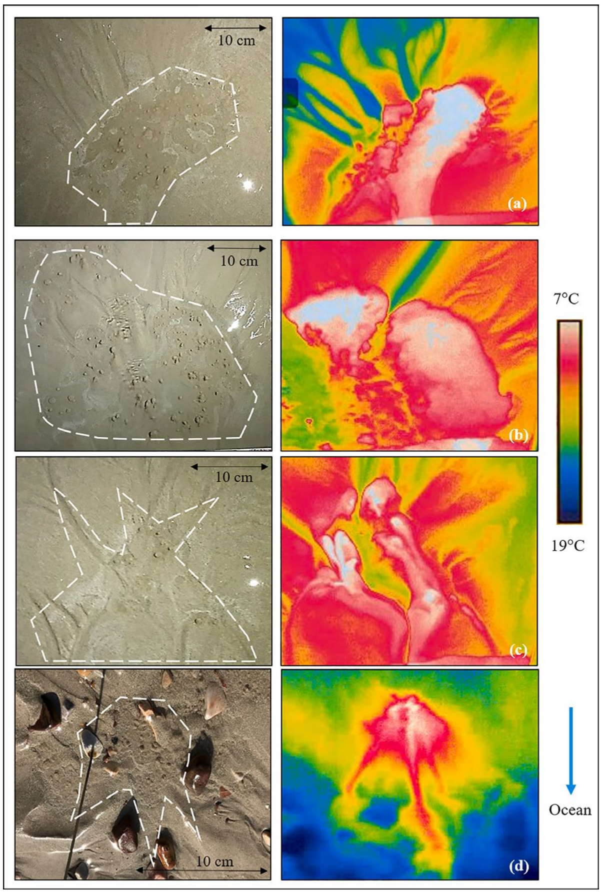

Fig. 7. Visible light and thermal images of the four intertidal springs from the 2017 field campaign. (a) Spring A, (b) Spring B, (c) Spring C, and (d) Spring D. The dashed white circles shown in the visible light images highlight the location of spring discharge and the sand boils within the springs. For spring location, see Fig. 4. The blue arrow shows the downward slope of the beach towards the sea. (For interpretation of the references to colour in this figure legend, the reader is referred to the web version of this article.)

Table 1

δ^2H and δ^{18}O, EC, pH and temperature data from sampled Springs D, E, F and G, seawater, local rainfall, and regional groundwater from the Quaternary aquifer (Qa), the Port Willunga Formation (PWF), the Maslin Sands aquifer (MS) and the basement rocks (BR). See Fig. 2 for location of the regional groundwater monitoring wells. Elevation data and water levels are reported in metres above the Australian Height Datum (m AHD, approximately mean sea level). ND = no data. NA = not applicable.

Sample source	Sample date/time	Tide level	Easting	Northing	Elevation	δ^{18}O	δ^2H	EC	T	pH
					(m AHD)	(‰, VSMOW)		mS/cm	˚C	
Spring D	24/05/17 9:45	low	267879	6086627	0.60	−2.4	−13.3	27.7	20.6	7.31
	24/05/17 19:30	high				1	6.3	54.3	20.2	7.74
	24/05/17 22:30	mid				−0.4	−1.5	55.8	20.6	7.54
	25/05/17 10:10	low				−2.8	−16.4	26.7	21.3	7.03
	25/05/17 23:00	mid				−0.5	−2.6	31.8	21.1	7.59
	26/05/17 11:30	low				−3.6	−20.5	20.2	23.3	7.28
	26/05/17 11:00	low				−2.5	−15.2	ND	ND	ND
Spring E	14/11/19 12:09	low	267880	6086627	0.08	−3.9	−21.4	16.9	18.3	6.98
	14/11/19 12:37	low				−3.9	−21.8	16.5	21.0	6.97
Spring F	14/11/19 13:02	low	267866	6086638	−0.37	−3.8	−21.4	17.0	21.1	6.88

Table 1 (*continued*)

Sample source	Sample date/time	Tide level	Easting	Northing	Elevation (m AHD)	$\delta^{18}O$ (‰, VSMOW)	δ^2H	EC mS/cm	T ˚C	pH
Spring G	17/09/20 11:28	low	267866	6086635	−0.18	−3.9	−23.1	13.2	18.3	6.88
	17/09/20 11:45	low				−4.2	−24.0	13.2	18.5	6.81
	17/09/20 12:00	low				−4.4	−25.2	13.3	17.6	6.91
	17/09/20 12:12	low				−4.2	−24.5	13.0	17.6	6.84
	17/09/20 12:29	low				−4.2	−24.4	13.4	17.3	6.96
	17/09/20 12:59	low				−4.4	−24.9	12.9	18.6	6.70
	17/09/20 13:15	low				−4.4	−25.0	13.2	19.5	6.83
	18/09/20 10:03	low				−4.4	−25.1	13.0	22.1	6.87
	18/09/20 10:19	low				−4.4	−24.7	12.9	21.8	6.84
	18/09/20 10:36	low				−4.3	−24.2	13.0	21.7	6.74
	18/09/20 10:50	low				−4.4	−24.7	13.1	21.6	6.77
	18/09/20 11:20	low				−4.4	−25.5	13.2	21.8	6.85
	18/09/20 11:35	low				−4.4	−25.3	13.1	22.4	6.84
	18/09/20 11:50	low				−4.4	−25.0	13.1	23.1	6.80
	18/09/20 12:15	low				−4.4	−25.0	13.0	22.7	6.86
	18/09/20 12:33	low				−4.4	−25.0	12.9	22.7	6.79
	18/09/20 13:15	low				−4.3	−25.1	13.0	23.5	6.85
	18/09/20 13:30	low				−4.8	−26.0	12.9	23.3	6.76
	18/09/20 13:50	low				−4.7	−25.4	12.9	23.1	6.83
Seawater	24/05/17 9:45	low	267832	6086627	NA	0.8	5.0	57.0	19.8	7.70
	24/05/17 22:30	high				0.6	2.4	56.6	18.8	7.84
	25/05/17 19:00	mid				0.9	5.5	56.2	19.6	ND
	17/09/20 11:00	low	267830	6086640	−0.50	0.9	5.5	54.4	14.9	7.69
	17/09/20 11:30	low				1.1	6.7	54.5	14.7	7.74
	17/09/20 12:00	low				1.0	6.6	54.8	14.7	7.57
	17/09/20 12:29	low				1.0	6.6	54.9	14.9	7.58
	17/09/20 13:00	low				0.8	4.6	54.0	14.9	7.72
	18/09/20 9:31	low				1.1	6.0	54.5	18.0	7.79
	18/09/20 10:08	low				1.0	5.9	54.5	16.3	7.84
	18/09/20 10:36	low				0.9	5.9	54.1	16.2	7.82
	18/09/20 11:07	low				0.8	4.4	54.3	18.9	7.67
	18/09/20 12:00	low				0.9	5.0	54.2	17.3	7.65
	18/09/20 12:36	low				0.8	5.0	54.6	18.8	7.77
	18/09/20 13:00	low				0.8	4.2	54.1	18.1	7.74
	18/09/20 13:30	low				0.8	5.1	54.6	18.0	7.59
	18/09/20 13:50	low				0.9	5.2	54.2	20.3	7.70
Rainfall	05/17	NA	273533	6129692	2.00	−3.9	−18.7	ND	ND	ND
						−5.3	−24.8			
						−3.5	−12.5			
Qa	03/08/11	NA	268211	6090419	12.00	−4.6	−21.3	17.8	17.7	7.90
	05/08/11		268342	6089792	6.00	−4.3	−20.7	13.7	17.7	8.00
	29/08/11		268979	6091009	17.00	−4.6	−21.6	15.6	18.5	7.60
PWF	06/02/13	NA	268134	6092241	19.10	−4.6	−21.6	4.0	21.5	7.10
	06/02/13		268139	6092241	18.90	−4.2	−20.3	6.0	ND	7.30
	07/02/13		268652	6092289	20.90	−4.7	−21.3	3.1	24.2	7.40
	07/02/13		268655	6092289	20.90	−4.7	−23.6	2.7	24.6	8.10
MS	01/04/13	NA	275556	6096525	60.90	−5.1	−29.3	2.5	22.2	6.67
	01/10/12		277909	6099383	63.30	−5.4	−29.3	2.7	19.5	7.04
	01/04/13		281190	6103272	96.30	−5.2	−28.9	1.7	21.3	6.38
BR	01/03/14	NA	280643	6096705	182	−4.9	−26.6	1.4	18	7.20
	01/05/14		284135	6102541	211	−5.0	−27.0	2.0	26	7.50
	01/03/14		283263	6102519	163	−5.5	−30.6	5.3	24.4	7.00

1.4. EC, pH and stable isotopes of water

EC (measure of salinity), pH, $\delta^{18}O$ and δ^2H data from the springs, seawater, and regional groundwater from the Willunga Basin are given in Table 1. There was significant variability in the EC between sampling campaigns and the four major springs. Spring D (2017 campaign) had an average EC value of 24.8 mS/cm at low tide, whilst at mid to high tide the EC was 47.3 mS/cm. At low tide, the average EC recorded in Springs E and F (2019 campaign) was 16.7 mS/cm, whereas Spring G (2020 campaign) had a lower average EC of 13.1 mS/cm at low tide. In com- parison, the measured average seawater EC was 56 mS/cm during the 2017 campaign, whereas during the 2020 campaign it was 54.4 mS/cm. Average salinity values from regional groundwater from the Qa and PWF aquifers (see Fig. 2 for well locations) was 15.7 mS/cm and 3.95 mS/cm, respectively. Whereas average salinity values from the deeper MS and BR aquifers (see Fig. 2) was 2.3 mS/cm and 5.16 mS/cm, respectively.

In the 2017 field campaign, Spring D had an average pH at low tide and mid-high tide of 7.2 and 7.6, respectively. Springs E and F (2019 campaign) had an average pH of 6.9 and Spring G (2020 campaign) had the lowest average pH (6.8) at low tide. The average seawater pH of the 2017 and 2020 field campaigns only varied between 7.7 and 7.8.

Average pH values from four observation wells in each of the regional Qa, PWF, MS and BR aquifers were 7.8, 7.4, 6.7 and 7.2, respectively (NCRIS Groundwater Database, 2022). Overall, the recorded pH in the springs from the three field campaigns was lower than in the adjacent seawater. Samples collected over the mid and high tide periods showed increasing pH, which corresponded with increases in salinity.

Rainfall isotope data from May 2017 were obtained from the Australian Global Network of Isotopes in Precipitation (GNIP) for Adelaide (BOM station: 94672; Bureau of Meteorology, 2020) and plot adjacent to the Adelaide Local Meteoric Water Line (LMWL) and varied from δ^2H −3.5 to −5.3 ‰, and δ^{18}O from −12.4 to −24.8 ‰ (Fig. 8). Regional groundwater samples from the Qa aquifer (see Fig. 2 for locations) had δ^2H values that ranged from −21.6 to −20.7 ‰ and δ^{18}O values that ranged from -4.6 to -4.2 ‰. In contrast, groundwater from the PWF aquifer showed relatively more depleted δ^2H and δ^{18}O values ranging from –23.6 to -20.2 ‰ and from -4.7 to -4.1 ‰, respectively. δ^2H and δ^{18}O samples from the deeper aquifers, the MS and BR, were more depleted than the overlying PWF and Qa aquifers, varying from -26.6 to -30.6 ‰ and from −5.5 to -4.9 ‰, respectively.

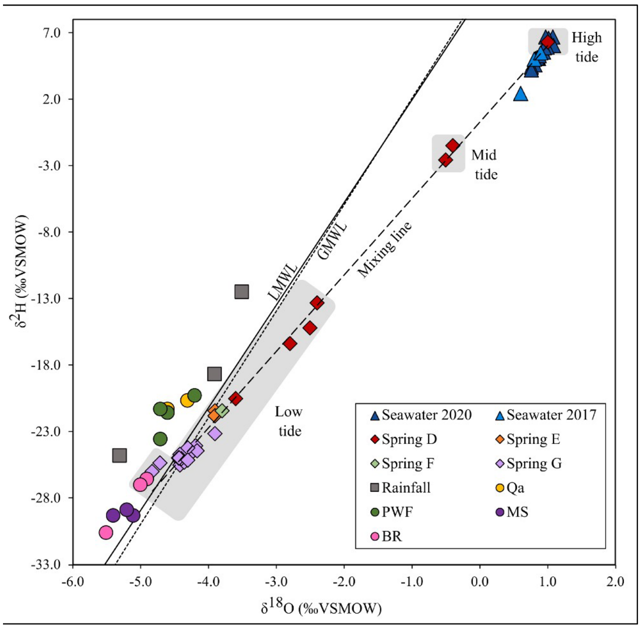

Fig. 8. δ^2H versus δ^{18}O for sampled Springs D, E, F and G, seawater, regional groundwater and rainfall. The Adelaide Local Meteoric Water Line (LMWL) is $\delta^2H = 7.7\delta^{18}O + 9.6$ (Banks et al., 2009) and the Global Meteoric Water Line (GMWL) is $\delta^2H = 8\delta^{18}O + 10$ (dashed line; Craig, 1961). Regional groundwater includes samples from the Quaternary (Qa), Port Willunga Formation (PWF), Maslin Sands (MS) and basement rock (BR) aquifers. The spring water mixing line between the end members of seawater and regional groundwater is $\delta^2H = 5.9\delta^{18}O + 0.5$ with and R^2 value of 0.99.

The δ^{18}O and δ^2H values of the springs fall to the right of the LMWL, with δ^2H varying from −20.5 to 6.3 ‰, and δ^{18}O from −3.6 to 1.0 ‰ for Spring D (2017 campaign) (Fig. 8). Depleted values from Spring D were identified at low tide periods (δ^2H = −20.5 ‰, and δ^{18}O = −3.6 ‰), while more enriched δ^2H and δ^{18}O values (δ^2H = 6.3 ‰, and δ^{18}O = 1.0 ‰) were recorded during mid- to high tide, indicating likely mixing with seawater, which had average δ^2H and δ^{18}O values of 4.3 ‰ and 0.8 ‰, respectively. δ^{18}O and δ^2H data from the 2019 field campaign, showed depleted values at low tide for Spring E and F, with δ^2H varying from −21.8 to −21.4 ‰, and δ^{18}O from −3.9 to −3.8 ‰. At low tide, average δ^2H and δ^{18}O data from Spring G (2020 campaign) was more depleted (−24.9 ‰ and −4.4 ‰, respectively) than the 2017 and 2019 samples. While average δ^2H and δ^{18}O from seawater (2020 campaign) was 5.5 ‰ and 0.9 ‰, respectively.

The proportion of regional groundwater (GW) and seawater (SW) mixing at Spring D was approximated using a simple binary-mixing approach (Table 2). Mixing calculations using average δ^{18}O values from Spring D at low tide from the 2017 campaign (−2.8 ‰), PWF (−4.6 ‰) and seawater (0.9 ‰) end-members, showed that spring discharge was comprised of approximately 67 % groundwater (PWF). At high tide, the more enriched average δ^{18}O (1.0 ‰) values from Spring D showed a high proportion of seawater (86 %) and lower groundwater contribution (14 %). Mixing calculations for Springs E and F (November 2019), using average δ^{18}O (−3.8 ‰) at low tide, resulted in a similarly high proportion of groundwater contribution (86 %) at the springs. Mixing calculations using average δ^{18}O data from Spring G (2020 campaign) at low tide (−4.4 ‰) also showed high groundwater contribution (97 %) to the spring mixture. Additional mixing calculations using δ^2H and EC data indicate that δ^2H data tends to overestimate the groundwater contribution to the springs compared to calculations based on δ^{18}O and EC (Table 2).

Table 2

Binary mixing calculations between groundwater (GW) and seawater (SW) end- members using δ^{18}O, δ^2H and EC data.

Groundwater-Seawater mixing								
Percentage (%)	2017				2019		2020	
Low tide			High tide Low tide		Low		tide	
	GW	SW	GW	SW	GW	SW	GW	SW
δ^2H	81	19	14	86	99	1	100	0
δ^{18}O	67	33	14	86	86	14	97	3
EC	60	40	18	82	76	24	82	18

The GW-SW mixing processes of the springs are presented in the EC vs δ^2H plot (Fig. 9). There are two well distinguished groups of samples, represented at the left side of the plot by regional GW (average δ^2H and EC values of −24.8 ‰ and 6.0 mS/cm, respectively), and on the right by the SW end-member (average δ^2H values of 4.3 ‰ and average EC of 56.6 mS/cm). The average δ^{18}O and δ^2H composition of the springs (−3.7 ‰, and −20.7 ‰, respectively) was similar to both the isotopic signature of the nearby Qa (δ^{18}O = −4.5 ‰ and δ^2H = −21.2 ‰) and PWF aquifers (δ^{18}O = −4.6 ‰ and δ^2H = −21.7 ‰), but significantly differed from the composition of the MS (δ^{18}O = –5.2 ‰ and δ^2H =–29.2 ‰) and BR (δ^{18}O = −5.1 ‰ and δ^2H = −28.1 ‰) aquifers. Our mixing processes analysis (Fig. 9) shows that the isotopic values of the springs more closely resemble those of the upper aquifers (Qa and PWF), rather than the deeper MS and BR aquifers, which show isotopic sig- natures that are more depleted. These results indicate that the GW contribution most likely originates from the upper aquifers rather than the MS and BR aquifers. However, given that there is no major difference in their isotopic composition, we cannot accurately determine which aquifer is the main supplier of fresh GW to the springs.

1.5. *Time series water level observations*

Time series water level observations from the shallow piezometer installed in Spring D together with measured sea levels offshore from the study site for the May 2017 field campaign are shown in Fig. 10. Over the field campaign period, sea level reached its maximum at ~1.0 m AHD at high tide, and then decreased to 0.4 m AHD at low tide. During high tide periods Spring D was fully inundated by seawater. Analysis of the measured sea and water levels over the 4 days of monitoring showed that the spring response to tidal sinusoidal oscillations varies asymmetrically at the location of Spring D, and that spring water levels are dependent on tidal range between 0.65 m AHD (high tide) to -0.46 m AHD (low tide). Time series measurements of EC at Spring D also showed a change in salinity with the tidal cycle (Fig. 10c). During high tide periods the average salinity was ~44 mS/cm, compared to low tide, where the salinity of Spring D reached its minimum of ~1.89 mS/cm. The time series EC results were consistent with measurements that were taken with a handheld YSI EC meter, where a maximum EC of 55.8 mS/cm was recorded during or shortly after high tide, and a minimum EC of 20.2 mS/cm observed during low tide periods. These salinity fluctuations with time show the influence of mixing seawater at the spring, where increasing salinity correlated to high tide periods, when Spring D was inundated by seawater. Over the measurement period, a time lag in the change in salinity at Spring D was occasionally observed. For example, on May 24, the high tide was recorded at 15:39, while the highest EC (53.3 mS/cm) was recorded at 19:38, ~3 h later (Fig. 10).

The average water temperature of Spring D was 18.4 °C, with a maximum value of 20.7 °C recorded at low tide, and minimum of 16.8 °C during high tide (Fig. 10b). In comparison, handheld measurements using TIR imagery at low tide showed average spring temperature values of 21.3 °C and seawater of 19.4 °C. The presence of seawater during high tide periods was represented by low temperature values (~17 °C), while daytime observations at low tide (i.e., 23/05/17, 11:00) showed increased temperatures values (~20 °C). Overall, these early winter transient temperature patterns seemed to be influenced by the interaction of ocean tides and solar radiation.

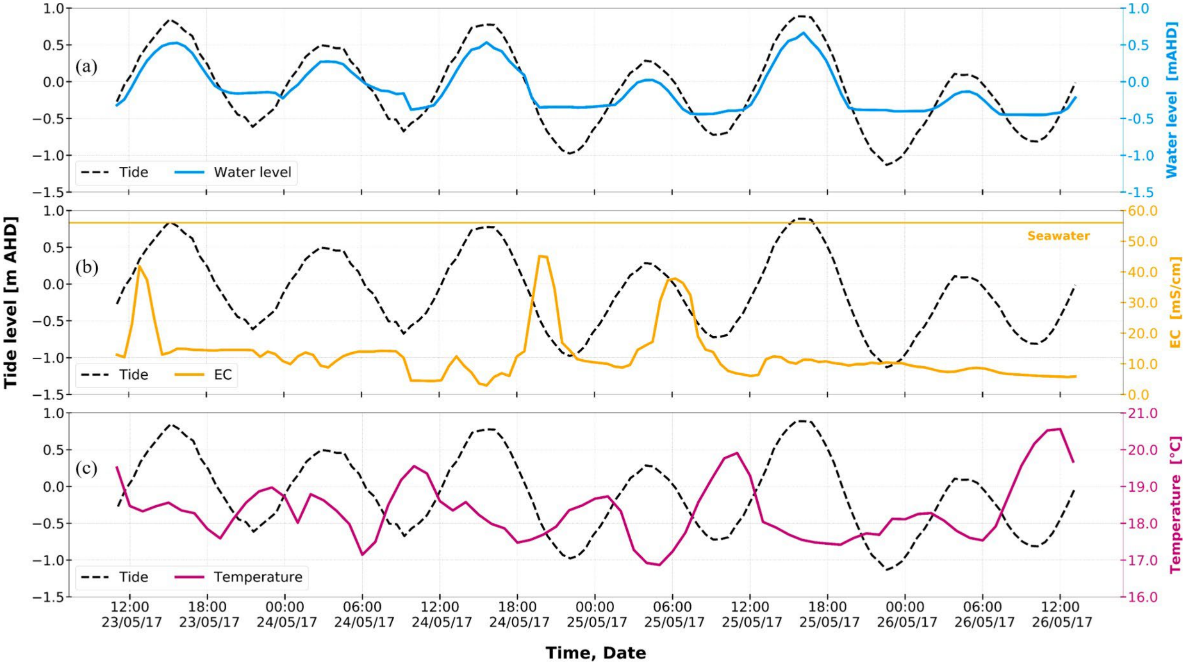

Fig. 10. Temporal variations of (a) water levels, (b) EC and (c) temperature at Spring D and ocean tide (dashed line) during 23–26 May 2017.

Discussion

1.6. *Spring and sand boils observations*

Results from the intertidal observations undertaken by this study during the three field campaigns (May 2017, Nov 2019 and Sept 2020), demonstrated the seasonal variability of the surface expression of the Sellicks Beach springs. From visual observations, the largest spring (Spring F; Fig. 1), with an approximate diameter of 0.50 m, was identified in the late spring campaign (Nov 2019). The diameter of the sand boils within Spring F were identified as the largest throughout this study (~0.1 m). In the winter campaign (May 2017) Spring A was identified at night with the TIR camera and had an approximate diameter of 0.30 m. However, the diameter of the sand boils within Spring A were significantly smaller (~0.01 m) compared to Spring F. Given the close proximity between the locations of Springs A and F (~1.5 m; Fig. 4), the continual changes in the geomorphology of the beach and the sand deposition, these two springs are considered to be the same spring. Nevertheless, the internal mechanisms that control the surface characteristics of the sand boils (e.g., sand boil diameter) within the springs should be considered in future studies.

At Sellicks Beach, previous studies have identified that the PWF cliffs and platforms have experienced significant erosion (May and Bour- man,1984; Bourman et al., 2016). Particularly, Cann et al. (2014) con- ducted field observations at Sellicks Beach for over forty years and described the erosion and distribution of beach sediments at Sellicks Beach. They attributed the origin and transport of the gravels, located at the high-tide level of the beach, to coastal and rainfall erosion of the alluvial fan sediments and the PWF cliffs (Fig. 3). They concluded that sediment transport along Sellicks Beach is predominantly influenced by seasonal changes. Specifically, longshore sediment transport occurs during wintertime when wave energy is high. These seasonal erosion and sediment transport mechanisms are likely to influence the surface expression of the intertidal springs. For example, the seasonal variation of sand thickness that overlays the PWF rocks can provide distinctive preferential flow paths and may be a controlling factor of the temporal changes of the location and occurrence of the springs and sand boils.

1.1. *Structural controls on spring discharge*

Previous studies that focused on groundwater discharge to the sea from the Willunga Basin (Martin, 1998; Lamontagne et al., 2008) suggested diffuse discharge along the coastline. However, this study demonstrated that discrete discharge from the basin can also occur as intertidal springs. The reason for the occurrence of this point discharge seems to be structural and linked to the faults and fractures identified in the area, associated with neotectonic activity (Jayawardena 2013; Lubiniecki et al. 2019). The nearby outcropping Willunga Fault is a clear example of the structural complexity at Sellicks Beach, where additional active faults, deformation bands, and land slumping have been identified in the Port Willunga Formation cliffs (Preiss, 2019) and platforms. Evidence documented by Reed (1982) of the faults at the top of the PWF cliffs (Fig. 2), approximately 200 m from the study site, brings to mind the possibility that this set of faults can extend towards the ocean and could have a greater influence in the creation of the preferential flow paths that control the intertidal seeps. Further geophysical investigations can help in the mapping and detection of the faults within the intertidal zone and determine their extent towards the ocean.

1.2. *EM geophysics*

The EM geophysical survey provided a fast, non-invasive opportunity to map the intertidal zone. This technique was able to identify a high resistivity anomaly (5 ohm.m) that correlated with the location of the visible surface expression of Spring D. Compared to the areas where no spring was identified, lower resistivity values (<1.5 ohm.m) were detected by the CMD-Explorer and correlated to the presence of seawater saturated sand.

Despite the valuable results obtained, this technique has not been widely explored in highly conductive environments, such as the inter- tidal zone. As suggested by Reid and Howlett (2001), in highly conductive environments (<10 ohm.m) the depth of investigation is reduced, and the measured conductivity tends to underestimate real conductivity values. Paepen et al., (2020) indicated that this limitation is the reason that this technique has not been extensively explored in intertidal environments. However, this study has shown that in combi- nation with other methods, (e.g., TIR imaging) EM geophysical techniques can provide valuable information to describe the spatial extent and geometry of intertidal springs.

1.1. *EC, pH and stable isotopes of water*

Intertidal spring δ^{18}O and δ^{2}H composition is characterised by a considerable tidal and seasonal variability. Isotope enrichment was observed at high tide, where seawater inundates the springs. Addition- ally, winter samples were more enriched, compared to early-late spring values. Water mixing calculations using average δ^{18}O, δ^{2}H and EC data also showed seasonal variability. In the winter campaign (May 2017) at low tide periods, the average groundwater contribution to spring discharge was 69 %, while during high tide periods this decreased to 15%. For the late and early spring campaigns (Nov 2019 and September 2020, respectively), the average groundwater contribution to the springs at low tide was 87 % and 93 %, respectively. These seasonal comparisons correlate to previous studies of the area that indicate that seasonal changes of seawater levels and wave energy can considerably influence the water composition of intertidal springs (Short et al., 2014; Cann et al., 2014).

pH values also showed seasonal variations; during the spring campaign, the average pH was 7.4, while for the late and early spring campaigns the pH ranged between 6.8 and 6.9.

1.1. *Time series analysis*

The response observed in the water level and tidal data can be attributed to filtering processes occurring at the beach (Lanyon et al., 1982), something which has previously been observed in estuarine settings (e.g., Carey et al., 2009). In Fig. 10(a), the flat sections in the water levels of Spring D are indicative of seepage face formation at the beach, whereby the head at the point of discharge levels out at an elevation close to the land surface. Similar patterns have been observed in other studies of intertidal zones (e.g., Turner, 1993; Li et al., 2006; Carey et al., 2009). At low tide periods, spring water discharge occurs in the intertidal zone because the water levels in Spring D remain above seawater levels. Meanwhile, at high tide periods, tidal and wave action drive seawater to the intertidal zone, where it infiltrates and mixes with groundwater, causing seawater recirculation (Robinson et al., 2007; Heiss and Michael, 2014).

Conclusions

This study aimed to characterise intertidal springs identified as groupings of closely spaced sand boils, located in Sellicks Beach, South Australia, to better understand groundwater-surface water interactions in coastal environments. The combined use of EM geophysics and handheld TIR imagery proved to be a reliable, rapid and non-invasive methodology to locate and describe the surface expressions of the intertidal springs and their spatial distribution in the subsurface $\delta^{18}O$ and $\delta^{2}H$ data indicated that isotope composition of the intertidal springs is characterised by a significant seasonal variability (winter and spring), and isotope enrichment due to groundwater-seawater mixing processes and tidal variations. We may conclude that water from the springs is controlled by a mixture of two main end members, fresh regional groundwater and seawater. With different proportions of groundwater in the mixture, i.e. up to 100 % at low tide in early spring 2020 and down to 14 % at low tide in early winter 2017. However, our results cannot accurately determine which aquifer is feeding the springs or if it is mainly a combined contribution due to the complex multi-aquifer setting. Temperature time series measurements and water levels at spring D showed variations strongly driven by the tidal cycle. Additional handheld temperature measurements and TIR imagery revealed clear contrasts between seawater, spring water and the surrounding saturated sediments.

The presence of intertidal springs in Sellicks Beach is likely a result of the structurally complex nature of the area. The cliffs and outcropping intertidal platforms display faults and fractures that provide preferential flow paths for groundwater flow. A more comprehensive characterisation of the fractured rock system underneath the beach sand would enhance our current understanding of the source and structural, geological controls of the springs. Future work should develop a temporal assessment of the springs to better understand their seasonal variability, including spring heads and discharge. Also, sediment transport analysis would be greatly beneficial to characterise and understand the release of water and sediment from intertidal sand boils within springs.

Declaration of Competing Interest

The authors declare that they have no known competing financial interests or personal relationships that could have appeared to influence the work reported in this paper.

Data availability

Data will be made available on request.

Acknowledgments

Adrian Werner is the recipient of an Australian Research Council Future Fellowship (project number FT150100403). The authors would like to thank the two anonymous reviewers who reviewed this manuscript.

References

Adelaide and Mount Lofty Ranges NRM Board, 2007. Water Allocation Plan for the McLaren Vale Prescribed Wells Area. Adelaide.

Aggarwal, P., Fröhlich, K., Kulkarni, K.M., 2009. Environmental Isotopes In Groundwater

Studies, in: Silveira, L., Usunoff, E.J. (Eds.), Groundwater. EOLSS Publications, pp. 69–92.

Auken, E., Christiansen, A.V., Kirkegaard, C., Fiandaca, G., Schamper, C., Behroozmand, A.A., Binley, A., Nielsen, E., Effersø, F., Christensen, N.B., Sørensen, K., Foged, N., Vignoli, G., 2015. An Overview Of A Highly Versatile Forward And Stable Inverse Algorithm For Airborne, Ground-Based And Borehole

Aydin, A., 1978. Small Faults Formed As Deformation Bands In Sandstone, in: Byerlee, J. D., Wyss, M. (Eds.), Rock Friction And Earthquake Prediction. Birkhäuser Basel, pp. 913–930. 10.1007/978-3-0348-7182-2_22.

Bardsley, D.K., Palazzo, E., Wiseman, N.D., Stringer, R., 2017. The roles of agricultural biodiversity in the McLaren Vale landscape. Department of Environment, Water and Natural Resources (SA). APO-103711.

Beck, A.J., Tsukamoto, Y., Tovar-Sanchez, A., Huerta-Diaz, M., Bokuniewicz, H.J., Sañudo-Wilhelmy, S.A., 2007. Importance Of Geochemical Transformations In Determining Submarine Groundwater Discharge-Derived Trace Metal And Nutrient Fluxes. Appl. Geochemistry 22, 477–490. https://doi.org/10.1016/j. apgeochem.2006.10.005.

Benkendorff, K., Fairweather, P., Dittmann, S., 2008. Intertidal Ecosystems. In: Shepherd, S., Bryars, S., Kirkegaard, I., Harbison, P., Jennings, J.T. (Eds.), Natural HiStory Of The Gulf St Vincent. Royal Society Of S.A, Adelaide, Australia.

Bokuniewicz, H., Taniguchi, M., Ishitoibi, T., Charette, M., Allen, M., Kontar, E.A., 2008. Direct Measurements Of Submarine Groundwater Discharge (SGD) Over A Fractured Rock Aquifer In Flamengo Bay Brazil. Estuar. Coast. Shelf Sci. 76, 466–472. https:// doi.org/10.1016/j.ecss.2007.07.047.

Bourman, R.P., Murray-Wallace, C.V., Harvey, N., 2016. Coastal Landscapes of South Australia. University of Adelaide Press. 10.20851/coast-sa.

Bureau of Meteorology, 2017. South Australian Observations. http://www.bom.gov.au/ climate/current/annual/sa/archive/2017 (accessed 14.07.22).

Bureau of Meteorology, 2020. South Australian Observations. http://www.bom.gov.au/ sa/observations (accessed 21.09.20).

Burnett, W.C., Bokuniewicz, H., Huettel, M., Moore, W.S., Taniguchi, M., 2003. Groundwater And Pore Water Inputs To The Coastal Zone. Biogeochemistry 66, 3–33. https://doi.org/10.1023/b:Biog.0000006066.21240.53.

Burnett, W.C., Aggarwal, P.K., Aureli, A., Bokuniewicz, H., Cable, J.E., Charette, M.A., Kontar, E., Krupa, S., Kulkarni, K.M., Loveless, A., Moore, W.S., Oberdorfer, J.A., Oliveira, J., Ozyurt, N., Povinec, P., Privitera, A.M.G., Rajar, R., Ramessur, R.T., Scholten, J., Stieglitz, T., Taniguchi, M., Turner, J.V., 2006. Quantifying Submarine Groundwater Discharge In The

Coastal Zone Via Multiple Methods. Sci. Total Environ. 367, 498–543. https://doi.org/10.1016/j.scitotenv.2006.05.009.

Burnett, W.C., Dulaiova, H., 2006. Radon As A Tracer Of Submarine Groundwater Discharge Into A Boat Basin In Donnalucata. Sicily. Cont. Shelf Res. 26, 862–873. https://doi.org/10.1016/j.csr.2005.12.003.

Cable, J.E., Burnett, W.C., Chanton, J.P., Weatherly, G.L., 1996. Estimating Groundwater Discharge Into The Northeastern Gulf Of Mexico Using Radon-222. Earth Planet. Sci. Lett. 144, 591–604. https://doi.org/10.1016/S0012-821X(96)00173-2.

Cann, J.H., Lower, C.S., Jago, J.B., 2014. Provenance And Sediment Characteristics Of Contemporary Gravel Deposits At Sellicks Beach, Eastern Shore Of Gulf St Vincent. South Australia. Aust. J. Earth Sci. 61, 819–836. https://doi.org/10.1080/

Carey, H., Lenkopane, M.K., Werner, A.D., Li, L., Lockington, D.A., 2009. Tidal controls on coastal groundwater conditions: field investigation of a macrotidal system. Aust. J. Earth Sci. 56, 1165–1179. https://doi.org/10.1080/08120090903246246. Cave, R.R., Henry, T., 2011. Intertidal And Submarine Groundwater Discharge On The West Coast Of Ireland. Estuar. Coast. Shelf Sci. 92, 415–423. https://doi.org/ 10.1016/j.ecss.2011.01.019.

Charette, M.A., Buesseler, K.O., Andrews, J.E., 2001. Utility Of Radium Isotopes For Evaluating The Input And Transport Of Groundwater-Derived Nitrogen To A Cape Cod Estuary. Limnol. Oceanogr. 46, 465–470. https://doi.org/10.4319/ lo.2001.46.2.0465.

Charette, M.A., Sholkovitz, E.R., 2006. Trace Element Cycling In A Subterranean Estuary: Part 2. Geochemistry Of The Pore Water. Geochim. Cosmochim. Acta 70, 811–826. https://doi.org/10.1016/j.gca.2005.10.019.

Christiansen, A.V., Pedersen, J.B., Auken, E., Søe, N.E., Holst, M.K., Kristiansen, S.M., 2016. Improved Geoarchaeological Mapping With Electromagnetic Induction Instruments From Dedicated Processing And Inversion. Remote Sens. 8, 1022. https://doi.org/10.3390/rs8121022.

Craig, H., 1961. Isotopic Variations in Meteoric Waters. Science (80-.). 133, 1702–1703. https://doi.org/10.1126/science.133.3465.1702.

Dale, R.K., Miller, D.C., 2007. Spatial And Temporal Patterns Of Salinity And Temperature At An Intertidal Groundwater Seep. Estuar. Coast. Shelf Sci. 72, 283–298. https://doi.org/10.1016/j.ecss.2006.10.024.

Danielescu, S., MacQuarrie, K.T.B., Faux, R.N., 2009. The integration of thermal infrared imaging, discharge measurements and numerical simulation to quantify the relative contributions of freshwater inflows to small estuaries in Atlantic Canada. Hydrol. Process. 23, 2847–2859. https://doi.org/10.1002/hyp.7383.

de Louw, P.G.B., Oude Essink, G.H.P., Stuyfzand, P.J., van der Zee, S.E.A.T.M., 2010. Upward Groundwater Flow In Boils As The Dominant Mechanism Of Salinization In Deep Polders, The Netherlands. J. Hydrol. 394, 494–506. https://doi.org/10.1016/j. jhydrol.2010.10.009.

DEW, 2021. McLaren Vale Prescribed Wells Area 2019–20 water resources assessment.DEW Technical Note 2021/12. Government of South Australia, Department for Environment and Water.

Duarte, T.K., Hemond, H.F., Frankel, D., Frankel, S., 2006. Assessment Of Submarine Groundwater Discharge By Handheld Aerial Infrared Imagery: Case Study Of Kaloko Fishpond And Bay. Hawai'i. Limnol. Oceanogr. Methods 4, 227–236. https://doi. org/10.4319/lom.2006.4.227.

Dyson, I.A., 1998. Estuarine Facies Of The North Maslin Sand And South Maslin Sand. Maslin Beach. MESA J. 11, 42–46.

El Hage, M., Robinson, C.A., El-Baz, F., Shaban, A., 2020. Fracture-Controlled Groundwater Seeps Into The Mediterranean Sea Along The Coast Of Lebanon. Arab. J. Geosci. 13, 52

Fairburn, B., 1998. The Willunga Embayment — An Stratigraphic Revision. MESA J. 11, 35–41.

Harrington, N., Cook, P.G., 2012. Willunga Research Update, October 2012. Adelaide.

Heiss, J.W., Michael, H.A., 2014. Saltwater-freshwater mixing dynamics in a sandy beach aquifer over tidal, spring-neap, and seasonal cycles. Water Resour. Res. 50,6747–6766. https://doi.org/10.1002/2014WR015574.

Jayawardena, C.L., 2013. Characteristics Of Neotectonic Faulting In The Mount Lofty And Flinders Ranges, South Australia. Sch. Earth Environ. Sci. University of Wollongong, Wollongong, New South Wales. ro.uow.edu.au/theses/4093/.

Johannes, R.E., 1980. The Ecological Significance Of The Submarine Discharge Of Groundwater. Mar. Ecol. Prog. Ser. 3, 365–373. https://doi.org/10.3354/ meps003365.

Knowles, I., Teubner, M., Yan, A., Rasser, P., Lee, J.W., 2007. Inverse groundwater modelling in the Willunga Basin, South Australia. Hydrogeol. J. 15, 1107–1118. https://doi.org/10.1007/s10040-007-0189-6.

Lamontagne, S., La Salle, C.L.G., Hancock, G.J., Webster, I.T., Simmons, C.T., Love, A.J., James-Smith, J., Smith, A.J., Ka¨mpf, J., Fallowfield, H.J., 2008. Radium And Radon Radioisotopes In Regional Groundwater, Intertidal Groundwater, And Seawater In The Adelaide Coastal Waters Study Area: Implications For The Evaluation Of Submarine Groundwater Discharge. Mar. Chem. 109, 318–336. https://doi.org/ 10.1016/j.marchem.2007.08.010.

Lanyon, J.A., Eliot, I.G., Clarke, D.J., 1982. Groundwater-level variation during semidiurnal spring tidal cycles on a sandy beach. Mar. Freshw. Res. 33, 377–400. https://doi.org/10.1071/MF9820377.

Lee, Y.W., Hwang, D.W., Kim, G., Lee, W.C., Oh, H.T., 2009. Nutrient Inputs From Submarine Groundwater Discharge (SGD) In Masan Bay, An Embayment Surrounded By Heavily Industrialized Cities. Korea. Sci. Total Environ. 407, 3181–3188. https:// doi.org/10.1016/j.scitotenv.2008.04.013.

Levi, E., Goldman, M., Hadad, A., Gvirtzman, H., 2008. Spatial Delineation Of Groundwater Salinity Using Deep Time Domain Electromagnetic Geophysical Measurements: A Feasibility Study. Water Resour. Res. 44./10.1029/ 2007WR006459.

Li, L., Barry, D.A., 2000. Wave-Induced Beach Groundwater Flow. Adv. Water Resour.
23, 325–337. https://doi.org/10.1016/S0309-1708(99)00032-9.

Li, L., Horn, D.P., Baird, A.J., 2006. Tide-Induced Variations in Surface Temperature and Water-Table Depth in the Intertidal Zone of a Sandy Beach. J. Coast. Res. 22, 1370–1381.

Liu, Y., Jiao, J., Cheng, H., 2018. Tracing Submarine Groundwater Discharge Flux In Tolo Harbor, Hong Kong (China). Hydrogeol. J. 26, 1857–1873. https://doi.org/ 10.1007/s10040-018-1736-z.

Lubiniecki, D.C., White, S.R.S., King, R.C., Holford, S.P., Bunch, M.A., Hill, S.M., 2019. Structural Evolution Of Carbonate-Hosted Cataclastic Bands Adjacent To A Major Neotectonic Fault, Sellicks Beach, South Australia. J. Struct. Geol. 126, 11–24. https://doi.org/10.1016/j.jsg.2019.05.004.

Martin, R.R., 1998. Willunga Basin – Status Of Groundwater Resources 1998. Primary Industries And Resources South Australia Report Book 98/28, Adelaide.

May, R.I., Bourman, R.P., 1984. Coastal Landslumping In Pleistocene Sediments At Sellicks Beach. South Australia. Trans. R. Soc, South Aust.

McAllister, S.M., Barnett, J.M., Heiss, J.W., Findlay, A.J., MacDonald, D.J., Dow, C.L., Luther III, G.W., Michael, H.A., Chan, C.S., 2015. Dynamic Hydrologic And Biogeochemical Processes Drive Microbially Enhanced Iron And Sulfur Cycling Within The Intertidal Mixing Zone Of A Beach Aquifer. Limnol. Oceanogr. 60, 329–345. https://doi.org/10.1002/lno.10029.

McNeill, J.D., 1980. Electromagnetic Terrain Conductivity Measurement At Low Induction Numbers Tech. Note TN-6. Geonics Limited, Ontario, Canada.

Miller, D.C., Ullman, W.J., 2004. Ecological Consequences Of Ground Water Discharge To Delaware Bay, United States. Groundwater 42, 959–970. https://doi.org/ 10.1111/j.1745-6584.2004.tb02635.x.

Moore, W.S., 1999. The Subterranean Estuary: A Reaction Zone Of Ground Water And Sea Water. Mar. Chem. 65, 111–125. https://doi.org/10.1016/S0304-4203(99) 00014-6.

Moore, W.S., 2010. The Effect Of Submarine Groundwater Discharge On The Ocean. Ann. Rev. Mar. Sci. 2, 59–88. https://doi.org/10.1146/annurev-marine-120308-081019.

Mulligan, A.E., Charette, M.A., 2006. Intercomparison Of Submarine Groundwater Discharge Estimates From A Sandy Unconfined Aquifer. J. Hydrol. 327, 411–425. https://doi.org/10.1016/j.jhydrol.2005.11.056.

NCRIS Groundwater Database, 2022. http://groundwater.anu.edu.au/fieldsite/willunga (accessed 22.07.22).

Paepen, M., Hanssens, D., De Smedt, P., Walraevens, K., Hermans, T., 2020. Combining Resistivity And Frequency Domain Electromagnetic Methods To Investigate Submarine Groundwater Discharge In The Littoral Zone. Hydrol. earth Syst. Sci. 24, 3539–3555. https://doi.org/10.5194/hess-24-3539-2020.

Picarro, 2020. L2130-i Isotope and Gas Concentration Analyzer. https://www.picarro.co m/products/l2130i_isotope_and_gas_concentration_analyzer (accessed 12.1.21).

Post, V.E.A., Banks, E., Brunke, M., 2018. Groundwater flow in the transition zone between freshwater and saltwater: a field-based study and analysis of measurement errors. Hydrogeol. J. 26, 1821–1838. https://doi.org/10.1007/s10040-018-1725-2.

Post, V.E.A., Salmon, U., van Duivenvoorde, W., 2020. The Intertidal Springs Near The Vergulde Draak 1656 Wreck Site, Western Australia: Hydrogeological Characteristics And Archaeological Significance. Hydrogeol. J. 28, 2071–2084. https://doi.org/ 10.1007/s10040-020-02173-3.

Povinec, P.P., Aggarwal, P.K., Aureli, A., Burnett, W.C., Kontar, E.A., Kulkarni, K.M., Moore, W.S., Rajar, R., Taniguchi, M., Comanducci, J.F., Cusimano, G., Dulaiova, H., Gatto, L., Groening, M., Hauser, S., Levy-Palomo, I., Oregioni, B., Ozorovich, Y.R., Privitera, A.M.G., Schiavo, M.A., 2006. Characterisation Of Submarine Groundwater Discharge Offshore South-Eastern Sicily. J. Environ. Radioact. 89, 81–101. https:// doi.org/10.1016/j.jenvrad.2006.03.008.

Povinec, P., Burnett, W., Beck, A., 2012. Isotopic, geophysical and biogeochemical investigation of submarine groundwater discharge: IAEA-UNESCO intercomparison exercise at Mauritius Island. J. Environ. Radioactiv. 104, 24–45. https://doi.org/ 10.1016/j.jenvrad.2011.09.009.

Preiss, W.V., 2019. The tectonic history of Adelaide's scarp-forming faults. Aust. J. Earth Sci. 66, 305–365.

https://doi.org/10.1080/08120099.2018.1546228.

Reed, G.D., 1982. Geophysical Investigation Of The Willunga Fault Zone. Department Of Mines And Energy, Adelaide, South Australia.

Reid, J.E., Howlett, A., 2001. Application of the EM-31 Terrain Conductivity Meter in Highly-Conductive Regimes. Explor. Geophys. 32, 219–224. https://doi.org/ 10.1071/EG01219.

Robinson, C., Li, L., Prommer, H., 2007. Tide-Induced Recirculation Across The Aquifer- Ocean Interface. Water Resour. Res. 43 https://doi.org/10.1029/2006wr005679.

Rodellas, V., Garcia-Orellana, J., Tovar-S´anchez, A., Basterretxea, G., Lo´pez-Garcia, J.M., Sanchez-Quiles, D., Garcia-Solsona, E., Masqu´e, P., 2014. Submarine Groundwater Discharge As A Source Of Nutrients And Trace Metals In A Mediterranean Bay (Palma Beach, Balearic Islands). Mar. Chem. 160, 56–66. https://doi.org/10.1016/j. marchem.2014.01.007.

Ro¨per, T., Greskowiak, J., Massmann, G., 2014. Detecting Small Groundwater DischargeSprings Using Handheld Thermal Infrared Imagery. Ground Water 52, 936–942. https://doi.org/10.1111/gwat.12145.

Schneider, J.C., Kruse, S.E., 2003. A Comparison Of Controls On Freshwater Lens Morphology Of Small Carbonate And Siliciclastic Islands: Examples From Barrier Islands In Florida. USA. J. Hydrol. 284, 253–269. https://doi.org/10.1016/j. jhydrol.2003.08.002.

Shanafield, M., Gutierrez-Jurado, K., White, N., Hatch, M., Keane, R., 2020. Catchment-Scale Characterization Of Intermittent Stream Infiltration; A Geophysics Approach. J. Geophys. Res. Earth Surf. 125, e2019JF005330. 10.1029/2019jf005330. Short, M.A., Lamontagne, S., Cook, P.G., Cranswick, R., 2014. Characterising The Distribution Of Near-Shore Submarine Groundwater Discharge Along A Coastline Using 222Rn And Electrical Conductivity. Aust. J. Earth Sci. 61, 319–331. https:// doi.org/10.1080/08120099.2014.884018.

Smith, N.P., 1986. The Rise And Fall Of The Estuarine Intertidal Zone. Estuaries 9, 95–101. https://doi.org/10.2307/1351941.

Stieglitz, T., 2005. Submarine Groundwater Discharge Into The Near-Shore Zone Of The Great Barrier Reef. Australia. Mar. Pollut. Bull. 51, 51–59. https://doi.org/10.1016/ j.marpolbul.2004.10.055.

Swarzenski, P.W., Izbicki, J.A., 2009. Coastal Groundwater Dynamics Off Santa Barbara, California: Combining Geochemical Tracers, Electromagnetic Seepmeters, And Electrical Resistivity. Estuar. Coast. Shelf Sci. 83, 77–89. https://doi.org/10.1016/j. ecss.2009.03.027.

Taboro˘si, D., Jenson, J.W., Mylroie, J.E., 2013. Field Observations Of Coastal Discharge From An Uplifted Carbonate Island Aquifer, Northern Guam, Mariana Islands: A Descriptive Geomorphic And Hydrogeologic Perspective. J. Coast. Res. 29, 926. https://doi.org/10.2112/JCOASTRES-D-12-00054.1.

Tait, D.R., Santos, I.R., Erler, D.V., Befus, K.M., Cardenas, M.B., Eyre, B.D., 2013. Estimating Submarine Groundwater Discharge In A South Pacific Coral Reef Lagoon Using Different Radioisotope And Geophysical Approaches. Mar. Chem. 156, 49–60. https://doi.org/10.1016/j.marchem.2013.03.004.

Taniguchi, M., Burnett, W.C., Cable, J.E., Turner, J.V., 2002. Investigation Of Submarine Groundwater Discharge. Hydrol. Process. 16, 2115–2129. https://doi.org/10.1002/ hyp.1145.

Taniguchi, M., Dulai, H., Burnett, K.M., Santos, I.R., Sugimoto, R., Stieglitz, T., Kim, G., Moosdorf, N., Burnett, W.C., 2019. Submarine Groundwater Discharge: Updates On Its Measurement Techniques, Geophysical Drivers, Magnitudes. And Effects. Front. Environ. Sci. 7 https://doi.org/10.3389/fenvs.2019.00141.

Terwey, J.L., 1984. Isotopes In Groundwater Hydrology, In: Proceedings Of The Harare Symposium: Challenges In African Hydrology And Water Resources. IAHS, Netherlands, pp. 155–160.

Tokarev, V., 2005. Neotectonics Of The Mount Lofty Ranges (South Australia). University of Adelaide, Adelaide, South Australia, Sch. Earth Environ. Sci.

Turner, I., 1993. Water table outcropping on macro-tidal beaches: A simulation model. Mar. Geol. 115, 227–238. https://doi.org/10.1016/0025-3227(93)90052-W.

Waska, H., Kim, G., 2011. Submarine Groundwater Discharge (SGD) As A Main Nutrient Source For Benthic And Water-Column Primary Production In A Large Intertidal Environment Of The Yellow Sea. J. Sea Res. 65, 103–113. https://doi.org/10.1016/j. seares.2010.08.001.

Werner, A.D., Jazayeri, A., Ramirez-Lagunas, M., 2020. Sediment Mobilisation And Release Through Groundwater Discharge To The Land Surface: Review And Theoretical Development. Sci. Total Environ. 714, 136757 https://doi.org/10.1016/ j.scitotenv.2020.136757.

Xin, P., Robinson, C., Li, L., Barry, D.A., Bakhtyar, R., 2010. Effects Of Wave Forcing On A Subterranean Estuary. Water Resour. Res. 46 https://doi.org/10.1029/ 2010wr009632.

Yechieli, Y., Kafri, U., Goldman, M., Voss, C., 2001. Factors Controlling The Configuration Of The Fresh-Saline Water Interface In The Dead Sea Coastal Aquifers: Synthesis Of TDEM Surveys And Numerical Groundwater Modeling. Hydrogeo77. https://doi.org/10.1007/s100400100146.

Appendix 2

Co-author publication

Science of the Total Environment 714 (2020) 136757

Contents lists available at ScienceDirect

Science of the Total Environment

Review

Sediment mobilisation and release through groundwater discharge to the land surface: Review and theoretical development

Adrian D. Werner [a,b], Amir Jazayeri [a,b,*], Marianna Ramirez-Lagunas [a,b]

[a] National Centre for Groundwater Research and Training, Flinders University, GPO Box 2100, Adelaide, SA 5001, Australia

[b] College of Science and Engineering, Flinders University, GPO Box 2100, Adelaide, SA 5001, Australia

HIGHLIGHTS

- Forms of sediment ejection by groundwater discharge are reviewed and categorized.
- New, simple formula proposed to estimate hydraulic gradient causing grain movement.
- Reasonable agreement between new formula and existing data obtained for suffusion.
- Laboratory sand boils require larger hydraulic gradients compared to new theory.
- Knowledge gaps for sediment ejection through groundwater discharge summarized

ARTICLE INFO

Article history:

Received 14 October 2019

Received in revised form 15 January 2020

Accepted 15 January 2020

Available online 18 January 2020

Editor: Filip M.G. Tack

Keywords:

Sand boil

Groundwater discharge

Sediment transport

Stokes' law

Piping Erosion

GRAPHICAL ABSTRACT

Conceptual models, theory, and experimental data relating to the release of sediments under the effects of groundwater discharge are critically reviewed and revisited. Groundwater flow simulation of simple conceptual models highlight key characteristics leading to heave, pipe formation and hydraulic gradient propagation that leads to subsurface sediment transport.

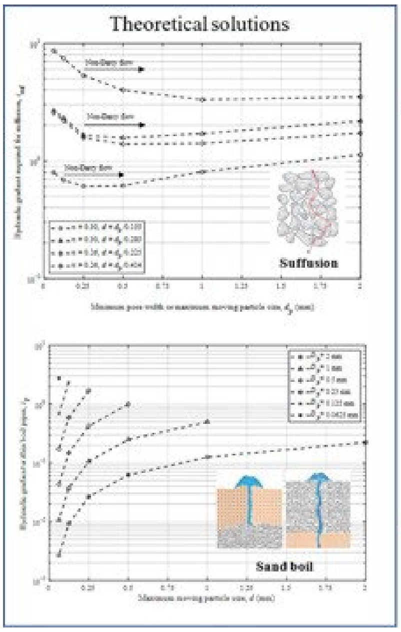

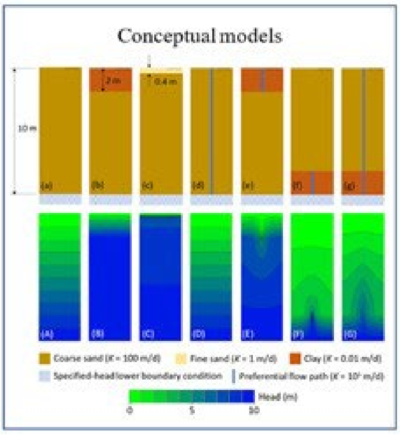

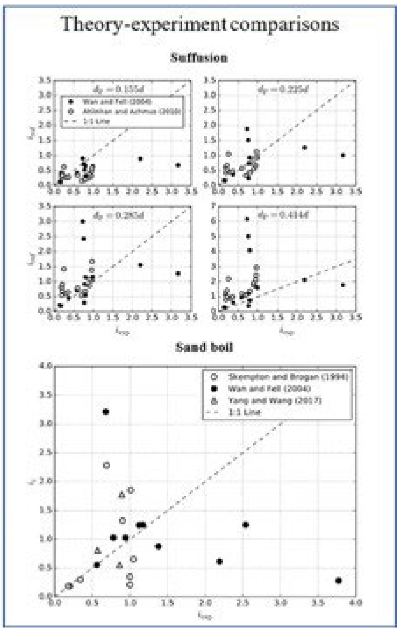

ABSTRACT

The discharge of groundwater to the land surface and to lakes and streams may express subsurface particles. This may lead to preferential pathways and increased fluxes of groundwater, sediment and contaminants, and modified subsurface structures. The current review attempts to describe and categorise the various forms through which sediment may be liberated in areas of groundwater discharge. Forces acting on subsurface particles in areas of groundwater discharge include seepage (drag), buoyancy and particle weight, amongst other, more complex forces. Equations for these can be combined to create formulae for approximating the conditions under which groundwater discharge will transport particles to the surface. Two forms of subsurface sediment transport are considered: (1) flow through an immobile granular matrix (*suffusion* and *suffosion*), and (2) flow through preferential pathways (i.e., often treated as pipes). Suffusion involves sediment movement that does not impact the soil's stability, whereas suffosion creates changes to soil stability and, consequently, soil volume. Preferential flow may arise from cracks in cohesive materials or through localised fluidization of non-cohesive soils, leading in some situations to *sand boils*. Guidance is presented on the minimum theoretical hydraulic gradient required for grains of various sizes to start to rise. New simple formulae are developed that build on existing theory, and these are compared to previous laboratory data, showing that suffusion is more or less predictable using the new simple method. However, experimental sand boils require larger hydraulic gradients compared to theory. The current analysis summarises the state of knowledge and persistent knowledge gaps associated with sediment ejection through groundwater discharge, which we expect has wide-ranging applications in terms of sediment transport in coastal regions and to surface water bodies, and where strong groundwater discharge is known to occur.

---

* Corresponding author.

E-mail addresses: adrian.werner@flinders.edu.au (A.D. Werner), amir.jazayeri@flinders.edu.au (A. Jazayeri), marianna.ramirez@flinders.edu.au (M. Ramirez-Lagunas).

Contents

1. Introduction

The expression of groundwater at the land surface is a common occurrence. Groundwater discharge (or *seepage flow*) is critical to the survival of ecosystems in water-limited regions and provides significant fluxes of dissolved chemicals to surface water bodies, including the ocean (e.g., Moore, 2010). In some situations, seepage flows may also entrain subsurface particles and transport these to the surface and/or surface water bodies.

The transport of particles by groundwater has received considerable attention in the field of dam safety because the failure of earth dams may initially present as ejected subsurface particles in groundwater dis- charge zones (Van Beek et al., 2013). Particle displacement below dam structures may be initiated where the friction forces arising from flowing groundwater are sufficient to rotate, dislodge and mobilise sediment particles (e.g., Sellmeijer, 1988; Van Beek et al., 2013). *Piping* was described by Hagerty (1991) as the removal of particles by seepage out- flow that forms cylindrical conduits commonly conceptualised as pipes. If seepage exfiltration occurs in a larger area, the term *sapping* can be used (Jones, 1981; Hagerty, 1991). Sapping has the same characteristics as piping in that both are particle removal mechanisms resulting in pipe formation, except that with sapping larger lenticular cavities can also appear (Hagerty, 1992). Additionally, the term *jugging* has also been used to describe vertical erosion tunnels (Decker and Dunnigan, 1977). Richards and Reddy (2007) acknowledged that jugging in dispersive soils is caused by rainfall erosion and might lead to dam failures that resemble erosion originated by animals or tree roots.

Where sediment is subsequently transported downstream of an engineering structure, hollow spaces in or underneath dam structures can grow in the opposite direction of the flow, potentially leading to *piping failure* (Van Beek et al., 2013), including such catastrophic events as the collapse of the Teton Dam (USA) in 1976 (Jones, 1981; Richards and Reddy, 2007). The various forms of sediment movement in the vicinity of engineering structures is termed *internal erosion* by FEMA (2015). *Contact erosion* and *concentrated leak erosion* are also internal erosion mechanisms. The former can occur where coarse and fine soils are in contact and there is a flow parallel to the contact, leading to erosion of the finer soil (Bonelli and Nicot, 2013). Concentrated leak erosion takes place through cracks originated by hydraulic fractures due to, for example, differential settlement during construction of a dam or levee (Bonelli et al., 2013). Another phenomenon commonly related to subsurface erosion is the *sand boil*, which may appear, often in groups, in areas of groundwater discharge. These typically appear as small, volcano-shaped vents through which sediment is released, and have been observed downstream of water-retaining structures (e.g., dams, dikes, etc.; TACFD, 1999). Artificial sand boils have been created in laboratory experiments (Miesel, 1978; Muller-Kirchenbauer, 1978) and in field-scale experiments (Silvis, 1991; Van Beek et al., 2011) to study the erosion of levees.

Sediment may also be liberated from the subsurface in the absence of surface water impoundments. For example, De Louw et al. (2010, 2013) observed preferential groundwater flow in the form of localised expressions of upwelling groundwater (i.e., *boils*) or as larger vents with both water and sediment discharge (i.e., sand boils) in Dutch polders. They attributed these and similar features in other Dutch polders to the considerable groundwater hydraulic gradients that arise from the low land surface elevation, relative to sea level, of much of The Netherlands. De Louw et al. (2010, 2013) suggest that the boils and sand boils in Dutch polders arise after cohesive layers heave, leading to preferential pathways through which groundwater flows at high velocities. Sand boils were particularly evident beneath lower polders. Sand boils have also been observed in river embankments, for example, during floods in: the Rhine, Waal, IJssel and Maas Rivers (The Netherlands; Van Beek et al., 2013), the Yangtze and Nenjiang Rivers (China; Yao et al., 2009), and the Mississippi River (USA; Li et al., 1996; Mansur et al., 2000; Glynn and Kuszmaul, 2010).

The current review evaluates the liberation of subsurface particles two categories: (1) flow through immobile pore networks within a granular matrix, and (2) flow through preferential pathways. The latter may arise from cracks in cohesive materials, through localised fluidity of non-cohesive soils (i.e., in which gravity, buoyancy effects and drag from flowing groundwater control intergranular forces) or through pathways created from more natural processes such as desiccation cracking, root holes, rodent activity and anthropogenic causes. In (1), the particles transported through a pore network by groundwater flow must be small enough to pass through the intergranular spaces, and groundwater flow must be strong enough to erode particles and transport them upwards against the submerged gravitational force (i.e., sediment weight minus buoyancy) acting on each particle. In (2), hydraulic forces must be large enough to cause heave (i.e., uplift) of cohesive layers and/or sand fluidization, and to transport particles upwards against submerged gravitational forces. Fig. 1 provides a schematic illustration of conceptual models for the different forms of subsurface sediment transport that lead to the ejection of particles.

The theory developed in this research is an extension to previous studies of vertical sediment transport in the subsurface because we consider relationships between sediment particle characteristics and hydraulic forces for various forms of sediment transport through porous media. While prior studies mainly focus on specific conditions, the current research aims to review theoretical bases for estimating vertical particle displacement under various common mechanisms and situations.

1. Theory

1.1. Particle movement under vertical fluid flow

Here, we consider the forces acting on a single particle within a moving fluid body. A single particle in a stationary fluid will eventually descend at its terminal velocity (V_T), whereby the total resistance force or drag force (F_D) becomes equal to the difference between the particle's weight (W) and the buoyancy force (F_B) acting on it, as (Prandtl and Tietjens, 1934):

$$F_D = C_D A_P \frac{\rho_f V_T^2}{2} = W - F_B \tag{1}$$

where C_D is the drag coefficient, A_P is the projected area of the particle and ρ_f is the fluid density. C_D can be expressed as a function of Reynolds number (Re) and the shape of the particle (e.g., Madhav and Chhabra, 1995), where Re is given by:

$$Re = \frac{\rho_f U L}{\mu} \tag{2}$$

Here, U is the velocity (taken as the terminal velocity of the particle, v_T), L is the characteristic dimension (taken as the particle diameter, d)and μ is the dynamic viscosity of the fluid (approximately 10^{-3} Pa·s for freshwater). Alternative forms of Eq. (2) apply to different situations of subsurface sediment movement, as addressed in subsequent subsections. At small Re (b0.5), two-thirds of the total resistance to flow around spheres is due to shear (friction drag) and one-third is due to pressure (form drag) (Lamb, 1932). Stokes' law can be used to define C_D for Re b 0.5, e.g., for spheres (e.g., Clift et al., 1978):

$$C_D = \frac{24}{Re} \tag{3}$$

The corresponding Stokes' terminal velocity (V_{ST}) (i.e., for the submerged descent on a single particle) can be calculated by combining Eqs. (1) and (3), as (e.g., Clift et al., 1978):

$$V_{ST}=\frac{1}{18}\frac{(\rho_s-\rho_f)}{\mu}gd^2 \tag{4}$$

Here, ρ_s is the particle density, and g is gravity (taken as 9.8 m/s^2).

Table 1 summarises V_{ST} and Re for different particle sizes using Eqs. (4) and (2), respectively. It is assumed that particles are spherical, and that ρ_s and ρ_f are 2650 kg/m^3 (i.e., approximately that of quartz sand grains) and 1000 kg/m^3, respectively. Combining Eqs. (2) and (4), it can be shown that C_D calculated using Eq. (3) is not valid for d N 0.0625 mm (i.e., sediment larger than very fine sand; Table 1). Hence, other relationships need to be used for fine sand (or larger) grains to obtain C_D. Tran-Cong et al. (2004) developed an empirical function to calculate C_D for irregularly shaped particles.

Their formulation is based on Re and the geometric characteristics of the particle, as:

$$C_D=\frac{24\,d_A}{Re\,d_n}\left[1+\frac{0.15}{\sqrt{c}}\left(\frac{d_A}{d_n}Re\right)^{0.687}\right]+\frac{0.42\left(\frac{d_A}{d_n}\right)^2}{\sqrt{c}\left[1+4.25\times10^4\left(\frac{d_A}{d_n}Re\right)^{-1.16}\right]} \tag{5}$$

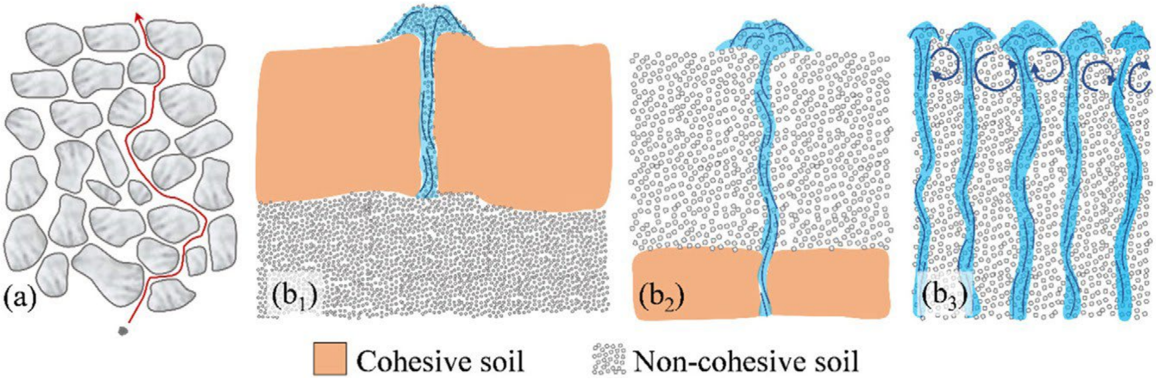

Fig. 1. Schematic illustration of different forms of subsurface sediment transport: (a) the passage of small particles through immobile pore networks (*suffusion* and *suffosion*), (b) three forms of sediment transport through preferential pathways. Two types of *sand boils* are shown: (b_1) preferential flow through a cohesive soil layer leading to the vertical transport of particles from the underlying non-cohesive sediment body, and (b_2) preferential flow within a non-cohesive soil layer caused by localised discharge from below (e.g., due to a fault or fracture). At sufficiently high hydraulic gradients, widespread fluidization may cause (b_3) *boiling sand*.

Table 1

Stokes' terminal velocity and corresponding Reynolds number for different particle sizes. Particle sizes are the limits for each particle description (for example, medium sand falls within the range 0.25 to 0.5 mm) following the Wentworth (1922) scale.

Particle description	Particle size, *d* (mm)	Stokes' terminal velocity, V_{ST} (m/s)	*Re*	Stokes' law validity
Very coarse sand	2	3.6	7191	Not valid
Coarse sand	1	0.90	899	Not valid
Medium sand	0.5	0.22	112	Not valid
Fine sand	0.25	0.056	14	Not valid
Very fine sand	0.125	0.014	1.76	Not valid
	0.0625	0.0035	0.22	Valid

Here, d_n is the diameter of a sphere of equal volume to the particle (e.g., Wadell, 1933), d_A is the diameter of a sphere of equal projected surface area (i.e., perpendicular to the flow direction) to the particle (e.g., Heywood, 1962), and c is the particle circularity or surface spheric- ity, given by $c = \pi d_A / P_P$, where P_P is the perimeter of the projected surface area of the particle (e.g., Wadell, 1933). Eq. (5) is valid for 0.15 b Re b 1500, 0.80 b d_A/d_n b 1.50 and 0.4 b c b 1.0, which covers most irregularly shaped particles in practical applications (Tran-Cong et al., 2004). For spherical particles, d_A/d_n and c are 1, and Eq. (5) reduces to the expression for spheres derived by Clift et al. (1978).

By rearranging Eq. (1), V_T can be calculated by:

$$V_T = \sqrt{\frac{2F_D}{C_D A_P \rho_f}} = \sqrt{\frac{2(W - F_B)}{C_D A_P \rho_f}} \tag{6}$$

Eq. (6) needs to be solved iteratively because C_D is a function of Re (Eq. (5)), which is a function of V_T (Eq. (2)).

As an alternative to the previous methodology for estimating the terminal velocity, Gibbs et al. (1971) derived an empirical equation for the relationship between V_T and d for spherical particles of diameters ranging from 0.1 μm to 6 mm, as:

$$V_T = \frac{-3\mu + \sqrt{9\mu^2 + gd^2\rho_f(\rho_s - \rho_f)\left(3.869 \times 10^{-5} + 2.48 \times 10^{-2} d\right)}}{\rho_f\left(1.1607 \times 10^{-4} + 7.4405 \times 10^{-2} d\right)} \tag{7}$$

Table 2 shows V_T values calculated using Eqs. (6) and (7) for spherical sand grains (using values for ρ_s, ρ_f and μ as defined above). The com- parison shows good agreement (b8% difference) between V_T values obtained using the two alternative methods. Comparison to Table 1 shows the order-of-magnitude error that arises if Stokes' terminal velocity is applied to larger particles.

2.2. Sediment transport through immobile pore networks (suffusion)

Water moving through a porous medium (i.e., seepage flow) creates dynamic forces on particles. If these forces exceed stabilizing forces holding particles in position, they may be mobilized. Some particles dislodged in this waymay be small enough to pass through the pore network of the body of sediment; a phenomenon referred to as seepage-induced internal instability (Fannin and Slangen, 2014). The pathway of moving particles is determined by the internal structure of the porous mediumand the direction of groundwater flow (Kovacs, 1981).

Fannin and Slangen (2014) reviewed various terms and descriptions of seepage-induced internal instability phenomena used in the literature.

Fannin and Slangen (2014) suggested that different seepage-induced internal instability phenomena can be characterised and distinguished based on measuring three variables including changes in the mass, volume, and hydraulic conductivity (K) of the porous medium. The latter can be deducted from measurements of flow rates and hydraulic gradients which are commonly recorded in experimental studies (e.g., Skempton and Brogan, 1994; Wan and Fell, 2004; Moffat et al., 2011).

Table 2

Terminal velocity of different sizes of spherical sand grains in freshwater.

Particle description	Particle size, d (mm)	Gibbs et al. (1971)	Tran-Cong et al. (2004)		
		Terminal velocity, V_T (m/s) (eq. (7))	Terminal velocity, V_T (m/s) (eq. (6))	Re	Drag coefficient, C_D (eq. (5))
Very coarse sand	2	0.27	0.28	558	0.56
Coarse sand	1	0.15	0.16	155	0.90
Medium sand	0.5	0.076	0.078	39	1.8
Fine Sand	0.25	0.032	0.034	8.5	4.7
Very fine sand	0.125	0.011	0.012	1.5	20
	0.0625	0.0033	0.0034	0.21	120

The stability of the porous medium skeleton may be modified de- pending on the rate of particle movement and the role of small particles in the mechanical strength of the soil. Accordingly, Fannin and Slangen (2014) recommended the term "*suffusion*" to describe "the non- destructive response, which may be quantified by a mass loss, no change in volume and an increase in hydraulic conductivity." They also advocated the term "*suffosion*" to describe "the instability phenomenon whereby the transport of fine particles by seepage flow is accompanied by a collapse of the soil structure." In other words, suffusion involves fine particle transport by seepage flow, resulting in mass re- duction and an increase in K, while the volume of porous medium is not changed, and the stability of the skeleton composed by the coarse grains is unaffected. Suffusion becomes suffosion if the migration of fine particles affects the porous medium skeleton (i.e., through rearrangement of coarser grains), resulting in an overall change to the soil body stability and a reduction in the solid volume accompanied by changes in K (Fannin and Slangen, 2014).

For suffusion to occur, Fell and Fry (2013) proposed three criteria:

(1) geometric criterion, (2) stress criterion, and (3) hydraulic criterion. The geometric criterion is a prerequisite that identifies that the pore size must be large enough to allow fine particles to pass through. The stress criterion establishes that the amount of finer particles must be less than enough to fill the voids of the soil matrix formed by the coarser particles, allowing free movement to some of finer particles in the soil matrix. For the hydraulic criterion to be satisfied, the flow velocity must be high enough to move fine particles through granular pore spaces. Significant research has been undertaken into the internal stability of soils from the geometric point of view (e.g., Kenney and Lau, 1985; Fannin and Moffat, 2006; Wan and Fell, 2008; Indraratna et al., 2011). Chang and Zhang (2013) summarized several existing geometric criteria in the literature and developed a dataset of soil internal stability tests. Here, soils that are *internally stable* have an ability to act as a filter thereby preventing the loss of small particles due to disturbing forces such as seepage and vibration (Kenney and Lau, 1985). Soils are otherwise considered *internally unstable* where suffusion may arise under the action of high groundwater flow. Factors such as clay dispersiveness may greatly en hance the susceptibility of soils to suffusion, particularly in engineered structures (FEMA, 2015). Transport and removal of finer individual particles may lead to micro-scale holes (e.g., De Wit et al., 1981; Van Beek et al., 2011). Therefore, suffusion may be the first sign of increasing levels of internal erosion (Van Beek et al., 2013), and is of interest in the design of filtration/drainage systems, particularly in relation to engineering structures that are vulnerable to piping failure (Worman and Olafsdottir, 1992).

Several numerical models have been developed to simulate seepage-induced fine particle transport through granular materials by coupling particle-based methods with groundwater flow modelling techniques (e.g., Abdelhamid and El Shamy, 2016; Aboul Hosn et al., 2018; Cheng et al., 2018). The flow of water through pores may be considered at the macroscopic level using continuum approaches or at a microscopic level where pore-scale flow is characterised, e.g., using discrete approaches such as the lattice Boltzmann method or the pseudo-particle method (Zhou et al., 2010). In the following, theory relating granular pore space, flow velocities and sediment movement is reviewed and combined to develop simple relationships between typical subsurface conditions and the characteristics of particles likely to be ejected with groundwater discharge.

2.2.1 Host media characteristics

The minimum pore (cavity) width (d_P) of granular materials dictates the largest particle size that can pass through a porous medium, and therefore dictates whether suffusion will occur. The packing of particles is a significant factor in the value of d_P. Theoretically, there are five different ways to pack uniform spherical particles which are shown in Fig. 2 (White and Walton, 1937).

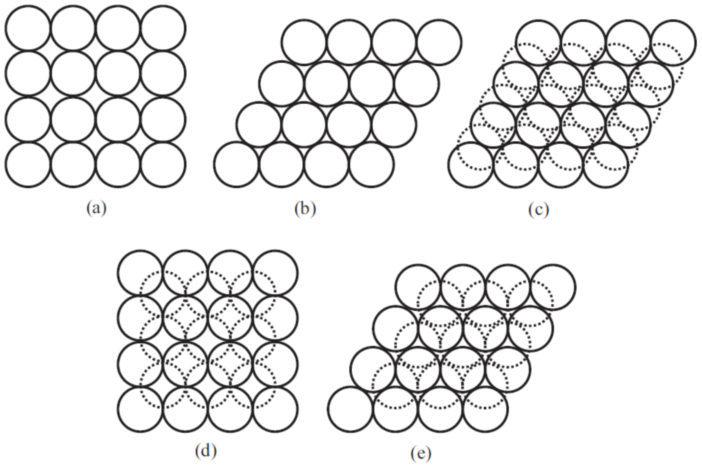

Fig. 2. Different packing arrangements for uniform spherical particles: (a) Cubical, (b) Single-staggered (Orthorhombic), (c) Double-staggered (Tetragonal), (d) Pyramidal

(Rhombohedral), (e) Tetrahedral (Rhombohedral). The solid circles represent spheres in one plane, while the dotted ones indicate the spheres (that are obscured from view) in the next layer (White andWalton, 1937).

Table 3 lists d_P, the number of pathways (per particle) with pore width equal to d_P, and porosity (n). These can be calculated based on the geometric configuration of each packing arrangement (Gupta and Larson, 1979), noting that for some packing arrangements (e.g., double-staggered, pyramidal, tetrahedral) there are alternative values of d_P given in Table 3 due to different possible sub-configurations.

Table 3

Porosity, minimum pore (cavity) width and number of cavities (i.e., the number of void spaces adjacent to a particle with the same minimum pore size) in various packing arrangements for uniform spherical particles (Gupta and Larson, 1979). Note that (a) and (b) denote alternative values of d_P due to different possible sub-configurations.

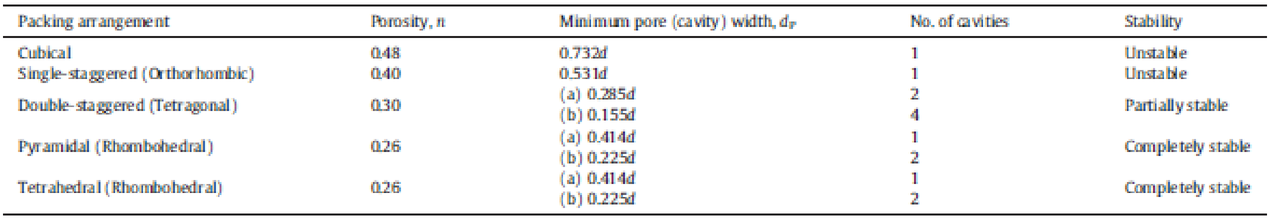

Packing arrangement	Porosity, n	Minimum pore (cavity) width, d_P	No. of cavities	Stability
Cubical	0.48	0.732d	1	Unstable
Single-staggered (Orthorhombic)	0.40	0.531d	1	Unstable
Double-staggered (Tetragonal)	0.30	(a) 0.285d (b) 0.155d	2 4	Partially stable
Pyramidal (Rhombohedral)	0.26	(a) 0.414d (b) 0.225d	1 2	Completely stable
Tetrahedral (Rhombohedral)	0.26	(a) 0.414d (b) 0.225d	1 2	Completely stable

The pyramidal and tetrahedral arrangements of Table 3 are completely stable, whereas the double-staggered arrangement is partially stable requiring some support from the container walls. The cubical and single-staggered arrangements are unstable in that they need considerable support from the container walls (e.g., Graton and Fraser, 1935; Gray, 1968). In field and laboratory conditions, the formation of unstable packing arrangements in soil (i.e., cubical and single-staggered) is highly unlikely. Therefore, only completely stable (i.e., pyramidal and tetrahedral) and partially stable (i.e., double- staggered) arrangements are used in assigning minimum pore widths in the analysis that follows. While we consider idealised (uniform grain size) materials, natural granular materials will comprise grain size distributions that lead to pore sizes (and values of n) that are prob- ably lower than those given in Table 3, because of pore-clogging by smaller particles. For example, the average pore size for well-sorted material was estimated by Sherard et al. (1984) as $0.11d_{15}$, where d_{15} is the equivalent particle size (diameter) at which 15% of the soil is finer by mass. However, in the absence of guidance on relationships between grain size distributions and d_P, we adopt the idealistic Table 3 values for the remainder of the analysis to demonstrate the development of theory.

We consider next the flow within sediments of known grain diameters (and therefore pore size), assuming relationships given in Table 3. The determination of flow in porous media requires knowledge of permeability (k), which can be approximated from d and n using empirical relationships such as Kozeny's (1927) permeability model, as:

$$k = c_0 \frac{d^2}{36} \frac{n^3}{(1-n)^2} \tag{8}$$

where c_0 is a constant that can vary from 1/2 (assuming capillary tubes have circular cross-sections) to 1/6 (Carman, 1937).

The relationships between pore size and packing arrangement in Table 3 are used to estimate pore sizes for typical grain diameters (assuming uniform particle size) in Table 4. We assume that Table 4 ap- plies to materials with narrow ranges in particle sizes (i.e., uniformly graded or well-sorted sediments). Table 4 lists values of k and d_P (using Eq. (8) and assuming $c_0 = 1/2$) for different packing arrangements, where d_P corresponds with the standard grain sizes used in Table 2.

1.1.1. *Initiation of suffusion: critical flow velocity*

The vertical movement of particles with sufficiently small diameter to pass through the pore network of a larger-diameter sediment is firstly examined by assuming that these particles will rise when the av- erage interstitial velocity (V_G) is greater than V_T. The critical condition (i.e., when particles of diameter d_P become unstable) arises when V_G equals V_T. This requires the assumption that V_G is locally independent of pore sizes, and therefore, the resulting theory is an initial, macro- scale approximation. V_G can be estimated from known relationships be- tween V_G and the groundwater hydraulic gradient (i). However, the re- lationship between i and V_G differs according to the flow conditions (i.e., laminar/Darcy, transitional or turbulent/non-Darcy) through po- rous media, which can be determined based on Re using Eq. (2). In ap- plying Eq. (2) to determine Re, Bear (1972) suggested to adopt $U = q$, where q is the specific discharge or Darcy velocity, calculated as the product of n and V_G. Different parameters have been assigned to L (i.e., the representative dimension of moving particles) in previous studies, including the mean grain diameter (d_m), other particle diameter statistics such as d_{10} or d_{50} (diameters at which 10% or 50% of a sample's mass is comprised of finer particles; Bear, 1972), $(k/n)^{1/2}$

(Collins, 1961) and $k^{1/2}$ (Ward, 1964). Various methods have been recommended for defining d_m, including that of Folk and Ward (1957), who suggest setting $\log_2 d_m = \log_2 d_{16} + \log_2 d_{50} + \log_2 d_{84}$.

Several values for Re at which flow transitions from laminar to turbulent (i.e., the critical Re; Re_c) are reported in the literature. Zeng and Grigg (2006) reviewed studies on non-Darcy (i.e., turbulent) flow behaviour in porous media and encountered ranges for Re_c that vary between that recommended by Bear (1972) (i.e., 1 b Re_c b 10), and that of Fancher and Lewis (1933) (i.e., 10 b Re_c b 1000).

Table 4

Minimum pore widths, i.e., reflecting the maximum size of particles that may move through the host material, and the corresponding particle diameter of host material and the permeability for different packing arrangements.

Minimum pore width, d_P (mm)	Particle diameter (d) and permeability (k) of host material							
	Double-staggered ($n = 0.30$)				Pyramidal, Tetrahedral ($n = 0.26$)			
	$d = d_P/0.155$ (mm)	k (m^2)	$d = d_P/0.285$ (mm)	k (m^2)	$d = d_P/0.225$ (mm)	k (m^2)	$d = d_P/0.414$ (mm)	k (m^2)
2	12.9	1.31E−07	7.02	3.86E−08	8.89	3.50E−08	4.83	1.03E−08
1	6.45	3.26E−08	3.51	9.65E−09	4.44	8.74E−09	2.42	2.58E−09
0.5	3.23	8.16E−09	1.75	2.41E−09	2.22	2.19E−09	1.21	6.46E−10
0.25	1.61	2.04E−09	0.877	6.03E−10	1.11	5.46E−10	0.604	1.61E−10
0.125	0.806	5.10E−10	0.439	1.51E−10	0.556	1.37E−10	0.302	4.04E−11
0.0625	0.403	1.28E−10	0.219	3.77E−11	0.278	3.42E−11	0.151	1.01E−11

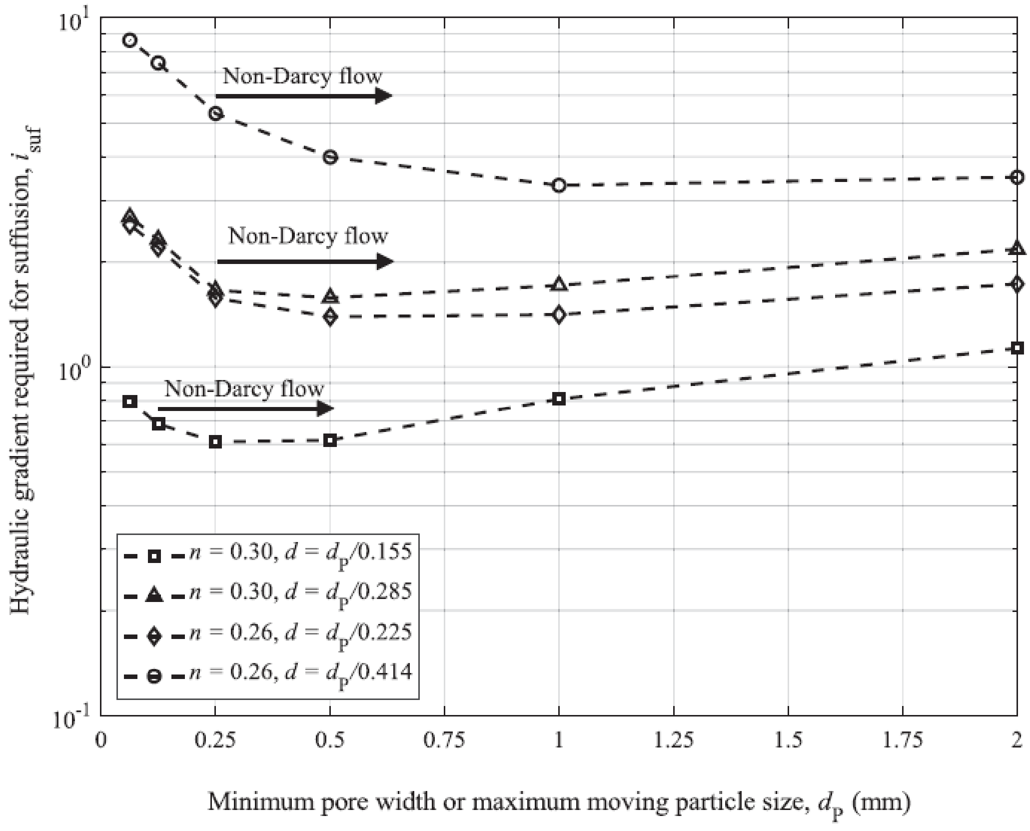

Fig. 3. Hydraulic gradient required for suffusion (i_{suf}) for different pore widths (or maximum moving particle size), d_P, and packing arrangements: double-staggered ($n = 0.3$) with $d_P = 0.155d$ (-□-) and $d_P = 0.285d$ (-△-); pyramidal/tetrahedral ($n = 0.26$) with $d_P = 0.225d$ (-◇-) and $d_P = 0.414d$ (-o-). Arrows indicate non-Darcy flow regimes.

The relation between i and V_G for different flow conditions in porous media is expressed by Bear (1972) as:

$$|i| = \begin{cases} q\dfrac{\mu}{k\rho_f g} & Re \le Re_c \text{ (Darcy/Laminar flow)} \\ aq + bq^2 & Re > Re_c \text{ (Non}-\text{Darcy/Turbulent flow)} \end{cases} \quad \text{where } q = nV_G \tag{9}$$

Here, a and b are constants whose values have been obtained experimentally in numerous studies, as reviewed by Bear (1972). Eq. (9) uses the absolute value of i to account for negative fluxes arising from positive values of i. In the current analysis, the equations provided by Ward (1964) are used to find a and b for non-Darcy flow in Eq. (9), as:

$$a = \frac{\mu}{k\rho_f g}, b = \frac{0.55}{g\sqrt{k}} \tag{10}$$

Application of Eq. (9) to values of V_T given in Table 2 (e.g., obtained from Eq. (6)) allows for an evaluation of the hydraulic gradient (i_{suf}) at which vertical suffusion (i.e., the vertical movement of subsurface particles) occurs, at least in terms of the largest particles that can pass through the porous matrix (i.e., of diameter d_P, see Table 3) and on the basis of other assumptions described above. Smaller particles will theoretically rise under hydraulic gradients less than i_{suf}, so that gradients greater than or equal to i_{suf} will theoretically cause suffusion of all non- cohesive sediment smaller than the minimum pore space of the immobile matrix. According to values for n and k in Table 4, i_{suf} (i.e., leading to $V_G = V_T$) for different packing arrangements is illustrated in Fig. 3. To obtain the i_{suf} values in Fig. 3, Re was first calculated using Eq. (2) (where $L = d$ and $U = q = nV_G$) for the combinations of d and n values given in Table 4 and assuming V_G equals the corresponding V_T values in Table 2. Re was compared with Re_c, which was assumed to be 10 according to Bear (1972). Subsequently, the appropriate Darcy (i.e., laminar) or non-Darcy (i.e., turbulent) flow expression (Eqs. (9) and (10)) was selected. Non-Darcy flow regimes are identified by arrows in Fig. 3

Kovacs (1981) suggests that the critical velocity to move a particle in a narrow tube is less than half the settling velocity of isolated particles unaffected by the conduit wall and collision with other particles. A large number of experiments have demonstrated that the particle settling velocity is reduced in higher suspended sediment concentrations (e.g., Baldock et al., 2004) by a factor usually given by the widely used semi-empirical Richardson and Zaki (1954) equation:

$$V_S = n^m V_T = (1-\phi)^m V_T \tag{11}$$

where V_S is the hindered settling velocity at porosity n, ϕ is the volumetric concentration of suspended sediments and m is an empirical exponent that ranges from 2.4 to 4.65 depending on Re for particles (Baldock et al., 2004).

If V_T is consequently reduced to V_S by a factor of $(1 - \phi)^m$, the value of i_{suf} (e.g., Fig. 3) reduces by a similar order (for laminar flow situations).For turbulent flow, the relationship between V_T and i_{suf} is nonlinear and the effect on i_{suf} of empirical or experimentally based modification to V_T (e.g., Eq. (11)) requires application of non-Darcy flow theory (e.g., Eqs. (9) and (10)).

1.1. *Vertical sediment transport following fluidization of non-cohesive soils*

Vertical sediment transport through preferential pathways in porous media may occur in several ways, as illustrated in Fig. 1. Sediment fluidization is an important phenomenon in all cases, even where sediment rises through preferential pathways within overlying cohesive (e.g., clay, peat, etc.) layers. Fluidization is the loss of effective stress (i.e., the stress that is resisted by the soil skeleton) of non-cohesive soils and may lead to the widely known condition of *quicksand*. It occurs when hydraulic forces accompanying flowing groundwater are sufficiently high to balance the total stress and reduce the effective stress to zero. This gives rise to a critical hydraulic gradient (i_c) at which fluidization may occur (Kovacs, 1981; Knappett and Craig, 2012). According to Terzaghi's (1922) theory:

$$i_c = \frac{\gamma_s - \gamma_f}{\gamma_f} = \frac{\gamma'}{\gamma_f} \tag{12}$$

Here, γ_f is the unit weight of the fluid, γ_s and γ' are the saturated and buoyant (or effective) unit weight of the soil, respectively. We consider Eq. (12) in more detail in the following sub-sections.

While the initiation of fluidization has been well studied, the mechanisms that lead to any accompanying subsurface sediment transport are not well defined. Our review has encountered two types of subsurface sediment transport that may arise following fluidization, which we differentiate using the terms sand boils and boiling sand. Conceptual models are shown in Fig. 1, which illustrates two sub-categories of sand boils, including: (1) heave and preferential flow through cohesive soil layers overlying non-cohesive sediments (Fig. 1b$_1$), and (2) individual boil vents within non-cohesive soil, caused by localised discharge from below (e.g., due to a fault or fracture; Fig. 1b$_2$). The sediment surface appears as a boiling fluid where fluidization leads to more distributed sediment movement in the case of boiling sand (Fig. 1b$_3$).

2.3.1. *Creation of preferential pathways: heave and pipe formation*

The hydraulic gradient required to cause heave in both cohesive and non-cohesive sediments, and sand boils and boiling sand in non- cohesive sediments is, theoretically at least, Terzaghi's (1922) i_c (i.e., Eq. (12)) (Kovacs, 1981; Wan and Fell, 2004; Knappett and Craig, 2012; FEMA, 2015). In cohesive soils, heaving can create concentrated outflows of seepage to the land surface through weaknesses (e.g., through hydraulic fracturing) in upper soil layers, in the form of holes or cracks (Fig. 1b$_1$) (e.g., Mansur et al., 2000; Glynn and Kuszmaul, 2010; Van Beek et al., 2011). This may result in localised discharge which De Louw et al. (2010, 2013) referred to as ‘sand boils’ or simply ‘boils’ depending respectively on whether or not sediment is ejected. FEMA (2015) describe two alternative approaches to the estimation of heave, based on whether force balances are undertaken using the effective stress or the total stress. In both cases, heave is predicted to occur when the hydraulic gradient equals Terzaghi's (1922) i_c. However, preferential pathways may arise in cohesive layers at hydraulic gradients well below i_c due to hydraulic fracturing (FEMA, 2015). Petrula et al. (2019) conducted extensive laboratory experiments on glass beads subjected to upward seepage flow and compared the measured critical hydraulic gradients for heave to calculated i_c using three different formulae developed during 1922–1931, and found that the Terzaghi's (1922) formula (i.e., Eq. (12)) provides the best prediction of i_c.

As discussed above and illustrated in Fig. 1, two types of conduit flow are apparent in previous studies of non-cohesive soils: sand boils (point discharge) and boiling sand (dispersed discharge). Differentiating between the mechanisms that create sand boils versus boiling sand re- quires some speculation because the distinction has not been investigated previously. Perhaps the former, sand boils, are found where conduits in non-cohesive soil bodies originate from a source of localised discharge (e.g., through a fault or fracture) below the non- cohesive soil body, as illustrated in Fig. 1b$_2$. Where upward seepage is dispersed (rather than localised) and sufficiently high to disturb the non-cohesive sediment structure over an area (rather than localised points causing discrete sand boils), this may lead to multiple pathways of instability in the soil structure, creating recirculation of particles in the form of boiling sand (Fig. 1b$_3$). In any case, the occurrence of both sand boils and boiling sand in non-cohesive soils requires the creation of preferential pathways (Wan and Fell, 2004). Discharge must be high enough to carry sand grains to the land surface and to maintain preferential flow conduits within the non-cohesive sediment body. In the case of boiling sand, it is likely that those pathways are continuously changing. Wan and Fell (2004) state that the hydraulic gradient leading to boiling sand is again theoretically equal to Terzaghi's (1922) i_c.

However, their experimental results for silt-sand-gravel and clay- sand-gravel soil mixtures showed that hydraulic gradients greater than i_c were needed for sand boils or boiling sand to occur. They attributed this to inter-particle electrochemical forces in soil mixtures containing silt or clay.

2.3.2. *Flow through preferential pathways*

For simplicity, conduits in both non-cohesive and cohesive soils are often treated as pipes, through which water is assumed to flow at high rates relative to flow through the surrounding sand matrix. The preferential pathways associated with sand boils (in both cohesive and non-cohesive sediment; Fig. 1b$_1$ and b$_2$) are approximated in the analysis that follows as vertical pipes, allowing use of the Darcy- Weisbach formula to describe their flow, as (Bear, 1972):

$$i_P = f\frac{1}{D_P}\frac{V_P^2}{2g} \tag{13}$$

where i_P is the hydraulic gradient in the pipe, f is the friction factor, D_P is the pipe diameter, and V_P is the flow velocity in the pipe. Re for pipe flow is obtained from Eq. (2), with $L = D_P$ and $U = V_P$. When $Re \leq 2320$, lam- inar pipe flow can be assumed in the preferential pathway (Van Beek et al., 2013), and the Hagen-Poiseuille formula (Hagen, 1839; Poiseuille, 1841) can be used by adopting $f = 64/Re$ in Eq. (13). When Re N 4000, turbulent pipe flow occurs, and f is a function of Re and the relative roughness, ε/D_P, where ε is the roughness of the pipe wall and is a function of grain size distribution, grain shape and grain spacing (e.g., Kamphuis, 1974). Various expressions and methods are available to find f for turbulent flow, including the Colebrook equation, given as (Nakayama, 1999):

$$\frac{1}{f} = -2\log\left(\frac{\varepsilon/D_P}{3.71} + \frac{2.51}{Re\sqrt{f}}\right) \tag{14}$$

The above theory allows for estimates of i_P required to produce V_P values that coincide with Table 2 values of V_T, i.e., hydraulic gradients needed to bring sediments of various sizes to the surface through verti- cal pipes. Values of d and D_P ranging from 0.0625 mm to 2 mm (as per Table 2 diameters) were evaluated for cases where $d \leq D_P$, i.e., particles theoretically able to pass through the pipe. Calculated values of Re ($0.2 \leq Re \leq 560$) indicated that in all cases, laminar flow con- ditions are expected. Values of i_P arising from these calculations are shown in Fig. 4.

1.2. *Subsurface flow processes: hypothetical modelling of conceptual models*

In the previous sub-sections, estimates are provided of hydraulic gradients required to cause heave and to move particles through immobile porous matrices and through preferential pathways. The conceptual models adopted in developing the above theory involve various combi- nations of non-cohesive materials (e.g., sand), with and without preferential flow paths (e.g., flow pipes), and with and without overlying/ underlying cohesive layers (e.g., overlying clay or underlaying faulted bedrock). The subsurface head distributions (and corresponding flow directions) accompanying these conceptual models are rarely considered in previous studies. Therefore, to assist in the understanding of subsurface flow processes associated with the previous situations, several hypothetical scenarios of simplified aquifer cross-sections are de- vised and modelled. Steady-state groundwater flow was simulated using MODFLOW (Harbaugh, 2005) to demonstrate the effects of preferential flow and layering on subsurface flow conditions. We neglect pipe flow and treat preferential flow features as equivalent porous medium, amongst other simplifying assumptions that allow for conceptual demonstration of subsurface flow in uncomplicated scenarios.

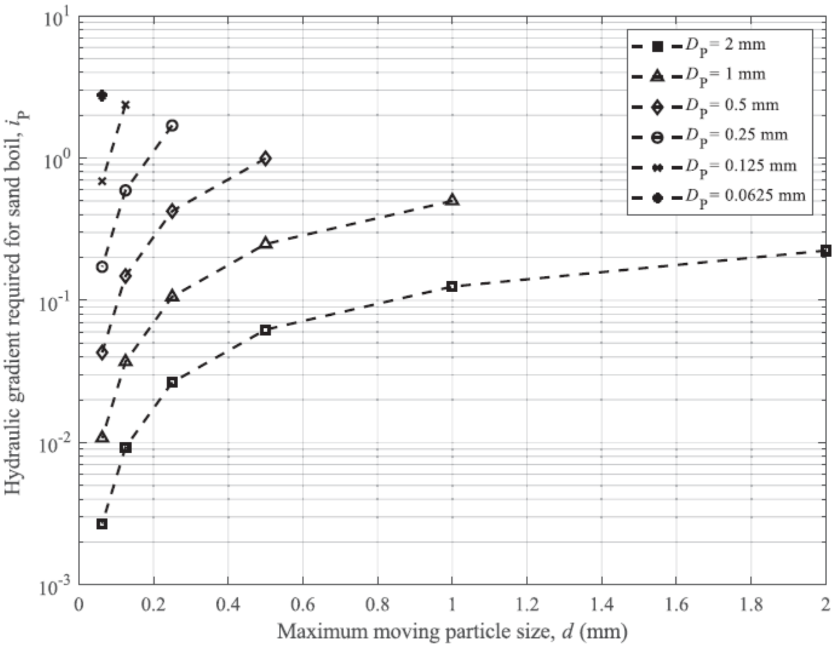

Fig. 4. Hydraulic gradients within boil ‘pipes’ (i_P) for different moving particle sizes (d) and pipe diameters (D_P).

The conceptual models are illustrated in Fig. 5, which also provides the head distributions arising from MODFLOW simulations. Flow is considered in cross-sections of 10 m depth by 10 m horizontal length (N.B., scale distortion of approximately 1:4 is used in Fig. 5). Flow directions are perpendicular to head contours. The boundary conditions in all cases are specified head conditions at the top (hydraulic head = land surface) and bottom (hydraulic head = 10 m above land surface), creating a hydraulic gradient of 1.0 that is uniform throughout the subsurface in the absence of aquifer heterogeneity (see Fig. 5a). No-flow conditions apply to the side boundaries, and other parameters are shown in Fig. 5.

The results shown in Fig. 5 highlight important subsurface flow processes of relevance to the conceptual models of earlier sub-sections. For example, relatively high hydraulic gradients occur in low-*K* layers that overly high-*K* layers (Fig. 5B and C). For the simple configuration of Fig. 5, manipulation of Darcy's law shows that:

$$\frac{i_U}{i_L} = \frac{K_L}{K_U} \tag{15}$$

$$i_U = \frac{\Delta h}{\frac{K_U}{K_L} L_L - L_U} \tag{16}$$

where subscripts L and U refer to lower and upper layers, *i* is hydraulic gradient, *K* is isotropic hydraulic conductivity, and Δh is the head drop (10 m in Fig. 5) across the subsurface profile. Eq. (16) allows for rapid assessment of gradients in low-*K* surface layers (for initial estimation of the potential for heave). Note that i_U is higher in the fine sand case (i.e., Fig. 5C; $|i_U| = 32.9$) than in the clay case (i.e., Fig. 5B; $|i_U| = 1.25$). It follows that where relatively fine materials are deposited over coarse sediment in groundwater upwelling zones, these are highly susceptible hydraulic gradients may occur in the parent material both with and without vertical preferential pathway (Fig. 5A and D). Hence, under idealistic homogeneous conditions, pipes may develop in sand bodies without necessarily reducing the likelihood of other pipes forming, given stable boundary conditions below the sand.

Fig. 5e represents a situation where the overlying low-*K* layer contains a preferential flow path, as might occur following heave (see Section 2.3.1). A comparison of head contours with and without the preferential pathway (Fig. 5E and B) shows that it creates considerably higher flow in the coarse sand (i.e., larger i_L; more closely spaced head contours), and significantly reduces i_U (i.e., more sparsely spaced head contours). Thus, the development of preferential pathways in low-*K* surface layers reduces the likelihood of heave and additional preferential pathways forming within the low-*K* layer in the near vicinity.

Fig. 5f illustrates the situation of a high-K feature within an other- wise low-K layer, underlying a coarse sand body, consistent with the conceptual model of Fig. 1b2, except no preferential flow features are simulated within the coarse sand. The MODFLOW results show a high hydraulic gradient (approximately equal to 19 in the vertical direction) at the base of the coarse sand layer where the preferential flow feature flow feature in the coarse sand in Fig. 5g reduces head gradients at the base of the coarse sand and increases gradients in the middle and upper sections. It follows that preferential flow features that develop within sand bodies, under conditions similar to Fig. 5g, propagate the high hydraulic gradients needed for fluidization over larger vertical extents than otherwise occurs without preferential flow paths. In other words, preferential flow paths tend to maintain and propagate the head gradients required for their occurrence (i.e., fluidization).

Experimental studies

The results of suffusion, fluidization and sand boil experiments are critical for assessing theory of the type described above, given the many simplifying assumptions adopted in the respective force equilibrium methods. The theory presented above does not account for friction arising from the collision of moving particles or between moving particles and the stationary porous matrix, or other factors including electro- chemical forces and other phenomena that modify the capacity for particles to move due to hydraulic forces.

1.1. *Suffusion experimental studies*

The initiation of piping, erosion processes and fine particle displacement rates caused by suffusion has been observed in laboratory experiments predominantly aimed at studying the onset and mechanisms of piping failure (e.g., De Wit et al., 1981; Van Beek et al., 2011). For ex- ample, Sterpi (2003) used laboratory experiments of erosion and trans- port of fine particles in a silty sand subjected to an upwards vertical seepage flow to produce an empirical equation relating particle trans- port to the experimental parameters. The experimental results showed that the percentage of eroded fine particles increased with time under a constant hydraulic gradient, and also increased with hydraulic gradient for constant periods of time.

Liang et al. (2017) designed a stress-controlled apparatus to investi- gate particle erosion under different stress states (i.e., combinations of vertical and confining stresses) and upwards seepage flow rate, by using a soil-water separating system. The results of their study showed that a specimen would collapse when the amount of eroded fine particles exceeded a critical proportion of the soil weight.

Wan and Fell (2004) investigated the internal stability of soils (mixtures of sand, gravel, silt, and clay) with respect to their susceptibility to suffusion by conducting both upward flow and downward flow seepage tests. The hydraulic gradient at which suffusion was initiated was re- corded. They defined a hydraulic gradient, i_{start}, at which the first sign of erosion of fine particles (e.g., observation of cloudiness in the flow) was observed. Wan and Fell's (2004) laboratory results showed that suffusion started at lower hydraulic gradients than that predicted by Eq. (12), i.e., i_{start} b Terzaghi's (1922) i_c for all unstable and many stable soil samples. Wan and Fell (2004) observed an inverse relationship be- tween *n* and i_{start}, whereby soils with higher *n* would be eroded at lower upward gradients. In other words, a higher i_{start} was required to erode a soil with higher γ_s. The theory of Kovacs (1981) is consistent with this general relationship. The same trend is generally applicable to the functions given in Fig. 3, in that the lowest and highest values of i_{suf} arose from the higher (0.3) and lower (0.26) *n* values, respectively. Wan and Fell's (2004) laboratory experiments also showed the effect of cohesiveness between particles, in that i_{start} was higher for soils with higher clay contents.

Ahlinhan and Achmus (2010) conducted several laboratory experiments on stable and unstable non-cohesive soils under upward and horizontal seepage flows to study the i_{start}. They determined the i_{start} where significant change (i.e., a strong increase)was observed in flow velocity and the mass of eroded fine particles. Their experiments showed that for unstable soils, the critical hydraulic gradient for upward flow slightly depends on the relative density

(D_r),which is an indicator of the degree of compaction in non-cohesive soils and is expressed as $D_r = (e_{max} - e) / (e_{max} - e_{min}) \times 100\%$ where e is the void ratio of soil in natural state, e_{max} and e_{min} are the maximum and minimum limits of e corresponding to the loosest and densest states of soil respectively, while a distinct dependence of critical hydraulic gradients on D_r was found for stable soils.

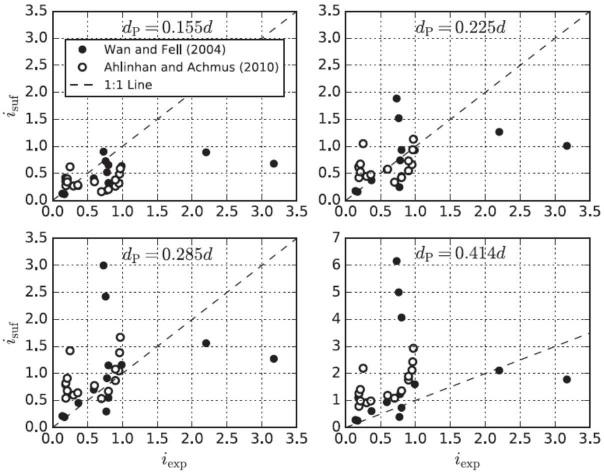

Fig. 6. Comparison between i_{suf} (suffusion theory described in earlier sections) and i_{exp} from the suffusion experiments of Wan and Fell (2004) and Ahlinhan and Achmus (2010). The four sub-figures show alternative assumptions (see Table 3) regarding the relationship between minimum pore size (d_P) and sediment diameter (d).

In laboratory experiments on sandy soils under upward flow, Fleshman and Rice (2014) observed that i_{start} was higher than both Terzaghi's (1922) i_c and values reported in previous laboratory research (e.g., Skempton and Brogan, 1994). This contradicts Wan and Fell's (2004) earlier results. Fleshman (2012) attributed these differences to the respective laboratory methodologies, in that in previous experiments, hydraulic gradients were measured across entire soil samples whereas the measurements of Fleshman and Rice (2014) focused on hydraulic gradients across smaller scales, namely at the seepage exit point. However, Schmertmann (2015) argued that the higher hydraulic gradient measured by Fleshman and Rice (2014) are seriously inconsistent with previous theory and laboratory and field experiments because of high friction between the interface of sample holder and the soil sample (i.e., sample side shear), the obstruction of the pore pressure probes to water and particle movement and resulting arching effects; hence, the Fleshman and Rice's (2014) results have not been used in the current study.

In the following, the theory developed in Section 2.2 for suffusion is compared to the experimental results of Wan and Fell (2004) and Ahlinhan and Achmus (2010). While i_{start} likely applies to the smallest particles within a soil, i_{suf} applies to the largest potentially mobile particles, and thus i_{start} b i_{suf} is expected, at least theoretically. Soil and experimental properties and the results of upward flow seepage tests by Wan and Fell (2004) and Ahlinhan and Achmus (2010) are given in Table 5. Wan and Fell (2004) observed three stages in their experiments and measured the hydraulic gradient in each stage, including (1) initial loss of fine particles, (2) extreme cloudiness, and (3) boiling sand development. The i values of Ahlinhan and Achmus (2010) in Table 5 correspond to the erosion of fine particles where a strong increase in mass transport and flow velocity was measured in their experiments, although Ahlinhan and Achmus (2010) observed some grain movements on the sample surface at smaller hydraulic gradients than those in Table 5.

Fig. 6 compares theoretical hydraulic gradients needed for suffusion (i_{suf}) based on the theory presented here with experimental values (i_{exp}) of Wan and Fell (2004) and Ahlinhan and Achmus (2010). Values of i_{exp} were taken as those required for the initial loss of fines (Wan and Fell, 2004; Ahlinhan and Achmus, 2010; Table 5). To calculate i_{suf}, several assumptions were required, including (1) the soil particles are spherical in shape and soil properties (i.e., ρ_s, d_{10}, d_{15}, d_{50}, and n) are given in Table 5, (2) the water properties are constant i.e., $\rho_f = 10^3$ kg/m^3, and $\mu = 10^{-3}$ Pa·s, (3) d_P is proportional to d_{50}, with proportionality based on the four different packing arrangements of Table 3 (i.e., double-staggered and pyramidal/tetrahedral, with two alternative values of d_P for each arrangement), (4) the maximum size of moving particles is equal to d_P, (5) Eq. (7) is used to calculate V_T where $d = d_P$, (6) k is obtained from Eq. (8) where $c_0 = 1/2$ and $d = d_{50}$, (7) Re is calculated by Eq. (2) where $L = d_{10}$, $U = q = nV_G$, and $V_G = V_T$, (8) Re_c is 10, and (9) Eqs. (9) and (10) are used to calculate i_{suf}. Assumption (1) is expected to overpredict i_{suf}, because V_T tends to be lower for natural particles relative to spheres (e.g., Arora et al., 2009). Assumptions (4) and (5) are also expected to overpredict i_{suf}, because suffused particles are likely to be smaller than d_P. An alternate value of c_0 (e.g., Fitts (2002) adopts c_0 equal to 1/5) would lead to lower k values for a given d, and therefore assumption (6) tends to underpredict i_{suf}.

The Fig. 6 results show relationships between i_{suf} and i_{exp} that vary from i_{suf} N i_{exp} (e.g., generally the case where $d_P = 0.414d$) to i_{suf} b i_{exp} (e.g., generally the case in $d_P = 0.155d$), although in all cases there is scatter across the 1:1 line. The comparisons show approximate correlation between theory and experimental results except for the highest i_{exp} value, which is underpredicted by i_{suf} in all four of the packing arrangements of Fig. 6. For the largest values of i_{suf} (e.g., where $d_P = 0.414d$), i_{suf} exceeds significantly i_{exp}, although where $d_P = 0.155d$, the match is improved. One possible cause of the larger deviations between i_{exp} and i_{suf} at higher hydraulic gradients may be related to the transition of flow from laminar to turbulent, which is not considered in the calculation of i_{suf} using Eq. (9). That is, in Eq. (9), the flow regime within the porous media is divided into laminar or turbulent based on Re values, whereas transitional flow likely arises at Re values greater than the threshold of $Re_c = 10$ (Bear, 1972). Statistical criteria including mean absolute error (MAE), root mean square error (RMSE), percent bias (PBIAS) and Nash-Sutcliffe efficiency (NSE) (Moriasi et al., 2007) are presented in Table 6 to evaluate the match between i_{suf} and i_{exp}. MAE, RMSE, PBIAS values closer to 0 and NSE closer to 1 indicate better agreement (Moriasi et al., 2007). Accordingly, packing arrangements with d_P =0.225d shows better match between i_{suf} and i_{exp}.

Sand boil experimental studies

Townsend et al. (1988) and Schmertmann (2000) obtained minimum gradients for piping in the lateral direction in clean, fine, uniform sands. Based on their laboratory tests, this type of sand was found to experience backward erosion piping at gradients as low as 0.08, although this appears model a severe scenario in that a highly erodible soil was used and a roof consisting of a plexiglass plate was placed above it. The low gradients for piping in Townsend et al. (1988) and Schmertmann (2000) experiments also attributed to local concentrations of flow lines at the entrance and discharge areas of the seepage flow and after pipe formation, near the pipe tip. The vertical movement of particles, which is the focus of the current review, differs to lateral particle movement, in which the stabilizing force includes the friction that inhibits particle rotation (e.g., along the horizontal plane), as op- posed to the requirement for the effective stress to drop to zero in ver- tical sand transport situations (Worman and Olafsdottir, 1992). Thus, vertical sediment movement likely requires higher hydraulic gradients relative to lateral sediment movement.

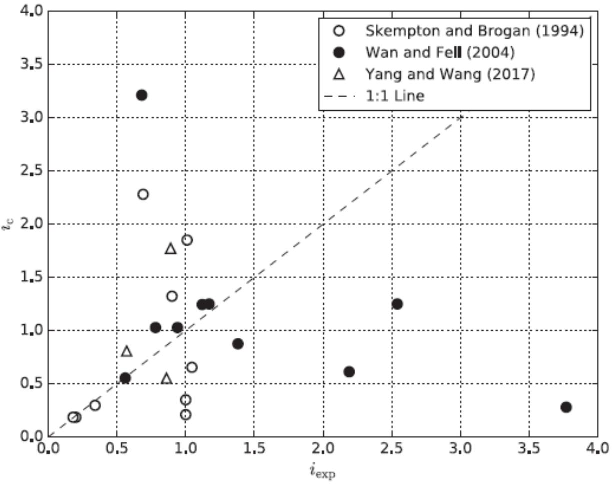

Fig. 7. Comparison between hydraulic gradients required to form sand boils using the theory of Section 2.3 (ic) and the experiments of Skempton and Brogan (1994), Wan and Fell (2004) and Yang andWang (2017) (iexp).

Table 7
Summary of soil properties and upward flow seepage test results of Skempton and Brogan (1994) and Yang andWang (2017).

Test no.	Particle density, ρ_s (kg/m^3)	d_{10} (mm)	d_{15} (mm)	d_{50} (mm)	Porosity, n	Hydraulic gradient, i_{exp}	Reference
S1	2650	0.089	0.095	0.149	0.490	0.69	Skempton and Brogan (1994)
S2	2650	0.220	0.259	0.501	0.460	0.90	
S3	2650	0.106	0.123	0.233	0.380	1.01	
F	2650	0.716	0.745	0.801	0.400	1.05	
A	2650	0.181	0.600	3.854	0.340	0.20	
AF	2650	0.181	0.600	3.854	0.340	0.18	
B	2650	0.485	0.900	3.854	0.370	0.34	
C	2650	0.662	0.980	3.854	0.375	1.00	
D	2650	1.080	1.600	4.137	0.365	1.00	
B	2650	0.175	0.189	0.280	0.420	0.89	Yang and Wang (2017)
C	2650	0.708	0.806	1.170	0.410	0.86	
G	2650	0.298	0.407	3.710	0.400	0.57	

Studies that reveal rates of vertical sediment transport through sand boils are uncommon relative to piping and suffusion experiments, and investigations that obtain i_c. Fujisawa et al. (2013) investigated the relationship between seepage forces and sand particle velocities due to up- ward and horizontal seepage flows within a vertical U-shaped cylinder and a horizontal pipe, respectively, in laboratory experiments. Sand par- ticle velocities obtained in their experiments were well estimated by force equilibrium analysis similar to that described herein (i.e., comparison of seepage, buoyancy and gravity forces).

Laboratory experiments evaluating i_c in sandy gravels subjected to upward flow were conducted by Skempton and Brogan (1994), who found that piping occurred at i_c values similar to Terzaghi's (1922) i_c when soils were internally stable. Otherwise, piping occurred at lower values of (i.e., one-third to one-fifth of Terzaghi's (1922) i_c) when the samples were internally unstable. Skempton and Brogan (1994) explained the discrepancy between experimental i_c and Terzaghi's (1922) i_c for internally unstable soil by that the greater part of the over- burden load is carried by coarser particles, leaving most of the finer particles under small pressure, i.e., a reduction in γ' in Eq. (12). Similar findings were obtained by Yang and Wang (2017), who undertook lab- oratory experiments on uniform sand (considered internally stable) and gap-graded sand (considered internally unstable). They compared 44 measured i_c values with i_c predictions from four alternative models, all based on the force equilibrium of a single soil particle. Comparison of predicted and measured i_c values showed that no single predictive model was applicable to all soil types.

Comprehensive studies aimed at controlling seepage and sand boils along the lower Mississippi River levees (e.g., USACE, 1956; Turnbull and Mansur, 1959) showed that the upward gradient required to cause sand boils varied from 0.5 to 0.8 at different sites. The gradient was determined by measuring the hydrostatic head beneath the top stratum (blanket) at the time sand boils first appeared (i.e., ic = hblanket/zblanket, where hblanket is the head beneath the blanket and zblanket is the thickness of the blanket). Accordingly, USACE (2005) recommends ic = 0.5 as the minimum gradient required to cause sand boils. In The Netherlands, TACFD (1999) assumed ic = 0.3 based on fluidization experiments of Yap (1981). A comparison between US and Dutch criteria for sand boils and piping can be found in Ammerlaan (2007).

In the sand boil, the head loss is not constant vertically through the sand boil and it is a function of sand properties, the size of sand boil and the flow rate (Robbins et al., 2019). Some recent studies (e.g., Bezuijen, 2015; Bezuijen et al., 2019; Robbins et al., 2019) have developed theoretical models to examine the head loss in a sand boil based on settling velocities in a vertical pipe that are hindered by suspended sediments. Robbins et al. (2019) compared their theory with head loss measurements in boils along the Mississippi River in the USA and the Waal River in The Netherlands, and also Yap's (1981) experiments. They found reasonably good agreement between measurements and their theory.

Theoretical and laboratory values for the hydraulic gradient required to create sand boils are compared in Fig. 7, in which ic is based on the theory developed in Section 2.3 in the case of sediment transport following fluidization of non-cohesive soils (sand boils) and iexp observations are taken from the studies of Wan and Fell (2004) (Table 5; I value at which “extreme cloudiness” was observed, as a possible indication of the onset of sand boil formation), Skempton and Brogan (1994) and Yang and Wang (2017) (Table 7). It should be noted that images of Skempton and Brogan (1994) and Yang and Wang (2017) experiments identify individual sand boils and therefore we consider that their results are applicable to the theory developed in Section 2.3.

The assumptions used in calculating i_c are: (1) fine particles trans- port through vertical preferential pathways, (2) Tables 5 and 7 provide soil properties (i.e., ρ_s, d_{10}, d_{15}, d_{50}, and n) and soil particles are spherical in shape, (3) the water properties are constant i.e., $\rho_f = 10^3$ kg/m^3, and $\mu = 10^{-3}$ Pa·s, (4) the maximum size of moving particles is equal to d_{10},

(5) the vertical preferential pathway has a circular cross-section (pipe) and the diameter of the pipe (D_P) should be bigger than the maximum size of moving particles (i.e., d_{10}), here assumed $D_P = d_{15}$. In other words, d_{15} is the initial pipe size at the start of sand boil allowing to particles with d_{10} pass through, (6) Eq. (7) is used to calculate V_T where $d = d_{10}$, (7) *Re* is

calculated by Eq. (2) where $L = D_P$, $U = V_P$, and $V_P = V_T$, and (8) Eq. (13) is used to calculate i_c where $f = 64/Re$ (Re b 2320 indicating laminar pipe flow).

Using d_{10} as the maximum size of moving particle and d_{15} as the minimum pipe diameter (assumptions 4 and 5, respectively) provides the best agreement between theoretical (i_c) and experimental (i_{exp}) hydraulic gradients required to form sand boils. Fig. 7 shows that approximately 32% of the experimental values (i_{exp}) are well predicted by theory with b13% difference, but otherwise, the match is poor. Clearly, the theory underpinning i_c (as described above) does not account for processes that are precursors to sand boil (and boiling sand) formation. This is discussed in more detail in the following section.

Discussion

Comparison can be made between the hydraulic gradients required to initiative heave (i.e., Terzaghi's (1922) i_c, although lower hydraulic gradients may create hydraulic fracturing; Section 2.3.1) and those associated with suffusion (i.e., i_{suf}; Fig. 3). Eq. (12) is applied to obtain estimates of i_c with $\gamma_f = 9.8$ kN/m^3 and noting that the two values of n in Table 3 equate to γ_s values of 21.14 and 21.79 kN/m^3 for n=0.3 and 0.26, respectively (assuming $\rho_s = 2650$ kg/m^3 and $\rho_f = 1000$ kg/m^3). Thus, the value of Terzaghi's (1922) i_c for double-staggered (n =0.30) and pyramidal/tetrahedral (n = 0.26) packing arrangements is 1.16 and 1.22. For the same values of n, i_{suf} in Fig. 3 varies from around 0.6 (the lowest value on the dashed line with square markers where $d_P = 0.25$ mm) to 8.6 (the highest value on the dashed line with circle markers where $d_P = 0.0625$ mm). Assuming that Terzaghi's (1922) i_c causes heave (i.e., i_c equal to 1.16 and 1.22), then heave theoretically occurs at hydraulic gradients that are lower than all i_{suf} values in Fig. 3 (i.e., for all values of d) for the three packing arrangements that produce the largest pore spaces (i.e., $d_P = 0.225d$ to $0.414d$). This seems prima facie to contradict the combined experimental findings of Wan and Fell (2004), who noticed suffusion prior to boiling and without reporting that any heave occurred. However, theoretical i_{suf} values used in the current study are those that require the largest particles capable of fitting through pore spaces to mobilise, and therefore, the first signs of suffusion should occur at gradients less than theoretical i_{suf} values. In reality, suffusion likely precedes heave, given that smaller particles require lower V_T values (Table 2) and therefore lower i_{suf}. However, heave is probably the precursor to the development of sand boils where there is no pre-existing defect (e.g., crack, root hole, animal burrow) in the soil layer, because the hydraulic gradient required for initial particle movement (Fig. 3) generally exceeds Terzaghi's (1922) i_c, as discussed above.

Table 8
Summary of literature comparing critical hydraulic gradients for different forms of subsurface sediment transport based on theory and experiments.

Laboratory experiments	Results	Comments
Skempton and Brogan (1994)	i_c ~ Terzaghi's (1922) i_c	Sand boil, internally stable soils
	i_c ~ 1/3 to 1/5 Terzaghi's (1922) i_c	Sand boil, internally unstable soils
Wan and Fell (2004)	i_{start} < Terzaghi's (1922) i_c	Suffusion, for all internally unstable and many internally stable soils
	i_c > Terzaghi's (1922) i_c	Sand boil, internally stable soils
	i_c < Terzaghi's (1922) i_c	Sand boil, internally unstable soils
	i_c > Terzaghi's (1922) i_c	Boiling sand, for all internally stable and many internally unstable soils
Ahlinhan and Achmus (2010)	i_{start} ~ Terzaghi's (1922) i_c	Suffusion, internally stable soils
	i_{start} ~ 1/3 to 1/5 Terzaghi's (1922)	Suffusion, internally unstable soils
Yang and Wang (2017)	i_c ~ Terzaghi's (1922) i_c	Sand boil, internally stable soils
	i_c ~ 1/2 Terzaghi's (1922) i_c	Sand boil, internally unstable soils

Intuitively, boiling sand probably occurs at higher hydraulic gradients relative to isolated sand boils. Notwithstanding the general concepts discussed above, the sequence of sediment transport processes accompanying high upward hydraulic gradients is likely to differ depending on specific circumstances. This is reflected in the summary of comparisons between hydraulic gradients required to initiate sand boils and boiling sand (i_c) and suffusion (i_{start}), and Terzaghi's (1922) i_c, given in Table 8.

Once sand boils form, the hydraulic gradients required to transport sand vertically upwards is expected to fall, because suffusion and heave, the precursors to sand boils, require higher hydraulic gradients (compare Fig. 4 with both Fig. 3 and Terzaghi's (1922) i_c values of 1.16 and 1.22 described above). The interplay between hydraulic gradients and the formation of preferential flow pathways (e.g., sand boil pipes), shown conceptually in Fig. 5, indicates that sand boil pipe formation in cohesive layers increases significantly the hydraulic gradients in non-cohesive sediments, while reducing the hydraulic gradients acting within underlying or overlying cohesive sediments. The same behaviour may not occur in homogeneous non-cohesive sediment bodies, because preferential pathways do not necessarily modify hydraulic gradients in undisturbed sediment, at least in theory (Fig. 5A). Combining these concepts, it would appear that sand boil pipes may be stable features where the source of sand and upward flow are continuous, because hydraulic gradients may increase in sand bodies subsequent to their formation, and yet sediment transport in pipes requires smaller hydraulic gradients than that needed for suffusion and heave. However, the sequence of suffusion, heave, pipe formation and sand boil occurrence, and the hydraulic gradients needed for each requires further experimental analysis.

The subsurface sediment transport conceptual diagrams illustrated in Fig. 1 can be extended by considering the situation of relatively fine, non-cohesive sediment (e.g., silt, fine sand) overlying coarse, non-cohesive sediment (e.g., medium or coarse sand). This is illustrated in Fig. 5c. Natural occurrences of this conceptual model include the widespread situation of groundwater discharge through coarse bed sediments of the sea floor or terrestrial water bodies, and the scenario of event-deposition of fine sediment due to floodwater sediment transport (freshwater bodies) and littoral transport (ocean). The hydraulic gradients required to cause suffusion, heave and/or sand movement through boil pipes are higher for coarser-grained materials. Therefore, it is plausible that fine particles deposited over coarse-grained sediments will be mobilized (i.e., they become fluidized) even though the underlying base material remains stable. The likelihood of this phenomenon is increased by the effect of an upper, lower-K layer on the hydraulic gradient distribution (Fig. 5C), considering Eqs. (15) and (16). It follows that regions of groundwater discharge through coarse-grained mate- rials in the beds of surface water bodies may act to enhance littoral transport and suspended sediment loads relative to regions where up- welling groundwater is absent. This is exemplified by field studies of Grant (1948) and Duncan (1964) who demonstrate this phenomenon through the impact of groundwater infiltration/exfiltration on swash sediment transport. Further research effort is warranted to evaluate the occurrence and influence of the conceptual model of Fig. 5c.

Whereas the analysis presented in this review adopts idealistic materials (e.g., uniform grain sizes), Sherard et al. (1984) approximate $d_P = 0.11d_{15}$ for well-sorted materials. Assuming $d_P = 0.11d_{15}$, it is possible to recalculate i_{suf} for natural (albeit well-sorted) materials. For ex- ample, for test 9 (Table 5), i_{suf} is equal to 0.03 when $d_P = 0.11d_{15}$ is assumed, while minimum and maximum values of i_{suf} are 0.13 and 0.28 with $d_P = 0.155d_{50}$ and $d_P = 0.414d_{50}$, respectively. The corresponding measured value for i ("initial loss of fines" in Table 5) was re- ported by Wan and Fell (2004) as 0.14. This shows that for natural materials, we expect that suffusion likely involves significantly smaller ejected particles than those reported in the analysis for uniform particles.

Our review finds significant knowledge gaps in the field of subsurface sediment transport. For example, few field-scale studies have been undertaken to quantify suffusion, heave, hydraulic fracturing and sand boil processes, despite that these features are encountered in a wide range of situations. The contribution of subsurface sediment trans- port to littoral transport and the suspension of sediment in open water bodies has not been previously assessed, with the exception of swash- zone processes. The effect of vegetation on sand boil formation has not been considered, even though the subsurface structures of roots are known to impart significant geomechanical forces (e.g., Zhou and Qi, 2019). Another factor that may influence the formation of voids (and perhaps preferential pathways) and subsurface sediment movement is gas ebullition, which to the best of the authors' knowledge has not been studied previously in the context of subsurface sediment transport, although the mechanisms leading to the formation of bubbles in springs and wells have been explored (e.g., Agnew and Halihan, 2018). More generally, the processes accompanying vertical subsurface sediment transport under heterogeneous conditions is largely unstudied, including relationships between heterogeneities and the formation of preferential flow paths. A rare attempt to manipulate subsurface sediment transport was reported by De Louw et al. (2013), who attempted to seal sand boils in the Haarlemmermeer and Noordplas Polders (The Netherlands). They found that the cessation of flow in one boil led to rapid hydraulic gradient increase across the low-K confining unit, an in- crease in flow in other boils, and the formation of new boils, to varying degrees in several attempts at sealing saline boils in agricultural areas. These observations are consistent with conceptual modelling under- taken as part of the current study (Fig. 5), in relation to the effect of preferential flow paths on low-K layers. Further research is warranted into intervening engineering measures designed to modify situations involving subsurface sediment transport through preferential flow paths. This is especially important in the face of projected sea-level rise, which is likely to exacerbate these phenomena in the coming decades due to changing head differences between the ocean and land. Additional evaluation of the importance of subsea boils in submarine groundwater dis- charge (SGD) is also warranted given that the predominance of SGD analyses neglect boil formation and flow (e.g., Moore, 2010; Konikow et al., 2013). More generally, physics-based modelling of the various phenomena leading to the liberation of sediment from the subsurface is warranted to unravel the influence of a wider range of factors than has been previously considered, and to build on the rudimentary functions based on simple force equilibria that are commonly adopted in practical applications (e.g., FEMA, 2015), and that are presented in the current article.

2. Conclusions

The current study evaluates different forms of vertical sediment transport in the subsurface through literature review and manipulation of previous theory. Subsurface sediment transport is a common phenomenon that is generally overlooked in the assessment of hydrological processes within catchments, sea and lake beds, and other areas within which groundwater discharge is expected. Rather, the primary foci of prior quantitative analyses of subsurface sediment transport are linked to engineered hydraulic structures. The various forms through which sediment may be liberated from the subsurface through groundwater discharge can be categorized into two groups: (1) suffusion, and (2) sand transport through preferential pathways. Sub-categories of (2) include: (a) point discharge caused by preferential flow through cohesive layers, (b) point discharge caused by preferential flow through non-cohesive sediment, and (c) dispersed discharge giving the appearance of boiling sand. Previous studies do not distinguish between the initial causes and driving processes associated with (a), (b) and (c), warranting further research effort.

Expressions are developed for the force balance at which upwards movement of subsurface sediment is expected to occur within each of the conceptual models described above, except the "boiling sand" cate- gory, which remains largely uncharacterised. Theories for the onset of sediment movement are described, based on parsimonious conceptual models and several simplifying assumptions, and incorporating existing theory related to piping failure (e.g., of earthen structures), soil fluidization and soil heave. Groundwater flow in a selection of simple conceptual models is simulated using numerical modelling to demonstrate subsurface flow patterns associated with idealised boil structures, and critical changes to subsurface head distributions that arise with the onset of preferential flow or with the addition of overlying low-K layers. For example, the deposition of a layer of fine-grained material onto a region of groundwater discharge through coarse-grained sediment will create enhanced hydraulic gradients in the deposited material, increasing the likelihood that the fine-grained sediment is fluidized. Estimates of critical hydraulic gradients that lead to subsurface sediment transport are compared to available observations from previous laboratory experiments to test the validity of existing theory and the formulae developed within the current study. While suffusion appears more or less predict- able using simple methods, the conditions leading to sand boils (and boiling sand) were poorly matched to theory.

The study of subsurface sediment transport requires additional effort to understand the mechanisms that lead to the liberation of sediment from preferential flow paths. While heave of cohesive sediments in a known precursor to sand boils, it is likely that heave is also required for preferential pathways to form in homogeneous, non-cohesive sediment bodies. Mismatch between theory and experimental results for the formation of boils in non-cohesive sediments perhaps indicates that heave in non-cohesive bodies requires hydraulic gradients that exceed those predicted by classic fluidization theory. This hypothesis should be tested using additional experimental work, which should also assess the occurrence of suffusion, heave and sand boils in heterogeneous media.

The results presented in this study are expected to have wide- ranging applications in terms of sediment transport in coastal regions and surface water bodies, where groundwater discharge occurs. While there is mismatch between theory and measurements when hydraulic gradients are high, the simple theory of the current article nonetheless offers a framework for at least initial estimates of the onset of sediment movement in discharging groundwater. Additionally, the current theory may be extended to the study of the transport of other particulate mat- ter, including micro-plastics and biological particles, including faecal bacteria, which are released from aquifers and may contaminate the drinking water supplies of surface storages (e.g., Frank et al., 2018).

Declaration of competing interest

The authors declare that they have no known competing financial interests or personal relationships that could have appeared to influence the work reported in this paper.

Acknowledgments

The authors are thankful for helpful discussions with Perry de Louw regarding boils in Dutch polders, and Hongyu Qin for advice on aspects relating to geomechanics. Adrian Werner is the recipient of an Australian Research Council Future Fellowship (project number FT150100403). Amir Jazayeri is funded by the Australian Research Council (project numbers FT150100403 and LP140100317).

Appendix A. Supplementary data

Supplementary data to this article can be found online at https://doi.org/10.1016/j.scitotenv.2020.136757.

References

Abdelhamid, Y., El Shamy, U., 2016. Pore-scale modeling of fine-particle migration in granular filters. International Journal of Geomechanics 16 (3), 04015086. https://doi.org/10.1061/(ASCE)GM.1943-5622.0000592.

Aboul Hosn, R., Sibille, L., Benahmed, N., Chareyre, B., 2018. A discrete numerical model involving partial fluid-solid coupling to describe suffusion effects in soils. Comput. Geotech. 95, 30–39. https://doi.org/10.1016/j.compgeo.2017.11.006.

Agnew, R.J., Halihan, T., 2018. Why springs bubble: a framework for gas discharge in groundwater. Groundwater 56 (6), 859–870. https://doi.org/10.1111/gwat.12789.

Ahlinhan, M.F., Achmus, M., 2010. Experimental investigation of critical hydraulic gradients of unstable soils. Scour and Erosion 5, 599–608. https://doi.org/10.1061/41147 (392)58.

Ammerlaan, P.R.M., 2007. Levees and Levee Evaluation, the Dutch and US Practice Compared. M.Sc. thesis. Delft University of Technology, Delft.

Arora, C., Kumar, B.P., Narayana, A.C., 2009. Influence of particle shape on drag coefficient for commonly occurring sandy particles in coastal areas. Journal of Ocean and Climate: Science, Technology and Impacts 1 (2), 99–112. https://doi.org/10.1260/1759-3131.1.2.99.

Baldock, T.E., Tomkins, M.R., Nielsen, P., Hughes, M.G., 2004. Settling velocity of sediments at high concentrations. Coast. Eng. 51 (1), 91–100. https://doi.org/10.1016/j.coastaleng.2003.12.004.

Bear, J., 1972. Dynamics of Fluids in Porous Media. Elsevier, Amsterdam.

Bezuijen, A., 2015. Critical vertical gradients in piping (Report 1220088-003). Deltares, Delft.

Bezuijen, A., Vandenboer, K., van Beek, V., Robbins, B., 2019. Pressure drop in vertical pipes of sand boils. European Conference on Soil Mechanics and Geotechnical Engineering: Proceeding of the XVII ECSMGE-2019 (Reykjavik, Iceland).

Bonelli, S., Nicot, F. (Eds.), 2013. Erosion in Geomechanics Applied to Dams and Levees. Wiley, London.

Bonelli, S., Fell, R., Benahmed, N., 2013. Concentrated leak erosion. In: Bonelli, S., Nicot, F. (Eds.), Erosion in Geomechanics Applied to Dams and Levees. Wiley, London, pp. 271–341. https://doi.org/10.1002/9781118577165.ch4.

Carman, P.C., 1937. Fluid flow through granular beds. Transactions, Institution of Chemical Engineers (London) 15, 150–166.

Chang, D.S., Zhang, L.M., 2013. Extended internal stability criteria for soils under seepage. Soils Found. 53, 569–583. https://doi.org/10.1016/j.sandf.2013.06.008.

Cheng, K., Wang, Y., Yang, Q., 2018. A semi-resolved CFD-DEM model for seepage-induced fine particle migration in gap-graded soils. Comput. Geotech. 100, 30–51. https://doi.org/10.1016/j.compgeo.2018.04.004.

Clift, R., Grace, J.R., Weber, M.E., 1978. Bubbles, Drops, and Particles. Academic Press, New York.

Collins, R.E., 1961. Flow of Fluids through Porous Materials. Reinhold, New York.

De Louw, P.G.B., Oude Essink, G.H.P., Stuyfzand, P.J., van der Zee, S.E.A.T.M., 2010. Upward groundwater flow in boils as the dominant mechanism of salinization in deep polders, the Netherlands. J. Hydrol. 394, 494–506. https://doi.org/10.1016/j.jhydrol.2010.10.009.

De Louw, P.G.B., Vandenbohede, A., Werner, A.D., Oude Essink, G.H.P., 2013. Natural salt- water upconing by preferential groundwater discharge through boils. J. Hydrol. 490, 74–87. https://doi.org/10.1016/j.jhydrol.2013.03.025.

De Wit, J.M., Sellmeijer, J.B., Penning, A., 1981. Laboratory testing on piping. Proceedings 10th International Conference on Soil Mechanics and Foundation Engineering (Stockholm, Sweden).

Decker, R.S., Dunnigan, L.P., 1977. Development and use of the soil conservation service dispersion test. In: Sherard, J.L., Decker, R.S. (Eds.), Dispersive Clays, Related Piping, and Erosion in Geotechnical Projects. ASTM International, West Conshohocken, PA,

pp. 94–109. https://doi.org/10.1520/STP26982S.

Duncan, J.R., 1964. The effects of water table and tidal cycle on swash-backwash sediment distribution and beach profile development. Mar. Geol. 2 (3), 186–197. https://doi. org/10.1016/0025-3227(64)90039-8.

Fancher, G.H., Lewis, J.A., 1933. Flow of simple fluids through porous materials. Ind. Eng. Chem. 25 (10), 1139–1147. https://doi.org/10.1021/ie50286a020.

Fannin, R.J., Moffat, R., 2006. Observations on internal stability of cohesionless soils. Géotechnique 56 (7), 497–500. https://doi.org/10.1680/geot.2006.56.7.497.

Fannin, R.J., Slangen, P., 2014. On the distinct phenomena of suffusion and suffosion. Géotechnique Letters 4 (4), 289–294. https://doi.org/10.1680/geolett.14.00051.

Fell, R., Fry, J., 2013. State of the art on the likelihood of internal erosion of dams and levees by means of testing. In: Bonelli, S., Nicot, F. (Eds.), Erosion in Geomechanics Applied to Dams and Levees. Wiley, London, pp. 1–99. https://doi.org/10.1002/ 9781118577165.ch4.

FEMA, 2015. Evaluation and Monitoring of Seepage and Internal Erosion, Interagency Committee on Dam Safety (ICODS) (Report No. FEMA P-1032). Federal Emergency Management Agency Retrieved from. https://www.fema.gov/media-library/assets/ documents/107639.

Fitts, C.R., 2002. Groundwater Science. Academic Press, London.

Fleshman, M., 2012. Laboratory Modelling of Critical Hydraulic Conditions for the Initiation of Piping. M.Sc. thesis. Utah State University, Logan.

Fleshman, M.S., Rice, J.D., 2014. Laboratory modeling of the mechanisms of piping erosion initiation. J. Geotech. Geoenviron. 140 (6), 04014017. https://doi.org/10.1061/(ASCE) GT.1943-5606.0001106.

Folk, R.L., Ward, W.C., 1957. Brazos River bar [Texas]; a study in the significance of grain size parameters. J. Sediment. Res. 27 (1), 3–26. https://doi.org/10.1306/74D70646- 2B21-11D7-8648000102C1865D.

Frank, S., Goeppert, N., Goldscheider, N., 2018. Fluorescence-based multi-parameter approach to characterize dynamics of organic carbon, faecal bacteria and particles at alpine karst springs. Sci. Total Environ. 615, 1446–1459. https://doi.org/10.1016/j. scitotenv.2017.09.095.

Fujisawa, K., Murakami, A., Nishimura, S., Shuku, T., 2013. Relation between seepage force and velocity of sand particles during sand boiling. Geotechnical Engineering Journal of the SEAGS & AGSSEA 44 (2), 9–17.

Gibbs, R.J., Matthews, M.D., Link, D.A., 1971. The relationship between sphere size and settling velocity. J. Sediment. Petrol. 41 (1), 7–18. https://doi.org/10.1306/74D721D0- 2B21-11D7-8648000102C1865D.

Glynn, M.E., Kuszmaul, J., 2010. Prediction of Piping Erosion Along Middle Mississippi River levees - An Empirical Model (Report No. ERDC/GSL TR-04-12). U.S. Army Corps of Engineers, Washington, DC.

Grant, U.S., 1948. Influence of the water table on beach aggradation and degradation. J. Mar. Res. 7, 655–660.

Graton, L.C., Fraser, H.J., 1935. Systematic packing of spheres: with particular relation to porosity and permeability. The Journal of Geology 43 (8), 785–909.

Gray, W.A., 1968. The Packing of Solid Particles. Chapman and Hill Ltd, London.

Gupta, S.C., Larson, W.E., 1979. A model for predicting packing density of soils using particle-size distribution. Soil Sci. Soc. Am. J. 43 (4), 758–764. https://doi.org/ 10.2136/sssaj1979.03615995004300040028x.

Hagen, G.H.L., 1839. Ueber die Bewegung des Wassers in engen cylindrischen Röhren. Annalen der Physik und Chemie 46, 423–442. https://doi.org/10.1002/ andp.18391220304.

Hagerty, D.J., 1991. Piping/sapping erosion. I: basic considerations. J. Hydraul. Eng. 117 (8), 991–1008. https://doi.org/10.1061/(ASCE)0733-9429(1991)117:8(991).

Hagerty, D.J., 1992. Identification of Piping and Sapping Erosion of Streambanks (Contract Report HL-92-1). U.S. Army Corps of Engineers, Washington, DC.

Harbaugh, A.W., 2005. MODFLOW-2005: the U.S. Geological Survey modular groundwa- ter model - the ground-water flow process. U.S. Geological Survey Techniques and Methods 6-A16. https://doi.org/10.3133/tm6A16 Reston.

Heywood, H., 1962. Uniform and non-uniform motion of particles in fluids. Proceeding of the Symposium on the Interaction Between Fluid and Particles. Institute of Chemical Engineering, London, UK.

Indraratna, B., Nguyen, V.T., Rujikiatkamjorn, C., 2011. Assessing the potential of internal erosion and suffusion of granular soils. J. Geotech. Geoenviron. 137 (5), 550–554. https://doi.org/10.1061/(ASCE)GT.1943-5606.0000447.

Jones, J.A.A., 1981. The Nature of Soil Piping: A Review of Research. British Geomorpho- logical Research Group Research Monograph 3GeoBooks, Norwich.

Kamphuis, J.W., 1974. Determination of sand roughness for fixed beds. J. Hydraul. Res. 12 (2), 193–203. https://doi.org/10.1080/00221687409499737.

Kenney, T.C., Lau, D., 1985. Internal stability of granular filters. Can. Geotech. J. 22 (2), 215–225. https://doi.org/10.1139/t85-029.

Knappett, J.A., Craig, R.F., 2012. Craig's Soil Mechanics. 8th ed. Spon Press, New York. Konikow, L.F., Akhaan, M., Langevin, C.D., Michael, H.A., Sawyer, A.H., 2013. Seawater circulation in sediments driven by interactions between seabed topography and fluid density. Water Resour. Res. 49, 1386–1399. https://doi.org/10.1002/wrcr.20121.

Kovacs, G., 1981. Developments in Water Science-Seepage Hydraulics. Elsevier, Amsterdam. Kozeny, J., 1927. Ueber kapillare Leitung des Wassers im Boden. Sitzungsber Akad, Wiss., Wien 136 (2a), 271–306.

Lamb, H., 1932. Hydrodynamics. 6th ed. Cambridge University Press, London.

Li, Y., Craven, J., Schweig, E.S., Obermeier, S.F., 1996. Sand boils induced by the 1993 Mis- sissippi River flood: could they one day be misinterpreted as earthquake induced liq- uefaction? Geology 24 (2), 171–174. https://doi.org/10.1130/0091-7613(1996) 024b0171:SBIBTMN2.3.CO;2.

Liang, Y., Zeng, C., Wang, J.-J., Liu, M.-W., Yeh, T.-C.J., Zha, Y.-Y., 2017. Constant gradient erosion apparatus for appraisal of piping behavior in upward seepage flow. Geotech. Test. J. 40 (4), 630–642. https://doi.org/10.1520/GTJ20150282.

Madhav, G.V., Chhabra, R.P., 1995. Drag on non-spherical particles in viscous fluids. Int. J. Miner. Process. 43 (1–2), 15–29. https://doi.org/10.1016/0301-7516(94)00038-2.

Mansur, C.I., Postol, G., Salley, J.R., 2000. Performance of relief well systems along Missis- sippi River levees. J. Geotech. Geoenviron. 126 (8), 727–738. https://doi.org/10.1061/ (ASCE)1090-0241(2000)126:8(727).

Miesel, D., 1978. Rückschreitende Erosion unter Bindiger Deckschicht, Vorträge der Baugrundtagung. Deutsche Gesellschaft für Erd-und Grundbau E. V, Berlin.

Moffat, R., Fannin, R.J., Garner, S.J., 2011. Spatial and temporal progression of internal erosion in cohesionless soil. Can. Geotech. J. 48 (3), 399–412. https://doi.org/10.1139/T10-071. Moore, W.S., 2010. The effect of submarine groundwater discharge on the ocean. Annu. Rev. Mar. Sci. 2, 59–88. https://doi.org/10.1146/annurev-marine-120308-081019.

Moriasi, D., Arnold, J., Van Liew, M., Bingner, R., Harmel, R., Veith, T., 2007. Model evalua- tion guidelines for systematic quantification of accuracy in watershed simulations. Trans. ASABE 50 (3), 885–900. https://doi.org/10.13031/2013.23153.

Muller-Kirchenbauer, H., 1978. Zum Zeitlichen Verlauf der Rückschreitenden Erosion in Geschichtetem Untergrund unter Dämmen und Stauanlagen. Beitrag zum Talsperrensymposium, München.

~~Nakayama, Y., 1999. Introduction to Fluid Mechanics. Butterworth-Heinemann, Oxford~~. Petrula, L., Hala, M., Říha, J., 2019. Uncertainty in determining the critical hydraulic gradient of uniform glass beads. In: Bonelli, S., Jommi, C., Sterpi, D. (Eds.), Internal Erosion in Earthdams, Dikes and Levees: Proceeding of EWG-IE 26th Annual Meeting 2018. Lecture Notes in Civil Engineering. Springer, Cham. https://doi.org/10.1007/978-3- 319-99423-9_8.

Poiseuille, J.L.M., 1841. Recherches experimentales sur Ie mouvement des liquides dans les tubes de tres petits diametres, IV. Influence de la temperature sur la quantite de liquide qui traverse les tubes de tres petits diametres. Comptes rendus de l'Academie des Sciences 12, 11215.

Prandtl, L., Tietjens, O.G., 1934. Applied Hydro- and Aeromechanics. McGraw-Hill Book Co, New York.

Richards, K.S., Reddy, K.R., 2007. Critical appraisal of piping phenomena in earth dams. Bull. Eng. Geol. Environ. 66, 381–402. https://doi.org/10.1007/s10064-007-0095-0.

Richardson, J.F., Zaki, W.N., 1954. Sedimentation and fluidisation: part 1. Chem. Eng. Res. Des. 75 (Suppl), S82–S100. https://doi.org/10.1016/S0263-8762(97)80006-8.

Robbins, B.A., Stephens, I.J., Van Beek, V.M., Koelewijn, A.R., Bezuijen, A., 2019. Field measurements of sand boil hydraulics. Géotechnique, 1–8 https://doi.org/10.1680/jgeot.18.P.151.

Schmertmann, J.H., 2000. The non-filter factor of safety against piping through sands. In: Silva, F., Kavazanjian, E. (Eds.), Judgment and Innovation. Geotechnical Special Publication. American Society of Civil Engineers, Reston, pp. 65–132.

Schmertmann, J.H., 2015. Discussion of "laboratory modeling of the mechanisms of piping erosion initiation" by Mandie S. Fleshman and John D. Rice. J. Geotech. Geoenviron. 141 (8), 07015015. https://doi.org/10.1061/(ASCE)GT.1943-5606.0001309.

Sellmeijer, J.B., 1988. On the Mechanism of Piping under Impervious Structures. Ph.D. thesis. Delft University of Technology, Delft.

Sherard, J.L., Dunnigan, L.P., Talbot, J.R., 1984. Basic properties of sand and gravel filters. J. Geotech. Eng. 110 (6), 684–700. https://doi.org/10.1061/(ASCE)0733-9410(1984)110:6(684).

Silvis, F., 1991. Verificatie Piping Model: proeven in de deltagoot. Dutch. Grondmechanica Delft, The Netherlands.

Skempton, A.W., Brogan, J.M., 1994. Experiments on piping in sandy gravels. Geotechnique 44 (3), 449–460. https://doi.org/10.1680/geot.1994.44.3.449.

Sterpi, D., 2003. Effects of the erosion and transport of fine particles due to seepage flow. International Journal of Geomechanics 3 (1), 111–122. https://doi.org/10.1061/(ASCE)1532-3641(2003)3:1(111).

TACFD, 1999. Technical Report on Sand Boils (Piping). Technical Advisory Committee on Flood Defences, Delft.

Terzaghi, K., 1922. Der Grundbruch an Stauwerken und seine Verhutung (the failure of dams by piping and its prevention). Die Wasserkraft 17, 445–449 (Reprinted in (1960) From theory to practice in soil mechanics. New York: Wiley).

Townsend, F.C.D., Bloomquist, D., Shiau, J.M., Martinez, R., Rubin, H., 1988. Analytical and Experimental Investigation of Piping and Filter Design for Sands, Report to the Bureau of Reclamation. Department of Civil Engineering, University of Florida, Gainesville, Florida.

Tran-Cong, S., Gay, M., Michaelides, E.E., 2004. Drag coefficients of irregularly shaped particles. Powder Technol. 139 (1), 21–32. https://doi.org/10.1016/j.powtec.2003.10.002.

Turnbull, W.J., Mansur, C.I., 1959. Investigation of underseepage-Mississippi River levees. Journal of the Soil Mechanics and Foundations Division 85 (4), 41–94.

USACE, 1956. Investigation of Underseepage and its Control, Lower Mississippi River Levees, Volume I; Waterways Experiment Station. U.S. Army Corps of Engineers, Vicksburg, Mississippi.

USACE, 2005. Design Guidance for Levee Under-Seepage. U.S. Army Corps of Engineers, Washington, DC.

Van Beek, V.M., Knoeff, H., Sellmeijer, H., 2011. Observations on the process of backward erosion piping in small-, medium- and full-scale experiments. Eur. J. Environ. Civ. Eng. 15 (8), 1115–1137. https://doi.org/10.1080/19648189.2011.9714844.

Van Beek, V.M., van Bezuijen, A., Sellmeijer, H., 2013. Backward erosion piping. In: Bonelli,

S. (Ed.), Erosion in Geomechanics Applied to Dams and Levees. Wiley, London, pp. 193–269. https://doi.org/10.1002/9781118577165.ch3.

Wadell, H., 1933. Sphericity and roundness of rock particles. The Journal of Geology 41 (3), 310–331. https://doi.org/10.1086/624040.

Wan, C.F., Fell, R., 2004. Experimental Investigation of Internal Erosion by the Process of Suffusion in Embankment Dams and their Foundations (UNICIV REPORT No. R- 429). University of New South Wales, Sydney.

Wan, C.F., Fell, R., 2008. Assessing the potential of internal instability and suffusion in embankment dams and their foundations. J. Geotech. Geoenviron. 134 (3), 401–407. https://doi.org/10.1061/(ASCE)1090-0241(2008)134:3(401).

Ward, J.C., 1964. Turbulent flow in porous media. J. Hydraul. Div. 90 (5), 1–12.

Wentworth, C., 1922. A scale of grade and class terms for clastic sediments. The Journal of Geology 30 (5), 377–392.

White, H.E., Walton, S.F., 1937. Particle packing and particle shape. J. Am. Ceram. Soc. 20 (1–12), 155–166. https://doi.org/10.1111/j.1151-2916.1937.tb19882.x.

Worman, A., Olafsdottir, R., 1992. Erosion in a granular medium interface. J. Hydraul. Res. 30 (5), 639–655. https://doi.org/10.1080/00221689209498885.

Yang, K.-H., Wang, J.-Y., 2017. Experiment and statistical assessment on piping failures in soils with different gradations. Mar. Georesour. Geotechnol. 35 (4), 512–527. https:// doi.org/10.1080/1064119X.2016.1213338.

Yao, Q., Xie, J., Sun, D., Zhao, J., 2009. Sino-Dutch Cooperation Project-Data Collection of Dike Breach Cases of China. China Institute of Water Resources and Hydropower Research, Beijing.

Yap, H., 1981. Fluidisatieproeven op Strandzand. Laboratorium voor Grondmechanica Delft (Report CO-220884), Delft (in Dutch).

Zeng, Z., Grigg, R.J., 2006. A criterion for non-Darcy flow in porous media. Transp. Porous Media 63 (1), 57–69. https://doi.org/10.1007/s11242-005-2720-3.

Zhou, W.-H., Qi, X.-H., 2019. Root cohesion estimation of riparian trees based on model uncertainty characterization. J. Mater. Civ. Eng. 31 (2), 04018389. https://doi.org/ 10.1061/(ASCE)MT.1943-5533.0002600.

Zhou, Z.Y., Kuang, S.B., Chu, K.W., Yu, A.B., 2010. Discrete particle simulation of particle-fluid flow: model formulations and their applicability. J. Fluid Mech. 661, 482–510. https://doi.org/10.1017/S002211201000306X.

Appendix 3

Supplementary information

Porosity data

Sample ID	Porosity
A1 surf	38%
A1 5 cm	39%
A1 10 cm	39%
A1 15 cm	39%
A2 surf	36%
A2 5 cm	37%
A2 10 cm	37%
A2 15 cm	38%
A3 surf	36%
A3 5 cm	34%
A3 10 cm	26%
A3 15 cm	25%
A4 surf	35%
A4 5 cm	33%
A4 10 cm	33%
A4 15 cm	33%
A5 surf	35%
A5 5 cm	36%
A5 10 cm	35%
A5 15 cm	33%
A6 surf	34%
A6 5 cm	34%
A6 10 cm	35%
A6 15 cm	37%
B1 surf	33%
B1 5 cm	34%
B1 10 cm	32%
B1 15 cm	31%
B2 surf	35%
B2 5 cm	35%
B2 10 cm	33%
B2 15 cm	36%
B3 surf	39%
B3 5 cm	39%
B3 10 cm	39%
B3 15 cm	37%
B4 surf	35%
B4 5 cm	35%
B4 10 cm	34%
B4 15 cm	34%
B5 surf	35%
B5 5 cm	36%
B5 10 cm	33%
B5 15 cm	34%
C1 surf	35%
C1 5 cm	34%
C1 10 cm	32%
C1 15 cm	32%
C2 surf	36%
C2 5 cm	36%
C2 10 cm	34%
C2 15 cm	34%
C3 surf	39%
C3 5 cm	39%
C3 10 cm	37%
C3 15 cm	39%
C4 surf	35%
C4 5 cm	34%
C4 10 cm	38%
C4 15 cm	32%
C5 surf	34%
C5 5 cm	33%
C5 10 cm	34%
C5 15 cm	32%
C6 surf	35%
C6 5 cm	35%
C6 10 cm	34%
C6 15 cm	35%
spring surf	26%
Spring 5cm	26%
spring 10cm	28%
Spring 15cm	29%